UNIVERSIDADE FEDERAL DO CEARÁ
CENTRO DE CIÊNCIAS
DEPARTAMENTO DE FÍSICA
PROGRAMA DE PÓS-GRADUAÇÃO EM FÍSICA

BRUNO SOUSA ARAÚJO

SPIN-PHONON COUPLING IN MULTIFERROIC COMPOUNDS OBTAINED BY HIGH-PRESSURE/HIGH-TEMPERATURE SYNTHESIS

FORTALEZA
2019

BRUNO SOUSA ARAÚJO

SPIN-PHONON COUPLING IN MULTIFERROIC COMPOUNDS OBTAINED BY HIGH-PRESSURE/HIGH-TEMPERATURE SYNTHESIS

Tese apresentada ao Programa de Pós-Graduação em Física da Universidade Federal do Ceará, como requisito parcial à obtenção do título de doutor em Física. Área de concentração: Física da Matéria Condensada.

Orientador: Prof. Dr. Alejandro Pedro Ayala.

FORTALEZA
2019

Dados Internacionais de Catalogação na Publicação
Universidade Federal do Ceará
Biblioteca Universitária
Gerada automaticamente pelo módulo Catalog, mediante os dados fornecidos pelo(a) autor(a)

A687s Araújo, Bruno Sousa.
Spin-phonon coupling in multiferroic compounds obtained by High-Pressure/High-Temperature synthesis / Bruno Sousa Araújo. – 2019.
101 f. : il. color.

Tese (doutorado) – Universidade Federal do Ceará, Centro de Ciências, Programa de Pós-Graduação em Física , Fortaleza, 2019.
Orientação: Prof. Dr. Alejandro Pedro Ayala.

1. Síntese sob Altas-Pressões e Altas-Temperaturas. 2. Compostos multiferróicos. 3. Acoplamento Spin-Fônon. I. Título.

CDD 530

BRUNO SOUSA ARAÚJO

SPIN-PHONON COUPLING IN MULTIFERROIC COMPOUNDS OBTAINED BY HIGH-PRESSURE/HIGH-TEMPERATURE SYNTHESIS

Tese apresentada ao Programa de Pós-Graduação em Física da Universidade Federal do Ceará, como requisito parcial à obtenção do título de doutor em Física. Área de concentração: Física da Matéria Condensada.

Aprovada em: 13/03/2019.

BANCA EXAMINADORA

Prof. Dr. Alejandro Pedro Ayala (Orientador)
Universidade Federal do Ceará (UFC)

Prof. Dr. Carlos William de Araújo Paschoal
Universidade Federal do Ceará (UFC)

Prof. Dr. Paulo de Tarso Cavalcante Freire
Universidade Federal do Ceará (UFC)

Prof. Dr. Narcizo Marques de Souza Neto
Laboratório Nacional de Luz Síncrotron (LNLS)

Prof. Dr. Waldeci Paraguassu Feio
Universidade Federal do Pará (UFPA)

A Deus.

Aos meus pais, Hélio e Lucinha.

AGRADECIMENTOS

Agradeço a Deus pela saúde, paz, paciência e perseverança concebida a mim diariamente durante os caminhos percorridos até a finalização desta etapa.

Ao meu orientador professor Alejandro Pedro Ayala pela confiança e oportunidades concedidas, além da inestimável orientação desde o meu ingresso na pós-graduação. Pelos conselhos pessoais e profissionais, bem como pelo grande exemplo de determinação e empenho no desenvolvimento das atividades de pesquisa, dando sempre o seu melhor. E principalmente pelo apoio nos momentos de maiores dúvidas e dificuldades durante este doutorado.

Ao professor Carlos William pelos conselhos sobre a vida acadêmica e pelas discussões dos assuntos abordados neste projeto.

Ao professor J. Paul Attfield por me receber e orientar durante o período de doutorado sanduíche na Universidade de Edimburgo.

Aos membros da banca avaliadora, professores Paulo de Tarso, Narcizo Marques e Waldeci Paraguassu por se disponibilizarem a participar, pela leitura e por suas valiosas considerações para a melhoria deste trabalho.

Aos meus familiares Lucia Sousa, Hélio Araújo e Hugo Araújo pelos valiosos ensinamentos cotidianos, motivação e incentivo para seguir estudando o que gosto.

À minha namorada Liana Albano pela enorme paciência e companheirismo, mostrando sempre sua visão otimista do mundo e das pessoas, e pelo apoio dado diante de desabafos e momentos de desmotivação.

Aos meus tios Elder Araújo, Elaine Magalhães e Flávio Rocha pelo apoio aos estudos desde a graduação, pelos conselhos e, principalmente, pelos excepcionais exemplos profissionais.

As minhas avós Mirian Araújo e Neuza Rocha pelo exemplo de esforço e determinação pessoal mostrando-me que devemos sempre compartilhar o que temos de melhor com todos ao nosso redor.

À Manuela Castro pelas discussões, conversas e valioso companheirismo desde que ingressei na pós-graduação.

Aos colegas da sala 08, Fabio, Keilla, Mayra e Wellington pelas discussões de resultados e brincadeiras durante o tempo de convívio.

Aos demais membros do grupo de pesquisa, Beatriz, Georgina, Laura, Renata, Silmara, Vasco, Wendell e Yara pela companhia e discussões.

Aos demais professores, colegas e funcionários do departamento de física da Universidade Federal do Ceará pelo empenho em continuar mantendo o alto nível das pesquisas buscando sempre o melhor desenvolvimento da ciência em nosso departamento.

Finalmente, as agências de fomento à pesquisa que me deram o apoio financeiro para atividades executadas neste doutorado, FUNCAP, CAPES e CNPq.

RESUMO

Os métodos de reação de estado sólido convencional e sob altas pressões e altas temperaturas foram aplicados para sintetização de materiais com propriedades multiferróicas interessantes. A melanotalita Cu_2OCl_2 foi sintetizada através da reação de estado sólido convencional em atmosfera de ar. Nós provamos o acoplamento spin-fônon no Cu_2OCl_2 por espectroscopia Raman, mostrando que sua estrutura magnética incomensurada induz um acoplamento spin-fônon em acordo com a teoria do campo médio e é similar aqueles observado em diversos modos de *stretching* de compostos perovskitas. No caso da perovskita ortorrômbica $TmMnO_3$, as amostras foram obtidas através do tratamento de Altas-Pressões e Altas-Temperaturas na fase hexagonal do $TmMnO_3$. O espectro Raman do $TmMnO_3$ ortorrômbico dependente da temperatura é reportado mostrando o acoplamento spin-fônon em baixas temperaturas. Também verificamos que o ordenamento incomensurado induz este acoplamento spin-fônon em acordo com a teoria do campo médio e contrastando as suposições na literatura. Além do mais, mostramos que o acoplamento se torna nulo na fase antiferromagnética ordenada do tipo E. A perovskita $PbMn_7O_{12}$ também foi sintetizada através da técnica de altas-pressões e altas-temperaturas, apresentando três transições magnéticas em 83, 72 e 38 K. Análises inicias dos espectros Raman dependentes da temperatura revelaram efeitos de renormalização nas frequências dos fônons abaixo de 80 K provavelmente devido ao acoplamento spin-fônon. O comportamento dependente da pressão da estrutura da perovskita $PbMn_7O_{12}$ também revelou possíveis transições de fase em 8.5 e 19.3 GPa. Finalmente, a perovskita $BiCrO_3$ preparada por altas-pressões e altas-temperaturas apresentou propriedades interessantes com três anomalias no ordenamento magnético encontradas em torno de 40, 80 e 110K. Neste estudo reportamos um forte acoplamento spin-fônon observado por meio de espectroscopia Raman, mostrando que o ordenamento antiferromagnético do tipo G induz o acoplamento em acordo com a teoria de campo médio similarmente aqueles observados em outros compostos de perovskitas. Em adição ao acoplamento spin-fônon, foi mostrado que todos os fônons acoplados também são sensíveis à reorientação de spins em 80 K e à anomalia magnética em torno de 40 K.

Palavras-chave: Síntese sob Altas-Pressões e Altas-Temperaturas; Compostos Multiferróicos; Acoplamento Spin-Fônon.

ABSTRACT

The conventional solid-state reaction and under High-Pressure and High-Temperature methods were applied to synthesis of materials with interesting multiferroic properties. The melanothallite Cu_2OCl_2 was synthesized through conventional solid-state reaction in air atmosphere. We probed the spin-phonon coupling in Cu_2OCl_2 by Raman spectroscopy, showing that its incommensurate magnetic structure induces a spin-phonon coupling in accord with the mean field theory and it is similar to those observed in several stretching modes of perovskite compounds. In case of, the orthorhombic $TmMnO_3$ perovskite, the samples were obtained through High-Pressure and High-Temperature treatment of the hexagonal phase of $TmMnO_3$. The temperature-dependent Raman spectrum of orthorhombic $TmMnO_3$ is reported showing the spin-phonon coupling at low temperatures. We also verified that the incommensurate antiferromagnetic ordering induces this spin-phonon coupling in according to the mean field theory and contrasting the assumptions in literature. In addition, we show that the coupling becomes null at the E-type antiferromagnetically ordered phase. The perovskite $PbMn_7O_{12}$ also was synthesized through high-pressure and high-temperatures technique presenting three magnetic transitions at 83, 72 and 38 K. Initial temperature dependent Raman spectrum analysis revealed renormalization effects on phonons frequency below 80 K, probably related to spin-phonon coupling. The pressure dependent behavior of $PbMn_7O_{12}$ perovskite also revealed possible phase transitions at 8.5 and 19.03 GPa. Finally, the High-Pressure and High-Temperature prepared monoclinic $BiCrO_3$ perovskite present interesting properties with three anomalies of magnetic ordering founded around 40, 80 and 110 K. In this study, we report a strong spin-phonon coupling observed by Raman spectroscopy, showing that the G-type antiferromagnetic ordering induces the coupling in accord with the mean field theory similar to those observed in the several stretching modes of other perovskite compounds. In addition to the spin-phonon coupling, it was showed that all coupled phonons are also sensitive to the spin reorientation at 80 K and the magnetic anomaly around 40 K.

Keywords: HPHT synthesis; Multiferroic compounds; Spin-phonon coupling.

TABLES LIST

FIGURES LIST

TABLE OF CONTENTS

1. INTRODUCTION

The increasing interest in multiferroic materials in the last few decades has been driven by their fascinating physical properties and enormous technological potential. This technological potential implies in a range of applications including data recording, memory devices, magnetic field sensors, microwave devices and photovoltaic solar cells[1–5].

The primary ferroic orders can be said as: ferromagnetism, which are found in those materials presenting two opposite states of spontaneous magnetization; ferroelectricity, found in those materials presenting two states of spontaneous polarization and the ferroelasticity, related to those materials presenting two states of spontaneous deformation (strain)[6]. In all cases, there are two spontaneous ordered states, which can be alternate between themselves by application of an external field. Those ordered pairs of states are related through a hysteresis loop as illustrated in Figure 1.1. In this model, $\mathbf{A}_s$ is the saturation point of spontaneous ordered state (polarization, magnetization or strain) and $\mathbf{F}_s$ is the external field (electric, magnetic or stress) value able to induce the saturated state. In general, when the applied field is removed, the saturated state is reduced to the $\mathbf{A}_r$ point, classified as a residual induced state. The necessary field to remove all residual ordered state is called coercive field ($\mathbf{F}_c$).

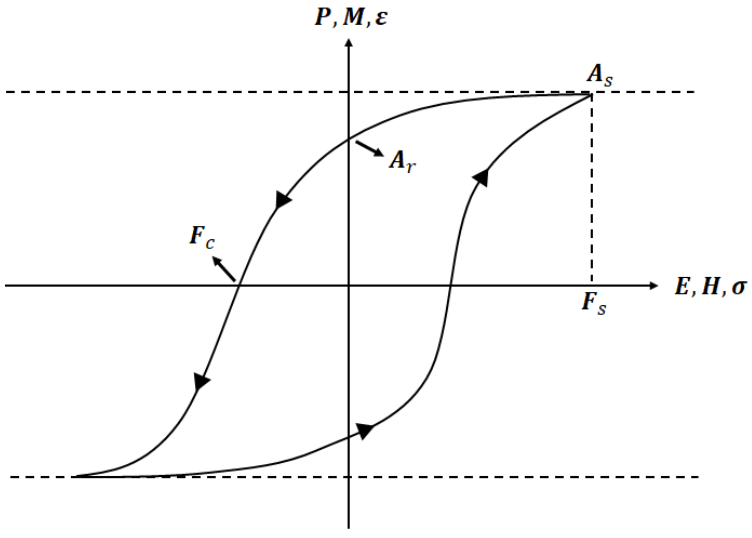

Figure 1.1. Characteristic hysteresis loop of ferroic amterials.

Through symmetry analysis in crystals, Pierre Curie predicted the coupling between magnetic and electric properties in insulating materials around 1894[7]. However, the first observation of magnetization in a dielectric material moving in an

electrical field was made by Rötgen at 1898, who also registered polarizations effects under a variable magnetic field[8]. Later, Debye named this coupled behavior as "magnetoelectric effect"[9]. In this way, multiferroic materials were firstly so-named by Schmid[10], defining then as those compounds which present at least two of the primary ferroic orders in the same phase.

However, multiferroic materials become scientific and technologically interesting not only because of their capacity to exhibit several ferroic orders, but also due to the possible coupling among these states of order. In Figure 1.2 are shown some of those possible couplings between the primary ferroic orders.

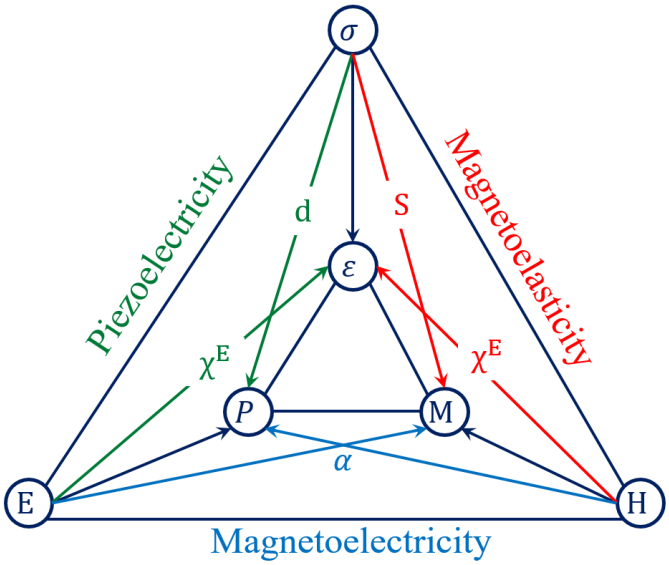

Figure 1.2. General couplings between ferroic orders founded in materials. (Adapted from reference [11])

In this study, we are focusing on magnetoelectric multiferroics materials which present the coexistence of coupled magnetic and electric ferroic orders in the same phase. At this point is important to note that some materials can present these ferroic orders at the same phase, but not necessarily, they are coupled as illustrated by Eerenstein *et al*[12] (see Figure 1.3).

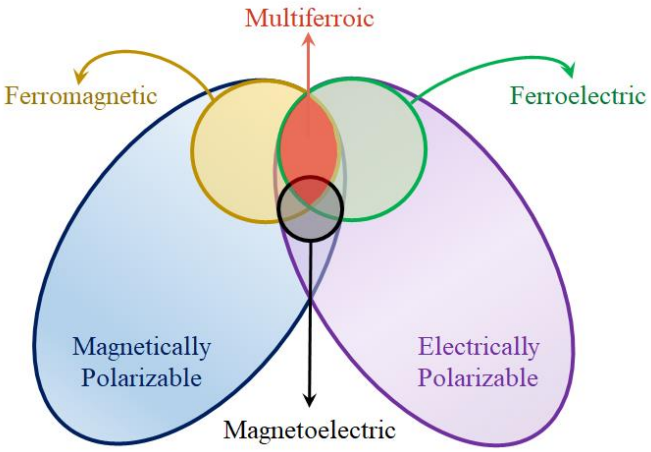

Figure 1.3. The relation between multiferroic and magnetoelectric materials. (adapted from reference [12])

1.1 *The nature of magnetic and electric orderings*

The magnetic properties of solid arise essentially from the magnetic moments of their atomic electrons[13]. In some cases, the magnetic interactions between two magnetic ions are mediated by a non-magnetic ion, commonly this non-magnetic ion is oxygen. Heisenberg reported a Hamiltonian to describe such interactions between two neighboring magnetic ions whose total electronic spins are namely $\boldsymbol{S}_i$ and $\boldsymbol{S}_j$. Such Hamiltonian is given by the overall sum of pairs of atoms at i and j sites lattice in such way that each pair is not taken into account twice:

$$\mathrm{H} = -\sum_{\mathrm{i,j>i}} J_{ij} \langle \mathbf{S}_\mathrm{i} \cdot \mathbf{S}_\mathrm{j} \rangle, \tag{1.1}$$

where the $\langle \boldsymbol{S}_i \cdot \boldsymbol{S}_j \rangle$ term is the scalar spin correlation function, while J is the exchange integral given by the exchange energy between the two magnetic ions. In this way, if $J_{ij} > 0$, the spin interactions favor the parallel alignment of spin moments. In this case, the system is said ferromagnetic (Figure 1.4(a)). Whereas, in case of $J_{ij} < 0$, the spin interactions favor an antiparallel alignment of the magnetic moments, constituting a antiferromagnetic system (Figure 1.4(b)).

Thus, in a general way, the magnetic orderings can be classified as ferromagnetic or antiferromagnetic. However, in some cases is possible to find the magnetic spin moments in an antiparallel orientation with a non-null resultant magnetization. In such cases, the system is called a ferrimagnetic system (Figure 1.4(c)).

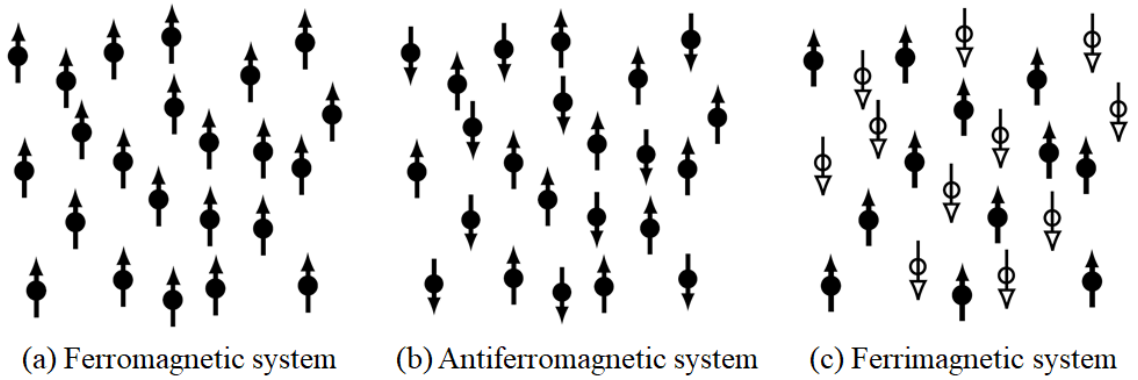

Figure 1.4. General magnetic orderings in the matter. The black up and down arrows indicate the opposite spin moments in figure (a) and (b). In figure (c) the different orientations of spin moments have different colors to clarify the lower number of down spins. (adapted from reference [13])

In the case of antiferromagnetic systems, the magnetic orderings are divided into two classes: commensurate and incommensurate. This classification is made according to the magnetic spin distribution in the unit cell of the crystaline structure. In case of commensurate phases, the antiferromagnetic orderings are said Type A, C, E or G, as is shown in Figure 1.5. In the case of incommensurate orderings, the spin moments can be seen as wave functions forming a spatial wave whose wavelength is not an integral number of the crystal lattice[14]. Examples of those incommensurate orderings can be: spin modulated waves, where the spin moments present fixed orientations, but with oscillating magnitudes; or cycloidal orderings, where the spin orientations are changed along the unit cell, as is show in Figure 1.6.

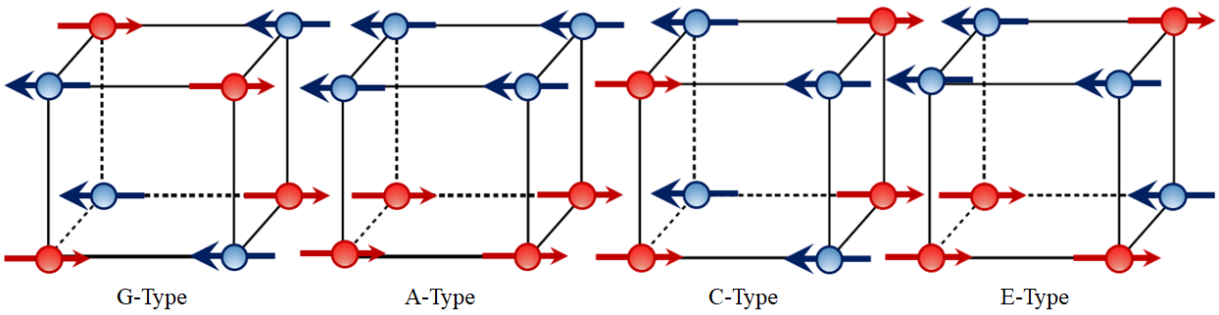

Figure 1.5. Different types of commensurate antiferromagnetic orderings. The red and blue arrows indicate opposite spin moments orientations. (Adapted from reference [13])

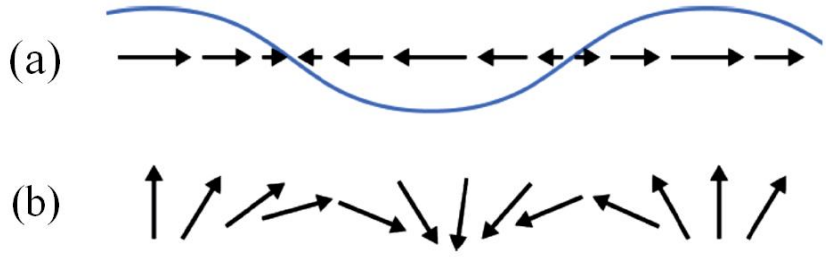

Figure 1.6. Examples of (a) sinusoidal and (b) cycloidal incommensurate magnetic orderings. (adapted from reference [15])

In the majority of materials, the electric order may be driven by geometric effects, charge ordering, electronic lone pairs or by means of magnetic orderings (these cases will be discussed later), being called spin-drive ferroelectricity[16,17].

In case of geometric effects, the ferroic order is given by a geometric distortion providing a closer packing of the structure, in this way, ions with different valences become closer favoring a polarization of this structure. This effect is commonly exemplified by using $YMnO_3$ [18], where the tilting of MnO_5 bipyramids approximates the oxygen ions at apical positions to the Y ions located at the free space between the bipyramids (Figure 1.7(a)).

The lone pair mechanism occurs when an ion with two 6*s* electrons are not involved in the chemical bonds. In this case, these two ions are "alone" inside the crystal structure becoming highly polarizable. A standard example of this mechanism occurs in the $BiFeO_3$, where the Bi^{3+} ions which present the cited two 6*s* playing the major role in the origin of ferroelectricity (Figure 1.7(b)).

The charge ordering effect is commonly observed in transition metal compounds in which the transition metals constituting the structure, after charge ordering, occupies nonequivalent sites having different valences and making different bonds (Figure 1.7(c)).

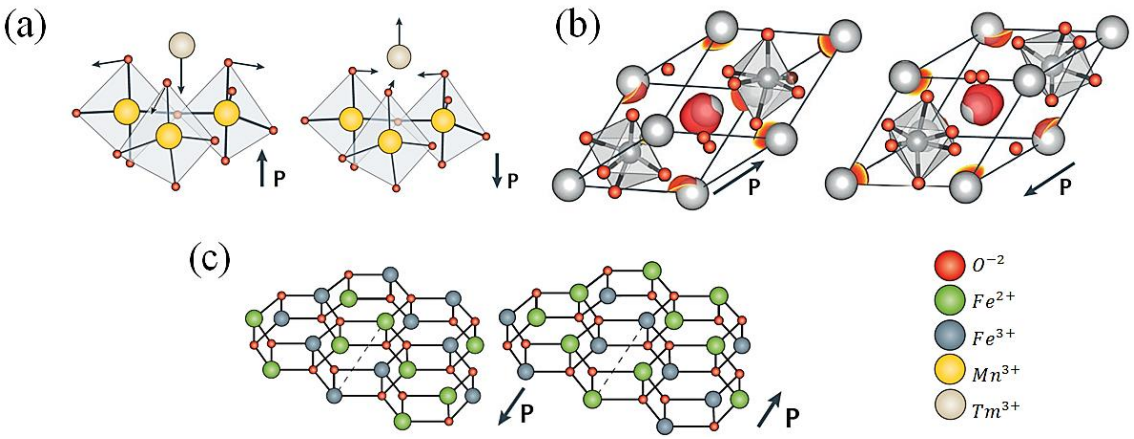

Figure 1.7. Mechanism to originate the electric orders. (adapted from references[16,17])

1.2 *Magnetoelectric materials*

An interesting example of coupled between some primary ferroic orders is the magnetoelectric effect. This property occurs in materials which have a magnetization (**M**) induced by an electrical field (**E**) or a polarized state (**P**) induced by the application of an external magnetic field (**H**). Traditionally, the contribution to the magnetoelectric effect can be obtained from the expansion of free energy of a material submitted to electrical and magnetic fields, as presented in reference[19]:

$$\mathrm{F}(\mathbf{E},\mathbf{H}) = \mathrm{F}_0 - \mathrm{P}_\mathrm{i}^\mathrm{s}\mathrm{E}_\mathrm{i} - \mathrm{M}_\mathrm{i}^\mathrm{s}\mathrm{H}_\mathrm{i} - \frac{1}{2}\varepsilon_0\varepsilon_{\mathrm{ij}}\mathrm{E}_\mathrm{i}\mathrm{E}_\mathrm{j} - \frac{1}{2}\mu_0\mu_{\mathrm{ij}}\mathrm{H}_\mathrm{i}\mathrm{H}_\mathrm{j} - \alpha_{\mathrm{ij}}\mathrm{E}_\mathrm{i}\mathrm{H}_\mathrm{j} - \frac{1}{2}\beta_{\mathrm{ijk}}\mathrm{E}_\mathrm{i}\mathrm{H}_\mathrm{j}\mathrm{H}_\mathrm{k} - \frac{1}{2}\gamma_{\mathrm{ijk}}\mathrm{H}_\mathrm{i}\mathrm{E}_\mathrm{j}\mathrm{E}_\mathrm{k} - \cdots \quad (1.2)$$

where F_0 is the free energy of such material and the reaming terms are those related to the electrical and magnetic fields contributions; $\mathbf{E}_\mathrm{i}$ and $\mathbf{H}_\mathrm{i}$ are the components of electrical and magnetic fields, respectively; $\mathbf{P}_\mathrm{i}^\mathrm{s}$ and $\mathbf{M}_\mathrm{i}^\mathrm{s}$ are the components of the spontaneous polarization and magnetization; ε_0 e μ_0 are the electric and magnetic susceptibilities in vacuum, while ε_{ij} and μ_{ij} are the higher order electrical permittivity and magnetic permeability. The differentiation of equation (1.2) with respect to the electrical and magnetic fields leads to:

$$\mathrm{P}(\mathbf{E},\mathbf{H}) = -\frac{\partial F}{\partial E_i} = P_i^s + \epsilon_0\epsilon_{ij}E_j + \alpha_{ij}H_j + \frac{1}{2}\beta_{ijk}H_jH_k + \gamma_{ijk}H_iE_j - \cdots \quad (1.3)$$

$$M_i(\boldsymbol{E},\boldsymbol{H}) = -\frac{\partial F}{\partial H_i} = M_i^s + \mu_0\mu_{ij}H_j + \alpha_{ij}E_i + \beta_{ijk}E_iH_j + \frac{1}{2}\gamma_{ijk}E_jE_k - \cdots \qquad (1.4)$$

The tensor $\hat{\alpha}$ corresponds to the induction of a polarization by a magnetic field or a magnetization induced by an electrical field and is recognized as the magnetoelectric linear tensor[6,7]. The γ and β terms are higher-order coefficients which will be omitted in this discussion. Since the research on the magnetoelectric effect is generally related to the linear effect, it is reasonable to omit the prefix "linear" and simply refer to it as the magnetoelectric effect.

In this way, the magnetoelectric materials are very interesting from the physical and technological point of view. The coupling between the electric and magnetic orders increased the interest of science both to investigate the fundamentals, which lead such coupling effects, as well as to understand the implication of these effects on fundamental features of those materials e.g. spin-orbital couplings, magnetostriction, spin-phonon coupling. From the technological point of view, the application of these two coupled orderings is promising due to their range of applications as data recording, memory devices, magnetic field sensors or microwave devices.

However, besides the interesting and useful coupling between the magnetic and electric orders, the existence of magnetoelectric materials is quite rare. The difficulty to find magnetoelectric materials is given because these two ferroic orders are self-excluding due to clear symmetric and chemical reasons[4,20].

From a symmetry point of view, the primary ferroic orders can be characterized by their variance in relation to the space and time inversion. When subjected to time reversal symmetry*, the electric polarization of crystal is maintained invariant, while the magnetic moment will be reversed. On the other hand, the space reversal symmetry would leave the magnetization invariant, while the electric polarization will be reverted. These relations are shown in Figure 1.8. Thus, while magnetic materials break the time inversion symmetry, electrically polarizable materials break the spatial inversion symmetry, the multiferroic materials consisting of both electric and magnetic orderings would break both space and time symmetries[4].

* This symmetry also can be more appropriately named by motion reversal symmetry. Deeper information about this symmetry is presented in references [4,161]

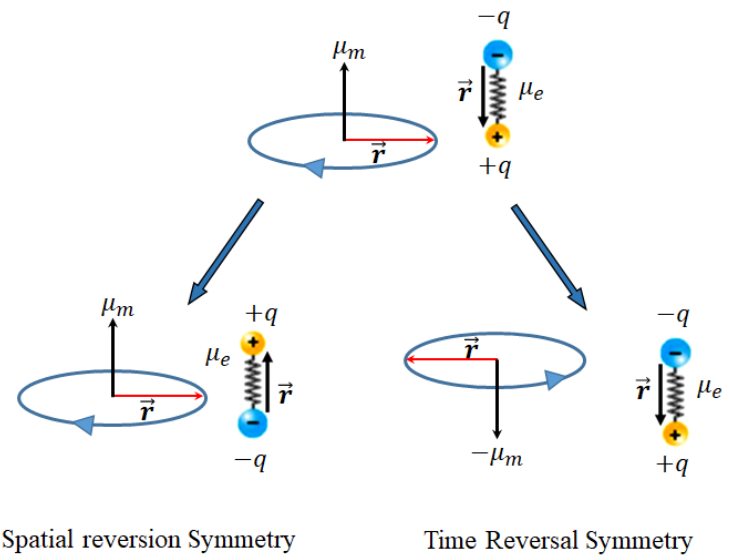

Figure 1.8. Invariance of magnetic and dipole moments under temporal and spatial reversion. (adapted from reference[21])

From a chemical point of view, the self-excluding properties are related to the origin of the electric and magnetic orderings. In general, the ferroelectric states emerge from the hybridization of electronic neighboring clouds, supporting off-centered ferroelectric ordering with empty d orbitals[16]. In such cases, these d^0 layers provide the formation of strong covalent bonds with neighboring ions favoring the off-center displacements. On the other hand, in general, the ordered magnetic moments are given by the partially filled d orbitals[20]. Somehow, the presence of d^n ions suppress the covalent bonds required by the off-center displacements for electric polarizations[17]. These considerations are known as the "d^0 vs d^n problem".

The simplest way to solve these problems is pointed out by Ramesh et al[22] and Khomski [17] where different ions play the role of magnetic and electric orderings. However, in such cases the magnetoelectric coupling is very weak. Nowadays, the best solution for difficulties raised from these two orderings is given through the spin-driven ferroelectric ordering mechanisms, found in type-II multiferroic compounds. These cases will be discussed in the following section.

A very similar system, which presents a coupling between electrical and magnetic orderings, is the magnetodielectric effect. In this case, this term denominates materials which present the dielectric function (ε) coupled to magnetic fields. However, in contrast to magnetoelectric materials, the magnetodielectric effect does not present a well-defined relation between its two ferroic orders, these materials present a response function in which this relation could be ambiguous[16].

1.3 *Types of Multiferroic Materials*

The multiferroic materials are classified in two types in according to the origin of the electric and magnetic orders and how they are coupled at the same phase.

The type-I multiferroic materials are those in which the ferroic orders coexist at the same phase. In case of magnetoelectric multiferroic materials, the magnetic and electric orderings present different microscopic origins and their existence are independent from each other. In such case, the self-excluding properties of electric and magnetic orders make these materials quite rare and, in general, their electric polarizations are strong, whereas the magnetoelectric coupling is very weak in comparison to type-II multiferroics. In those compounds, the ferroelectric ordering arises due to electronic lone pairs, geometric effects or charge orderings[16]. A classic example of this family of compounds is the $BiFeO_3$.

These are the materials in which one of the coupled ordering is originated from the other, making a mutually dependent existence of ferroic orders. In case of magnetoelectric multiferroic materials, the electric and the magnetic ordering emerge jointly[16], which originates a strong magneto-electric coupling[21].

In these materials, the electric polarization can be induced by the magnetic ordering through inverse Dzyaloshinskii-Moriya interactions (inverse DM interactions), where $P_{ij} \propto e_{ij} \times (S_i \times S_j)$;[†] exchange strictions (magnetostriction effect), where $P_{ij} \propto \prod_{ij}(S_i \cdot S_j)$;[†] or p-$d$ metal-ligant orbitals hybridization, $P_{il} \propto (S_i \cdot e_{il})^2 e_{il}$ [†](Figure 1.9).

[†] Deeper information about the spin-induced polarization in such cases are given in reference [162]

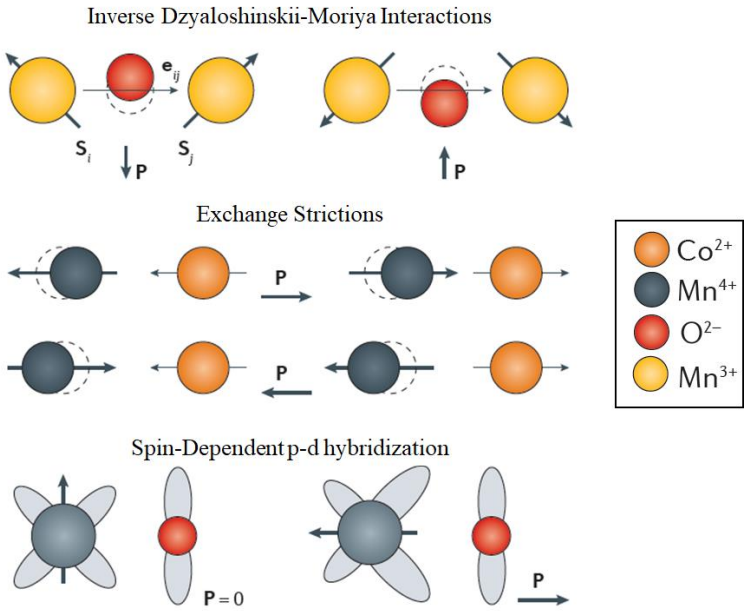

Figure 1.9. Possible spin-driven electric polarizations in multiferoic type-II materials. (adapted from reference [16])

1.4 *The Spin-phonon Coupling*

The coupling between the magnetic order and the electric order in magnetoelectric materials open the possibility of a magnetic ordering also coupled with the crystal lattice. The spin-lattice coupling in the multiferroic magnetoelectric materials can contribute significantly to the interplay between the electric polarization and the magnetic ordering[23]. In this way, the spin-phonon coupling investigation is applied as a probe to identify the nature and magnitude of spin and lattice interactions originated by this kind of multiferroic behavior[24]. Thus, in this section is shown an introduction to this coupling phenomenon.

In absence of phase transitions and other external phenomena, the temperature-depended Raman spectrum of a given compound is dominated by the anharmonic effects of its phonons. In this way, a simplified approximation to describe this complex phonon anharmonic contribution to the temperature dependent behavior of the phonon features was reported by Hart *et al*[25] and then, expanded by Balkanski *et al*[26] in order to take into account the four-phonons interaction. In this model, the temperature dependence of the full width at half maximum (FWHM) and center of a given phonon mode are given, respectively, by:

$$\Gamma(T) = A\left[1 + \frac{2}{e^{x} - 1}\right] + B\left[1 + \frac{3}{e^{y} - 1} + \frac{3}{(e^{y} - 1)^{2}}\right] \quad (1.5)$$

$$\omega(T) = \omega_0 + C\left[1 + \frac{2}{e^{x} - 1}\right] + D\left[1 + \frac{3}{e^{y} - 1} + \frac{3}{(e^{y} - 1)^{2}}\right] \quad (1.6)$$

where A, B, C, D and ω_0 are fitting parameters and $x = \hbar\omega_0/2k_BT$ and $y = \hbar\omega_0/3k_BT$.

The model presented by equations (1.5) and (1.6) describes very well the temperature dependent behavior of their respective phonons parameters as can be seen in Figure 1.10 (a) and (b). Also it shows that the four-phonon term included in that expansion becomes crucial when the systems are submitted to high temperatures. As an example of the applicability of models proposed by equations mentioned above, in the panels (c) and (d) of Figure 1.10 is shown the temperature dependent frequency and FWHM (respectively) of *o*-$TmMnO_3$ perovskite synthesized in this study. Although the samples studied here were not submitted to temperatures well above the room temperature, those figures illustrate the phonons behavior below room temperature. Based in these considerations, the models proposed by Balkanski *et al*[26] were adopted here to describe the temperature dependence of fundamental phonons features.

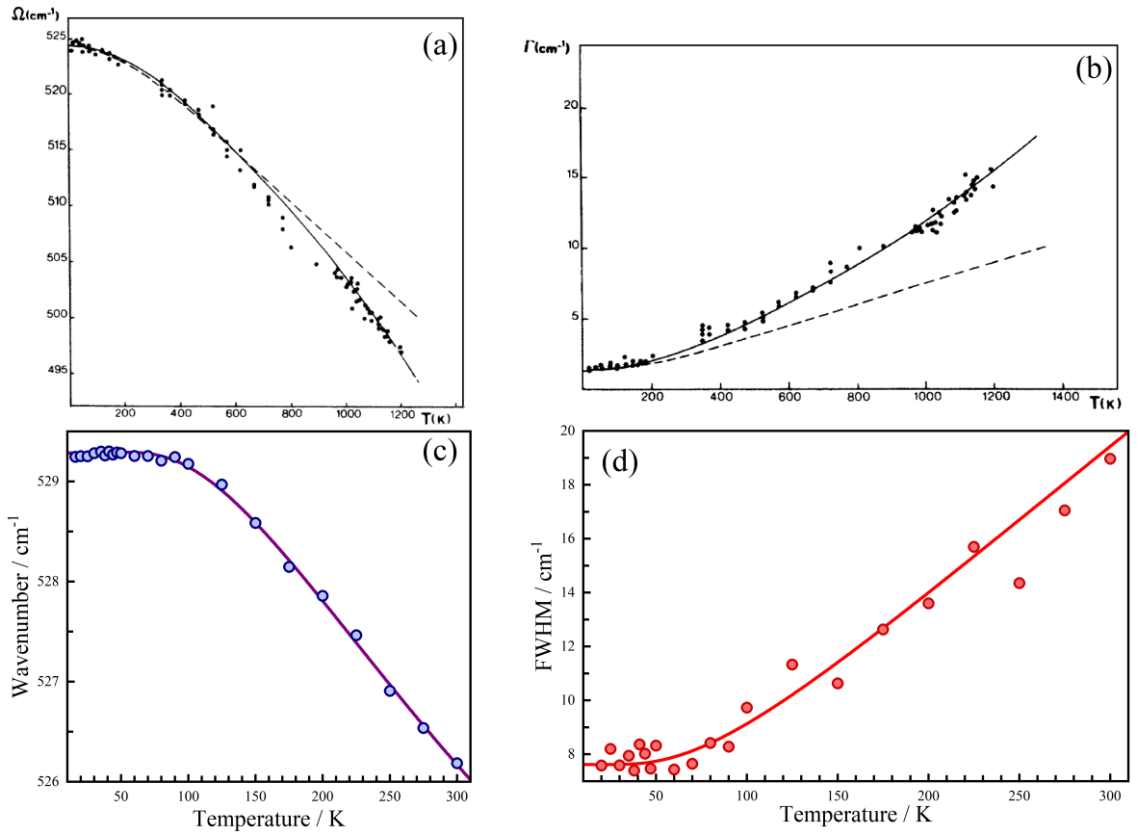

Figure 1.10. Panels (a) and (b) are showing the center and FWHM, respectively, reported by Balkanski et al[26], while the panels (c) and (d) are showing the center and FWHM fitting by using the equations (1.5) and (1.6) for *o*-$TmMnO_3$ synthesized in this work. (Panels (a) and (b) are adapted from Balkanski et al[26])

As mentioned before, the temperature dependent behavior of phonons features is often changed for several reasons. In the case of magnetic materials, the changes on temperature dependent frequency of a phonon α described by equation (1.6), can be related as reported by Granado *et al*[27]:

$$\Delta\omega_\alpha(T) = (\Delta\omega_\alpha)_{latt} + (\Delta\omega_\alpha)_{anh} + (\Delta\omega_\alpha)_{ren} + (\Delta\omega_\alpha)_{s-ph} \qquad (1.7)$$

According to the authors, the $(\Delta\omega_\alpha)_{latt}$ term in equation (1.7) is related to the contribution due to changes of ionic binding energies due to lattice variations. Thus, this term takes in consideration the contributions due to expansions or contractions on the crystalline lattice, which can be originated by ananharmonicity of crystal and/or magnetostriction effects. The second term ($(\Delta\omega_\alpha)_{anh}$) is related to the intrinsic anharmonic frequency shift of such phonon at constant volume. The third term ($(\Delta\omega_\alpha)_{ren}$) relates the phonon frequency to renormalizations of electronic states that occur near the spin ordering temperature, and, finally, the spin-phonon coupling

contribution is included to the fourth term ($(\Delta\omega_\alpha)_{s-ph}$), being caused by the modulation of the exchange integral by the lattice vibrations.

The spin-phonon coupling is identified as changes in temperature-dependent phonons parameters. These changes can be frequencies, lifetime or integrated intensity and, generally, appears at temperatures nearby the magnetic ordering temperature.

In a general way, the phonon renormalization of a given temperature dependent phonon frequency ($\Delta\omega$) can be described taking into account the spin-spin correlation function[28,29]:

$$\Delta\omega = \lambda\langle \boldsymbol{S}_i \cdot \boldsymbol{S}_j \rangle \tag{1.8}$$

where λ is the coupling constant and $\langle \boldsymbol{S}_i \cdot \boldsymbol{S}_j \rangle$ is the spin correlation function, which denotes a statistical-mechanic average for adjacent spins moments. Thus, in the paramagnetic phase, there is no spin ordering and the $\langle \boldsymbol{S}_i \cdot \boldsymbol{S}_j \rangle$ term vanishes, whereas in magnetically ordered phases, it is expected that the spin-phonon coupling generate an additional contribution to the phonons frequencies.

By means of mean field theory, the spin correlation function on equation (1.13) can be related to $(\langle S^Z \rangle / S)^2$, where $\langle S^Z \rangle$ is calculated by using the Brillouin function[27,30,31]. Thus, the magnetization is given by the Brillouin function in the form[13,14]:

$$M = M_0 B_j(x) \tag{1.9}$$

The M_0 factor in equation (1.9) is the saturated magnetization and is defined as $M_0 = ng\mu_B J$, where n is the number of magnetic ions, g is the Landé factor, μ_B is the Bohr magneton and J is the total angular moment. At zero external field, the spontaneous magnetization ($M(T)$) and can be written as[13]:

$$\frac{M(T)}{M_0} = \frac{M(T)}{ng\mu_B J} = \langle S^Z \rangle \tag{1.10}$$

Thus:

$$\langle \boldsymbol{S}_i \cdot \boldsymbol{S}_j \rangle = \left(\frac{\langle S^z \rangle}{S}\right)^2 = \left(\frac{M(T)}{n} \cdot \frac{1}{gJS\mu_B}\right)^2 \tag{1.11}$$

or alternatively:

$$\langle S_i \cdot S_j \rangle = \left(\frac{M_{sublatt}}{C\mu_B}\right)^2 \tag{1.12}$$

where C is a constant which depends on the magnetic ion including g, J and S factors, while $M_{sublatt}$ is the net magnetization per unit of magnetic ions.

Granado *et al*[27] reported an approach to describe the spin-phonon coupling in perovskite compounds showing the form of the λ coupling constant in equation (1.8). Such model present the frequency renormalization of an α phonon frequency due to a spin-phonon coupling (equation (1.8)) is given by:

$$\Delta\omega = -\frac{N}{2\mu_\alpha\omega_\alpha}\sum_{i,j}\frac{\partial^2 J_{ij}}{\partial u_\alpha^2}\langle \boldsymbol{S}_i \cdot \boldsymbol{S}_j \rangle \tag{1.13}$$

or:

$$(\Delta\omega_\alpha)_{s-ph} = -\frac{N}{2\mu_\alpha\omega_\alpha}\sum_{i,j}\frac{\partial^2 J_{ij}}{\partial u_\alpha^2}\left(\frac{M_{sublattice}}{C\mu_B}\right)^2 \tag{1.14}$$

where N is the number of magnetic ions and u_α is the displacement vector of a α phonon mode.

Several authors have been using the magnetic contribution for the frequency deviation as described by the equation (1.14)[27,32–34]. Alternatively, other authors[35–41] has been reported the deviation on phonon frequencies as proportional to $(M(T)/M_0)^2$, as described by equation (1.10), giving:

$$(\Delta\omega_\alpha)_{s-ph} = -\frac{N}{2\mu_\alpha\omega_\alpha}\frac{\partial^2 J_{ij}}{\partial u_\alpha^2}\left(\frac{M(T)}{M_0}\right)^2 \tag{1.15}$$

The two approaches are similar, differentiating themselves only in the way that the terms included in the saturated magnetization are arranged to $M(T)$.

As can be seen from equation (1.13)(1.14), the λ factor on equation (1.8) depends not only on the magnetic order but also on the character of the phonon[32]. A systematic trend on the renormalization of phonon frequencies was observed in a large number of compounds in which the spin-phonon coupling was confirmed. Usually, in ferromagnetic materials, a softening effect on phonon frequencies is observed[42,43], inducing the idea of $\lambda < 0$, whereas in antiferromagnetic systems, there is a hardening effect[35], inducing

$\lambda > 0$. However, due to the complex character of the λ coupling constant involving the second derivate in relation to phonon , the finding of compounds which are exceptions to this rule is not surprising[31,39,40,44,45].

The model proposed by Granado *et al*[27] has been effective to describe the spin-phonon coupling in several perovskite compounds e. g. $LaMnO_3$[27], Y_2NiMnO_6[42], $Gd(Co_{1/2}Mn_{1/2})O_3$[39], La_2NiMnO_6[43], Gd_2NiMnO_6[46] and Y_2CoMnO_6[47] as well as for non-perovskite compounds such as NiO[45] and $ZnCr_2O_4$[48].

However, in the case of incommensurate magnetic orderings, an extension of this model becomes necessary. As mentioned in section 1.1, in such cases, the spin moments are organized as wave functions whose wavelength is not an integral number of the crystal lattice[14]. Then, the spin moments now are described in terms of a propagation vector in the form $\boldsymbol{k}_s = (k_x, k_y, k_z)$. Once the spin alignment in those materials are not constant along the unit cell, a modification to the standard mean field theory approach becomes necessary to estimate the character of $\langle \boldsymbol{S}_i \cdot \boldsymbol{S}_j \rangle$. In this way, an expansion of the previously model was reported by Lavèrdiere *et al*[49], in which the spin correlation function in equation (1.13) is given by:

$$\langle \boldsymbol{S}_i \cdot \boldsymbol{S}_j \rangle = K(T)\cos(2\pi \boldsymbol{k}_S \cdot \boldsymbol{r}) \tag{1.16}$$

where $K(T)$ is a temperature-dependent prefactor that is proportional to the square of sublattice magnetization ($K(T) \propto M_{sublatt}^2$).

In this way, for incommensurate systems, the equation (1.17) becomes:

$$(\Delta\omega_\alpha)_{s-ph} = -\frac{1}{2\mu_\alpha \omega_\alpha} \sum_{i,j} \frac{\partial^2 J_{ij}}{\partial u_\alpha^2} [\cos(2\pi \boldsymbol{k}_S \cdot \boldsymbol{r})] \big(M(T)\big)^2 \tag{1.17}$$

Following this approach, the spin-phonon coupling for incommensurate systems should be described in the form of equation (1.17). Such equation is an expansion of that one reported by Granado et al[27] and, as such, this relation becomes the one expressed by equation (1.17) for determined systems as described by reference [49].

2. METHODOLOGY

The aim of this thesis is to synthesize and characterize different compounds in order to contribute to the understanding of different physical features presented by the proposed compounds. Such analysis was planned to involve different experimental and theoretical approaches in order to analyze the interesting features of intended samples. In this section, these different techniques used to perform the intended synthesis and characterization will be presented.

2.1 *X-ray powder Diffraction*

In this study the X-ray Powder Diffraction (XRPD) analyze was employed to evaluate the structural properties and confirms the formation of intended compounds after synthesis procedures. The equipments used for these analyses were available at the Federal University of Ceará, at Centre of Science at Extreme Conditions (CSEC) and School of Chemistry of The University of Edinburgh and at the Brazilian National Synchroton Light Source Laboratory (LNLS).

2.1.1 X-Ray Powder Diffraction measurements

In order to check the samples formation after synthesis procedures, X-Ray Powder Diffraction (XRPD) measurements were carried out by using a conventional D8 Advance (Bruker) diffractometer equipped with a θ/θ goniometer and a Cu source ($K\alpha_1$ 1.5406 Å). In addition, a Bruker D2 PHASER diffractometer with a Cu source ($K\alpha_1$ 1.5406 Å and $K\alpha_1$ 1.544300 Å) also was employed to perform fast XRPD analysis on as-synthetized samples by means of HPHT treatments.

The phase analysis and impurities formula weight of XRPD patterns were analyzed through Rietveld Refinements made through the graphical user interface EXPGUI[50] and the Generalized Structure Analysis System (GSAS)[51] software.

2.1.2 Synchrotron X-Ray powder diffraction measurements

In order to obtain more precise information about the crystalline structures presented by the samples synthesized here, high-resolution synchrotron X-ray Powder Diffraction (SXRPD) measurements were carried out. In addition, the pressure-dependent behavior of synthesized samples also was monitored through synchrotron X-ray measurements.

The pressure dependent XRPD measurements were performed in XDS beamline at Brazilian Synchrotron Light Source Laboratory (LNLS) with a monochromatic synchrotron radiation λ = 0.619999 Å. This beamline employs a 4T superconducting multipolar wiggler (SCW) as photon source and operates in the energy range between 5 and 30 keV.

The high pressures experiments were carried out by using a gas-membrane diamond anvil cell (DAC), where the sample was placed together a small piece of ruby (whose emission lines were used as pressure reference) in a metallic gasket. I such experiments the mineral oil (Nujol) and He gas were used as hydrostatic medium. In this configuration, the X-rays are transmitted through the diamonds and sample and collected in an area detector MarCCD MX225 (Rayonix, LLC).

The free software Fit2D (version 18.002)[52] was used to obtain the center of synchrotron beam radiation at the are detector, while the Dioptas (version 0.4.1)[53] was employed to integrate the SXRPD pattern into 1D spectra. In addition, the Le Bail method [54] was performed to obtain structural information using the software package FullProf[55].

2.2 *Magnetic Susceptibility Measurements*

The magnetic properties of synthesized samples, magnetic measurements were carried out monitoring the temperature dependent behavior of magnetic susceptibility and the magnetic answer under magnetic field variations in order to analyze the magnetic ordering temperatures.

The magnetic properties of synthesized samples were analyzed in a superconducting quantum interference device (SQUID) magnetometer model Quantum Design MPMS XL7 analyzing DC susceptibilities and a Physical Properties Measurement System (PPMS) from Quantum Design for AC susceptibility analyzes. Both types of equipment were cooled through liquid Helium in which the temperature controller was calibrated in order to obtain a precision of 0.1 K. All equipment used to analyze the magnetic properties were available at the Centre of Science at Extreme Conditions (CSEC) of the school of chemistry at Edinburgh University.

2.3 *Raman Spectroscopy*

Raman spectroscopy is a non-destructive technique widely used to study molecular and crystal lattice vibrations. Raman spectroscopy also is known as a sensitive technique for detecting phase transitions or subtler structural rearrangements due to magnetic transitions and coupling phenomena. In this way, this is a powerful technique to investigate the spin-phonon coupling of multiferroic magnetoelectric materials.

Raman spectroscopy measurements were performed at the Federal University of Ceará and in collaboration with Federal University of Maranhão. In both cases, the measurements were performed using Jobin-Yvon T64000 Triple Spectrometers configured in a backscattering geometry coupled to an Olympus Microscope model BX41 with a 20x long-working distance achromatic objective. The 532 and 633 nm emissions lines of HeNe gas lasers were used for spectra excitation. The lasers powers were kept below 2 mW to avoid the local heating of samples. In addition, all slits were set up to achieve a spectral resolution better than 1 cm^{-1}. Temperature-dependent Raman measurements from 16 up to 300 K were carried out by using a closed-cycle He cryostat in which the temperature was controlled by a Lakeshore temperature controller model 330 with a precision of 0.1 K.

In order to obtain more precise information about the center, FWHM and peaks intensity of phonons modes presented by Raman spectra obtained here, these spectra were deconvoluted into Voigt and/or Lorentzian functions by means of Fityk software (version 0.9.8)[56].

2.4 *Synthesis Methods*

In this study, were used two different kinds of synthesis procedure: the standard solid-state reaction in ambient atmosphere, and the solid state reaction under high pressure and high temperatures. The first one was performed at Federal University of Ceará, Brazil, as well as in the Centre of Science at Extreme Conditions (CSEC) at The University of Edinburgh, United Kingdom, while the second one only was done at CSEC. The following sections are dedicated to giving more details about each technique.

2.4.1 Solid State Reaction

This method consists of the mixture of two or more reagents (in form of powder) in appropriate stoichiometric ratios. The powdered mixture is pressed in pellet and are placed in the oven at fixed temperatures. The heating rate is adjusted to the most suitable conditions of each sample.

Conventional ovens for laboratories were used for the solid-state reaction synthesis adopted in this study. Such ovens allow synthesis with different levels of permanence with independent durations and different temperature rates.

2.4.2 Solid State Reaction under High-Pressure and High-Temperature (HPHT)

In the past years, the synthesis science has been developed to find ways to overcome the difficulties to obtain technologic interesting multiferroic compounds whose characteristics seem to be competitive between themselves. The main issue is represented by the difficulty to observe a high-temperature multiferroic phase and a high magnetoelectric coupling on the same material. However, as mentioned before, the majority of those compounds are complex and rarer in Nature. In addition to this scenario, the standard high-temperature synthesis under controlled atmosphere is becoming saturated in the production of new physical and technologically innovative materials.

In this way, the developing of apparatus capable to provide novel synthesis conditions to reach the limits of synthesis parameters become the center of interest of material science. The first successful prototype for this type of apparatus was developed in the 70’s, since this, the research to improve those high pressure and high-temperature configurations have been developed by researchers around the world[57]. Among the developed devices, the Multianvil apparatus belongs to the class of devices used for the generation of high pressures in laboratories. This apparatus also belong to the class of

devices of high pressure called large volume press (LVP)[58]. This classification is given by the pressurized volume, which is of the order of millimeters, differently from diamond anvil cells, for example, in which the pressurized volume is on the order of micrometers[59,60].

There are at least two types of configuration to multianvil apparatus to achieve high pressures on large volumes. One of those is the cubic geometry, more commonly called as DIA geometry. On these systems, an octahedral cavity pushes 6 wedges which, in turn, push a cubic gasket in each face. In 1995, Kat et al[61] reported a modification in this system adding eight cubes in sample region allowing in-situ x-ray analysis on pressures up to 25GPa.

However, the most common device used in high-pressure laboratories is the 6-5 anvil system. This configuration was developed by Kawai and Endo[62] and consist in a cubic cavity containing 6 anvils pushing the second stage of 8 anvils pushing an octahedral gasket in 8 different directions (Figure 2.1).

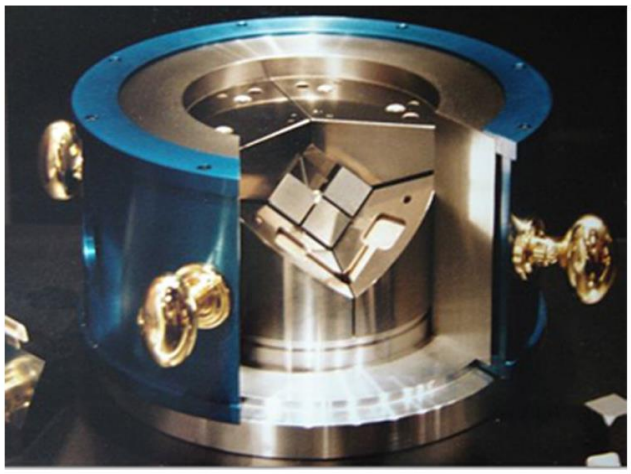

Figure 2.1. Schematic configuration of a Walker-type Multi-Anvil apparatus.

Based on this 6-8 configuration, the apparatus utilized on this research to perform the synthesis of multiferroics through high-pressure / high-temperature conditions was the Multi-Anvil Walker-type press, located at the Centre of Science at Extreme Conditions (CSEC), in the School of Chemistry of the Edinburgh University, Scotland – UK.

This apparatus is a versatile system for the syn thesis of bulk materials under variable isotropic pressure and temperature conditions in the range of 3 < Pressure < 22 GPa and 300 < Temperature < 2273 K.

The Walker-type module is able to convert an axial load over circular surface into a three-component force through a set of six wedges, made of tempered steel. The combination of these wedges generates a cubic cavity to be filled by eight truncated tungsten carbide cubes which, in turn, are assembled together to create an inner octahedral cavity with four resultant force directions. Inside this cavity is put the reaction cell, a magnesium oxide octahedron pierced at the center of two of its parallel faces from one side to other in a cylindrical cavity in which is located the graphite sample oven. The graphite sample oven, for once, consists of a cylindrical graphite tube filed in accord with the schematic diagram shown in Figure 2.2.

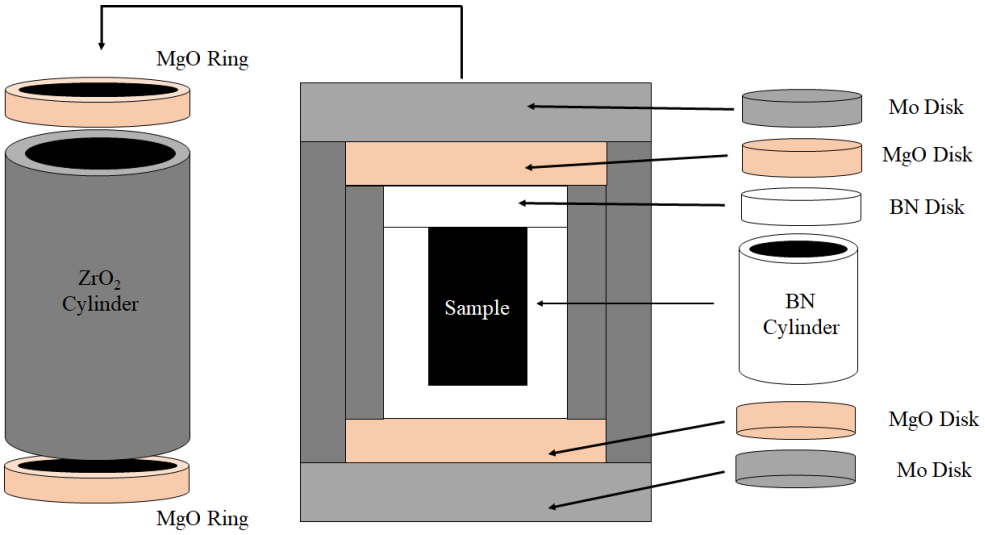

Figure 2.2. Schematic model for reaction cell used in HPHT treatments.

In these systems, the heating is achieved by Joule effect by means of a power unit that connects the upper and lower wedges via a non-insulated path which goes through the two opposite cubes until the pierced octahedral reaction cell connected by the two exposed surface of graphite sample oven. This electrical control of temperature was developed in order to manage the temperature in the vicinity of the reaction cell center, without heat dispersions along the massive anvil structure.

The typical synthesis procedure can be schematized into three sequential operations as described by Delmonte[63]:

1. The pressure is gradually increased from ambient pressure to the set-point of reaction pressure in an appropriate ramp in order to reach the desired pressure

2. Once the set-point pressure is reached, the system is Joule-heated from room temperature to the chosen set-point temperature (in a specific and appropriate range) where the system will be kept stable for the chosen reaction time (usually a few hours).
3. At the end of reaction, the system is abruptly quenched down to room temperature by switching off the power unit and the pressure is slowly released to ambient pressure with appropriate rate.

3. Spin-phonon coupling in melanothallite Cu_2OCl_2

In the field of multiferroic materials, the magnetodielectric materials have been attracting the attention of the scientific community because of their applications as spintronics, magnetic field sensors, memory devices and photovoltaic solar cells[4,20,64–68]. Concerning magnetodielectric applications, a large coupling is a key feature for devices with enhanced efficiency. In type-II multiferroics, in which the ferroelectricity is due to the magnetic ordering, this kind of coupling is natural. However, in contrast to the high magnetodielectric coupling, usually, type-II multiferroics exhibits low critical temperatures[69–72], which have limited their applications.

Recently, Zhao et al[73] showed that the melanothallite oxyhalide Cu_2OCl_2 is a spin-driven magnetodielectric multiferroic, which has a quite high critical temperature when compared to other type-II multiferroics and whose ferroelectricity emerges at $T_N \approx 70\ K$. It was also observed, using powder neutron diffraction measurements, that the magnetic structure is incommensurate below T_N, which is in disagreement with previously reported pyrochlore-like all-in-all-out spin structure. This spin structure shows that Cu_2OCl_2 is, in fact, a spin-induced multiferroic material.

At room temperature Cu_2OCl_2 crystallizes in an orthorhombic structure belonging to the *Fddd* space group and has lattice parameters $a = 7.469(2)$ Å, $b = 9.597(2)$ Å and $c = 9.700(2)$ Å; with 8 molecules per unit cell[74]. This structure, called melanothallite, can be seen in two forms. In the first one each Cu ion is coordinated to two oxygen and two chlorine ions forming CuO_2Cl_2 squares chains running along [110] and equivalent directions (Figure 3.1 (a)). In the second one, the structural configuration of Cu_2OCl_2 is described as O ions tetrahedrally coordinated by Cu ions forming a corner-sharing 3D network, while chlorine ions are located in the free space between the OCu_4 tetrahedra (Figure 3.1 (b)).

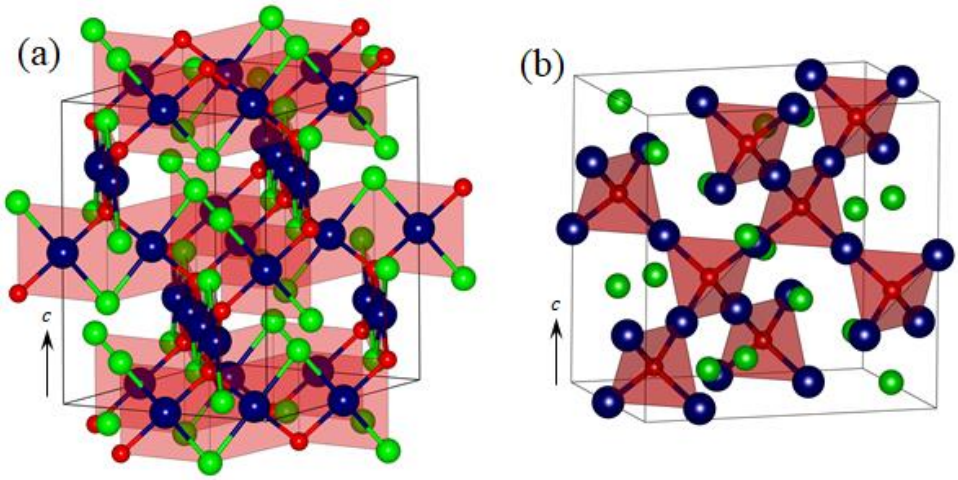

Figure 3.1. Unit cell of melanothallite Cu_2OCl_2 presented as (a) squares of CuO_2Cl_2 and (b) OCu_4 thetraheda. Blue spheres represent the Cu atoms; the green spheres represent Cl atoms, and red spheres are the O atoms.

3.1 *Cu_2OCl_2 Synthesis Procedure*

Cu_2OCl_2 polycrystalline samples were synthesized through the conventional solid-state reaction method using an equimolar mixture of $CuCl_2$ (Sigma-Aldrich 99.99%) and CuO (Sigma-Aldrich 99.99%). The starting materials were grounded in an agate mortar and pressed into pellets. Afterward, the pellets were sintered at 350 ºC under a heating rate of 3 ºC per minute, when were maintained on this temperature for 24 hours. Then, the pellets were quenched until 100 ºC on the rate of 2 ºC per minute. Once the samples presented a strong hygroscopic characteristic, the synthesized samples were removed from the oven at 100 ºC and deposited into a desiccator with silica gel to remove ambient moisture. To confirm the melanothallite Cu_2OCl_2 synthesis, samples were grounded and placed into capillaries sealed with silicone grease for Powder X-ray diffraction measurements. The X-ray analyses were performed in a Bruker D8 Advance diffractometer (Cu Kα1) on Centre of Science at Extreme Conditions (CSEC) of School of Chemistry at The University of Edinburgh.

3.2 *Results and Discussions*

The X-ray powder diffraction pattern obtained for the synthesized Cu_2OCl_2 sample is shown in Figure 3.2. This result confirms that the adopted synthesis method was enough to synthesize the melanothallite Cu_2OCl_2. In addition, the PDRX also revealed a small amount of CuO, which could be associated as impurity or a secondary

phase. Nevertheless, the existence of secondary phases is common for synthesis through solid-state reaction procedure.

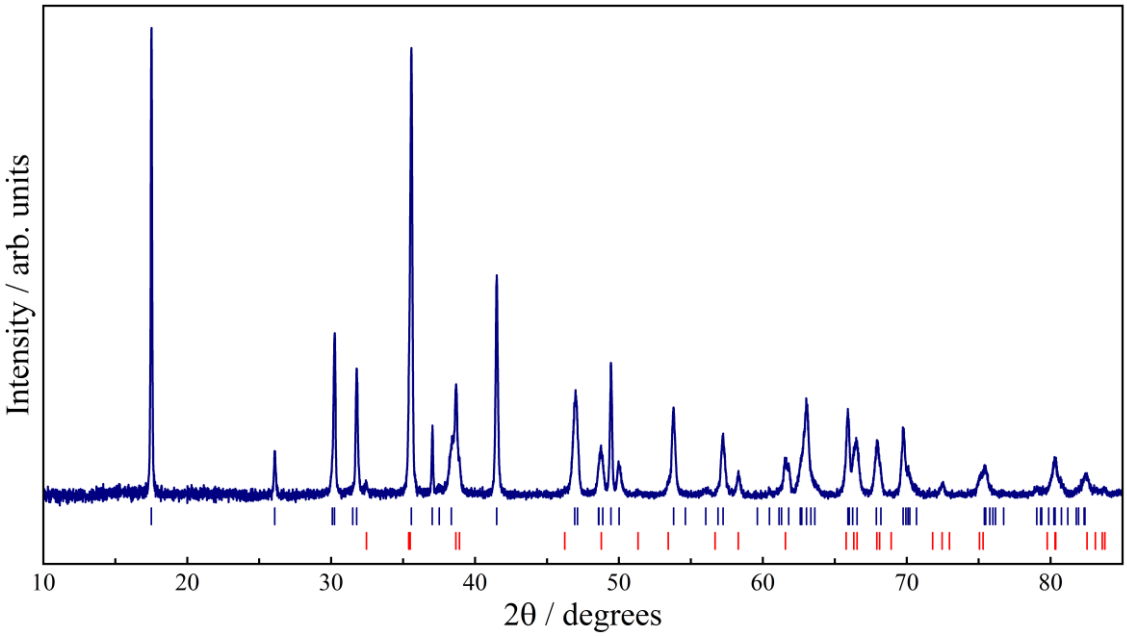

Figure 3.2. Cu_2OCl_2 X-ray powder diffraction pattern compared with its reported structure[74] (ICSD - 96610), indicated by the dark blue bars, and CuO (ICSD - 64699), indicated by red bars, as minor secondary phase peaks.

To analyze the magnetic profile of Cu_2OCl_2 sample, the synthesized compound was analyzed although magnetization curve extrapolated from Zero Field Cooled (ZFC) results. Then, the magnetization results of Cu_2OCl_2 synthesized in this study were compared to the one reported by Zhao et al[73] (Figure 3.3). As can be observed, the behavior of our sample is similar to that one reported in the literature and the magnetic ordering temperature (T_N) of Cu_2OCl_2, determined by the maximum slope of the temperature dependent magnetization, is around 68 K in good agreement with previous studies[73,75].

The magnetic profile of Cu_2OCl_2 also was analyzed to investigate the influence of CuO impurity originated from the adopted synthesis method. It is reported in the literature that this compound exhibits two antiferromagnetic transitions $T_{N1} = 230$ and $T_{N2} = 210\ K$[76–78]. Once no anomalies nearby the T_{N1} and T_{N2} of CuO can be observed in our magnetic measurements, we can conclude that the residual presence of CuO has no influence on magnetic behavior of on synthetized Cu_2OCl_2 samples.

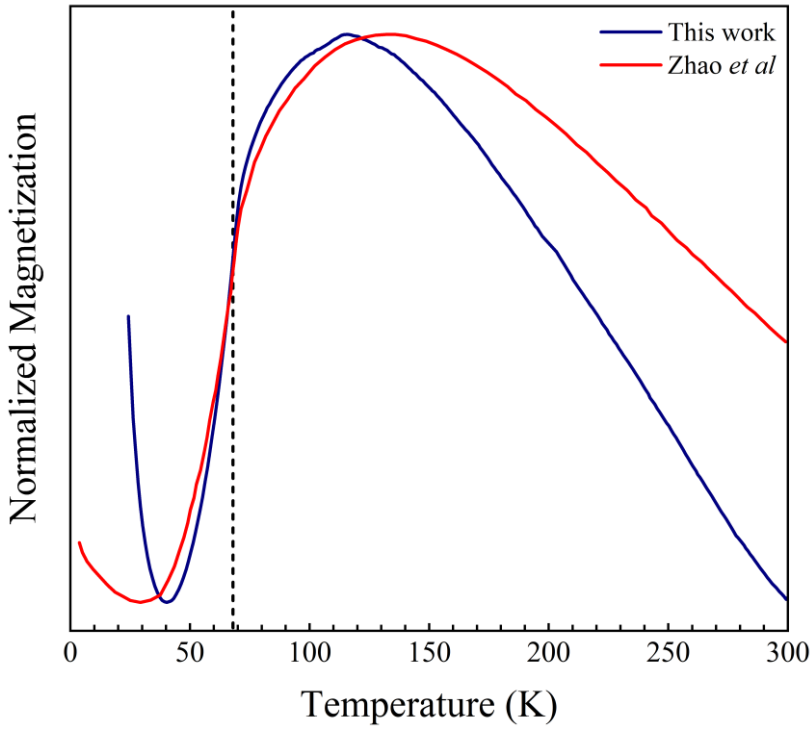

Figure 3.3. The magnetization of Cu_2OCl_2 synthesized in this work compared to the one reported by Zhao et al [73].

Another interesting feature about the magnetic behavior of Cu_2OCl_2 is related to the non-null magnetization value above T_N, region that corresponds to the paramagnetic phase where no magnetic response was expected. The Cu_2OCl_2 analysis of temperature dependent magnetization analysis shows a broad maximum around 140 K. Such broad response is commonly observed in low-dimensional materials as $CuGeO_3$[79] or TiOCl[80], whose structures are constituted by linear chains. As mentioned before, the structure of Cu_2OCl_2 also can be described by cross-linked chains of edge-sharing CuO_2Cl_2 squares running along [110] and equivalent directions (Figure 3.4). Thus, this broad maximum behavior could be related to the low dimensionality of these CuO_2Cl_2 squares chain[75].

In this system, there are three neighboring Cu ions with atomic distances of 3.04, 3.06 and 3.41 Å configuring two intrachain exchange paths and two interchains exchange paths, as shown in Figure 3.4. The intrachain exchanges are $J_{intra}^{(1)}$ and $J_{intra}^{(2)}$, being related to Cu-O-Cu (3.9445 Å and 102.84 º) and Cu-Cl-Cu (4.5672 Å and 83.46 º) paths, respectively. While the interchains are $J_{inter}^{(1)}$ and $J_{inter}^{(2)}$ related to 103.8º and 122.6°, respectively, angles of Cu-O-Cu interchains paths.

Based in this, the magnetic behavior of Cu_2OCl_2 was analyzed by Okabe *et al*[75] taking into a count the contribution of these two kinds of chains interactions. In that work,

the authors fitted the magnetic susceptibility (χ) following the models for the classical $S = 1/2$ linear chain, which do not includes the interchain interactions, and the mean field corrected chain model, which includes the interchain interactions[81,82].

Once the classical $S = 1/2$ linear chain did not include the interchain interactions to the magnetic susceptibility of a system, these models are the key analysis to determine the role of interchain interactions for the magnetic behavior. However, it is important to note that, since these models consider the magnetic effect of low dimensional chains, they describe the temperature magnetic behavior where there is not a long range magnetic order, as ferro or antiferromagnetic orderings, making those contributions negligible when compared to well oriented spin alignments.

Based on fit adjustments, by using the two previously cited models, Okabe *et al*[75] concluded that the mean field corrected chain model is the best model to describe the magnetic behavior of Cu_2OCl_2, showing that this melanothallite trend to be a 3D antiferromagnetic system with a strong interchain interactions, instead of a $S = 1/2$ 1D antiferromagnetic Heisenberg linear chain system[75], as proposed by other authors.

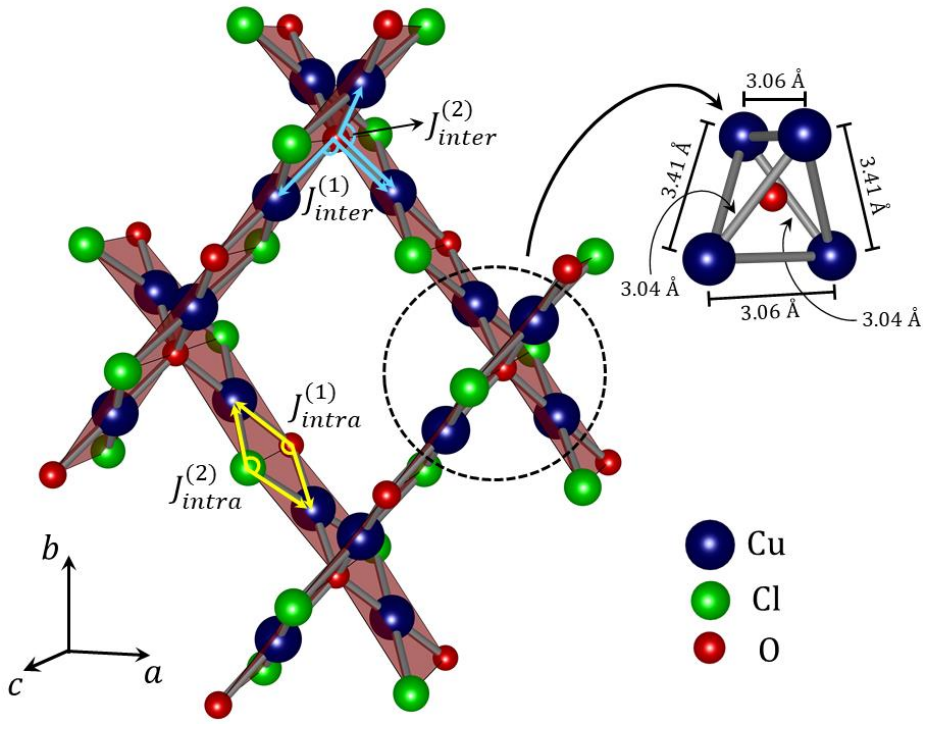

Figure 3.4. Chain structure of Cu_2OCl_2. CuO_2Cl_2 squares are represented in red.

After magnetic analyzes, the Cu_2OCl_2 samples were investigated by Raman spectroscopy. Figure 3.5 shows the room temperature Raman spectrum of the sample, where 8 vibrational modes can be observed, with the most intense one located around 550

cm^{-1}. Based on group theory analysis[83], the distribution of the vibrational modes of Cu_2OCl_2 in terms of the irreducible representations of the D_{2h} group factor is showed in Table 1. Thus, there are expected 9 Raman-active phonons ($A_g \oplus 2B_{1g} \oplus 3B_{2g} \oplus 3B_{3g}$) of mixed symmetries in the Raman spectrum of polycrystalline Cu_2OCl_2 sample, which is in good accordance with our observation.

Table 1. Irreducible representation of vibrational modes for Cu_2OCl_2.

Ion	Site	Symmetry	Contribution
Cu	16d	C_1	$3A_u \oplus 3B_{1u} \oplus 3B_{2u} \oplus 3B_{3u}$
Cl	16g	C_2^2	$A_g \oplus A_u \oplus B_{1g} \oplus B_{1u} \oplus 2B_{2g} \oplus 2B_{2u} \oplus 2B_{3g} \oplus 2B_{3u}$
O	8b	D_2	$B_{1g} \oplus B_{1u} \oplus B_{2g} \oplus B_{2u} \oplus B_{3g} \oplus B_{3u}$
		$\Gamma_{acoustic}$:	$B_{1u} \oplus B_{2u} \oplus B_{3u}$
		Γ_{silent}:	$4A_{1u}$
		Γ_{IR}:	$4B_{1u} \oplus 5B_{2u} \oplus 5B_{3u}$
		Γ_{Raman}:	$A_g \oplus 2B_{1g} \oplus 3B_{2g} \oplus 3B_{3g}$
		Γ_{TOTAL}:	$A_g \oplus 4A_{1u} \oplus 2B_{1g} \oplus 5B_{1u} \oplus 3B_{2g} \oplus 6B_{2u} \oplus 3B_{3g} \oplus 6B_{3u}$

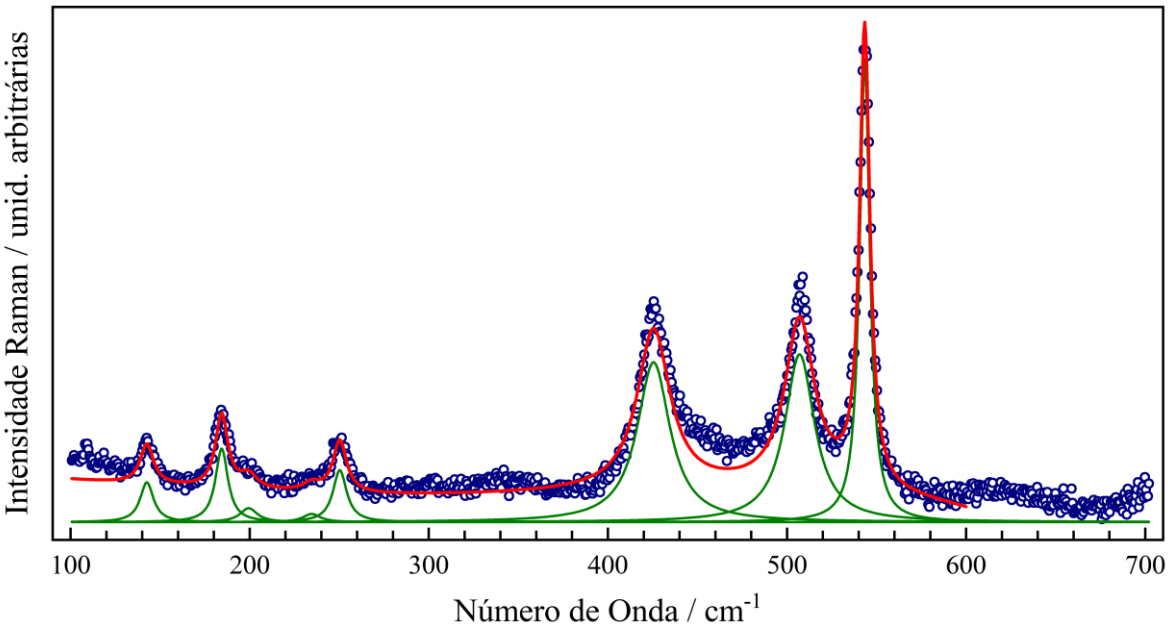

Figure 3.5. Raman spectrum of Cu_2OCl_2 at room temperature.

The Raman results were also analyzed in order to investigate the effect of the presence of CuO impurity on Cu_2OCl_2 samples. At room temperature, the monoclinic

phase of CuO present the C_{2h}^{6} (*C2/c*) space group with two molecules per unit cell. Its group theory analysis predict 3 Raman-active modes at the center Γ point of Brillouin zone, which irreducible representations are $A_g \oplus 2B_g$. Several authors studied the polarized Raman scattering of CuO in nanocrystals, single crystals and polycrystalline samples of CuO[84–88]. These studies present good agreement between themselves, showing that CuO crystals have the most intense A_g mode located at 296 cm^{-1} and two weaker B_g modes located at 344 and 629 cm^{-1}. In our study no one of those three vibrational modes was observed with good enough intensities on the region between 290 and 350 cm^{-1} or around 630 cm^{-1} (Figure 3.5), indicating that the CuO impurity also has no influence on Raman scattering results presented here.

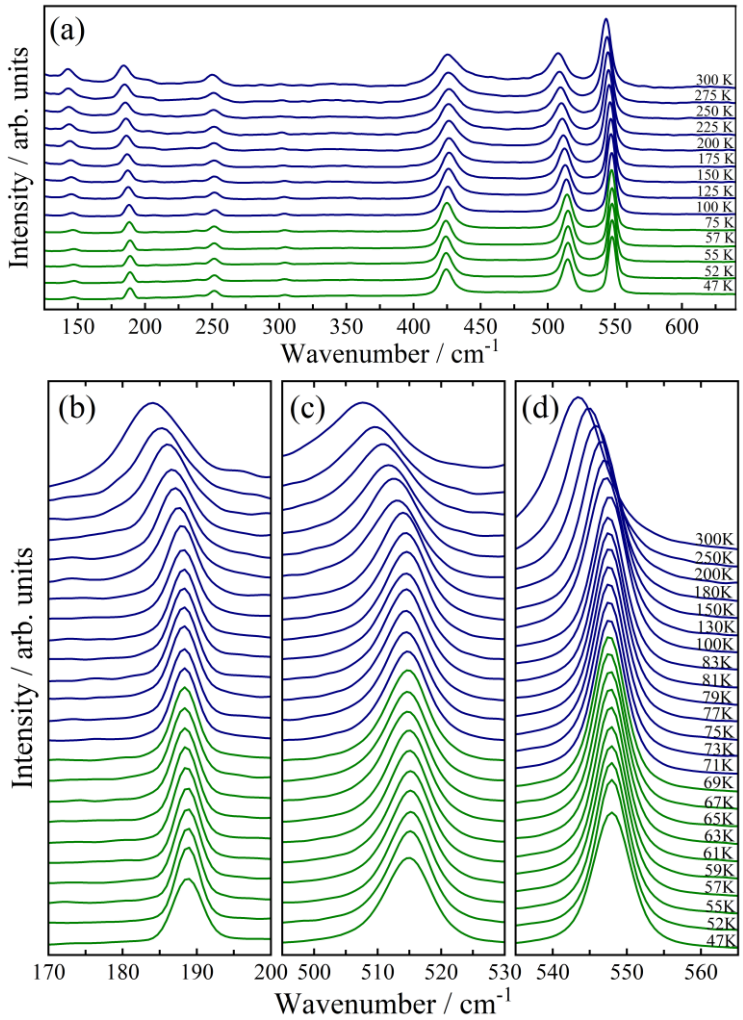

Figure 3.6. Temperature-dependent Raman spectra o Cu_2OCl_2. (a) The overall appearance of Raman spectra during cooling experiments; temperature dependence of phonon positions for the modes located at (c) 185 cm^{-1} (c) 515 cm^{-1} and (d) 545 cm^{-1}.

The temperature dependent Raman spectra of Cu_2OCl_2 was investigated on interval between 300 and 47 K. As expected, since Cu_2OCl_2 does not undergo any structural phase transition in the temperature range investigated, the Raman spectra did not show any remarkable change and the overall appearance of spectra is maintained during all interval of temperature investigation (Figure 3.6(a)).

In absence of structural phase transitions, the temperature-dependent behavior of a phonon mode with frequency ω is mainly defined by the phonon anharmonicity according to Balkanski's model given by equation (1.6) [26]. A detailed analysis of the temperature dependence of some phonon positions observed in Cu_2OCl_2 is showed in Figure 3.7 (a-c).

In these analysis, there are clear deviations of measured phonon positions (indicates by circles) from the one expected behavior in case of process only determined by anharmonic contributions (indicated by solid lines). The starting point of these effects coincides with the Néel temperature of Cu_2OCl_2, suggesting a spin-phonon coupling between the magnetic ordering and the lattice phonons.

The Full Width at Half Maximum (FWHM) of a phonon is related to the phonon lifetime[89] and, when it shows anomalies at the magnetic transition temperature, the observed spin-phonon coupling is usually direct and not mediated by magnetostriction[35]. As mentioned before, Balkanski et al[26] also presented a model to describe the temperature dependence of FWHM for a given phonon mode. This model is given by equation (1.6).

Based on this, the temperature dependent FWHM of Cu_2OCl_2 samples were analyzed and the fitting results are shown in Figure 3.7 (a-c). Clearly, there are anomalies in all analyzed FWHM phonons below 68 K, suggesting that the observed effects are not mediated by magnetostriction, orbital ordering or other lattice effects[27], but only by the long-range antiferromagnetic ordering.

As mentioned before, the renormalization on the phonon frequency in relation to the anharmonic model can be described by taking into account the spin-spin correlation function[28,29]:

$$\Delta\omega \equiv \omega - \omega_0 = \lambda\langle S_i \cdot S_j \rangle \tag{3.1}$$

where ω is the renormalized phonon frequency due to a spin-phonon coupling at fixed temperature, ω_0 is the phonon frequency only due to anharmonic effects), λ is the

coupling constant and $\langle S_i \cdot S_j \rangle$ denotes a statistical-mechanical average for adjacent spins on opposite sublattices. Thus, in the paramagnetic phase, there is no spin ordering and the $\langle S_i \cdot S_j \rangle$ term vanishes, whereas, in the magnetically ordered phase, it is expected that the spin-phonon coupling generates an additional contribution to the phonon frequencies.

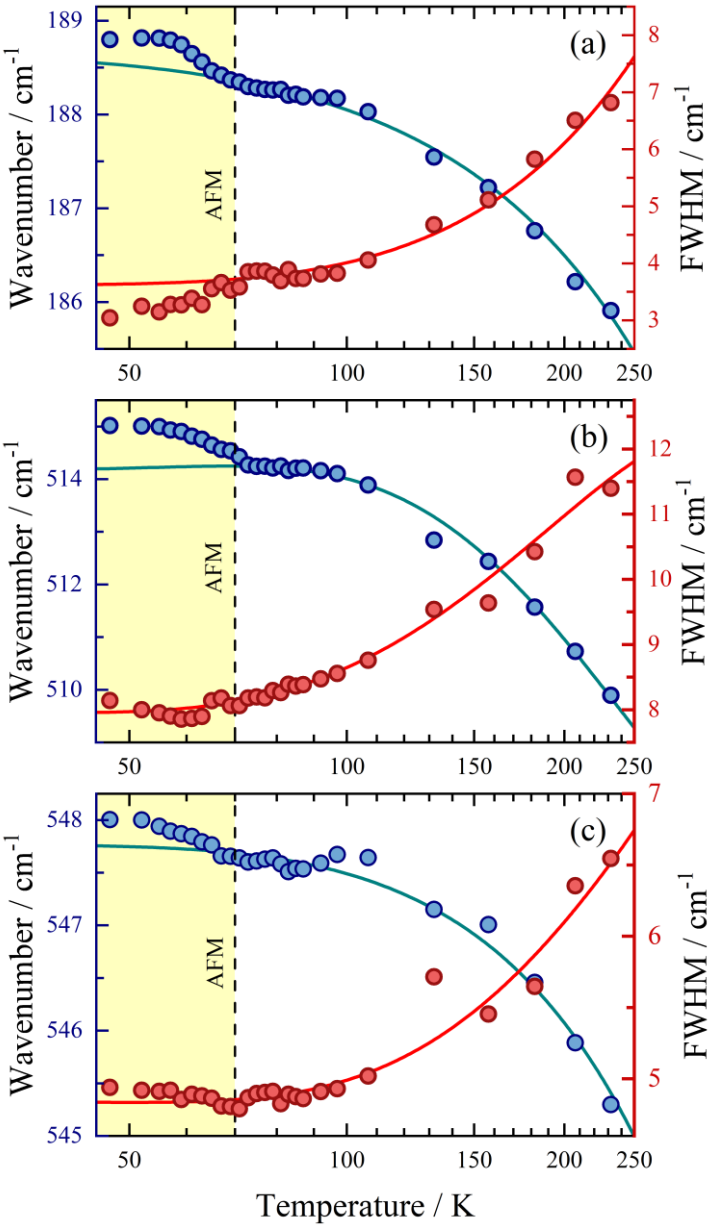

Figure 3.7. Temperature dependence of selected phonons frequencies and full width at half maximum of selected phonons of Cu_2OCl_2. The solid lines indicate the fit based on Balkanski's model.

Granado *et al*[27] have proposed a mechanism to describe the spin-phonon coupling by considering a molecular-field approximation and obtaining a phonon renormalization which scales with $\boldsymbol{M}^2$. As mentioned before, this model has been effective to describe the spin phonon coupling in several compounds and, in this context, the authors describe the phonon renormalization due to a spin-phonon coupling as equations (1.14) and (1.15).

However, in the case of incommensurate magnetic ordering, an extension of this model become necessary. This extension was reported by Kimura *et al*. [90] and consists of the inclusion of the nearest-neighbor (NN) and the next-nearest-neighbor (NNN) interactions. In this proposal, the phonon renormalizations process should be rewritten as (1.17).

Through powder neutron diffraction analysis, Zhao *et al*[73] showed that Cu_2OCl_2 magnetic ordered phase founded below 68 K can be described as an incommensurate antiferromagnetic phase which propagation vector is $\boldsymbol{k} = (k_x\ 0\ 0)$ with $k_x = 0.827(7)$. The magnetic moments are aligned with the Cu-O-Cu chains formed by OCu_4 tetrahedra along the $[\pm 1\ 0\ 1]$ directions[73]. Taking as reference the Cu ion placed at the lattice origin, two sets of two Cu ions could be considered as NN, because their bond distances are similar: the Cu ion located at $\pm\left(0\frac{1}{4}\frac{1}{4}\right)$ with Cu-Cu distance of 3.04 Å and Cu-O-Cu angle of $102.9\,°$ being assigned as D_1 interactions and the other Cu ion located at $\mp\left(\frac{1}{4}\ 0\ \frac{1}{4}\right)$ with Cu-Cu distance of 3.06 Å and Cu-O-Cu angle of 103.8° is associated to D_2 interactions. On the other hand, two Cu ions placed at $\pm\left(\frac{1}{4}\frac{1}{4}0\right)$ can be classified as NNN because of their Cu-Cu distances of 3.41 Å and Cu-O-Cu angle of $122.7\,°$, being assigned as D_3 interactions (Figure 3.4). Thus, the resulting phonon renormalization can be said as:

$$\Delta\omega = \frac{1}{m\omega}\left[D_1 + (D_2 + D_3)\cos\left(\frac{\pi k_x}{2}\right)\right] \tag{3.2}$$

where $D_j = \frac{\partial^2 J_j}{\partial u^2}$ $(j = 1, 2, 3)$.

According to the spin structure of Cu_2OCl_2, cations associated with D_1 and D_3 belong to two Cu-O-Cu chain with magnetic moments aligned along the [1 0 1] direction, whereas D_2 represents a chain running along $[\bar{1}\ 0\ 1]$, which includes the cation at the lattice origin (Figure 3.8). In this way, D_1 and D_2 have associated similar bridging

parameters, but, as they belong to different chains, they have opposite signs while D_3 is aligned with D_1. Notice that this arrangement could fulfill the condition $|D_1| \gg |D_2 + D_3|$ and, as discussed by Laverdière et al[49], the equation (3.2) reduces to equation **Erro! Fonte de referência não encontrada.**, as proposed by Granado *et al*[27].

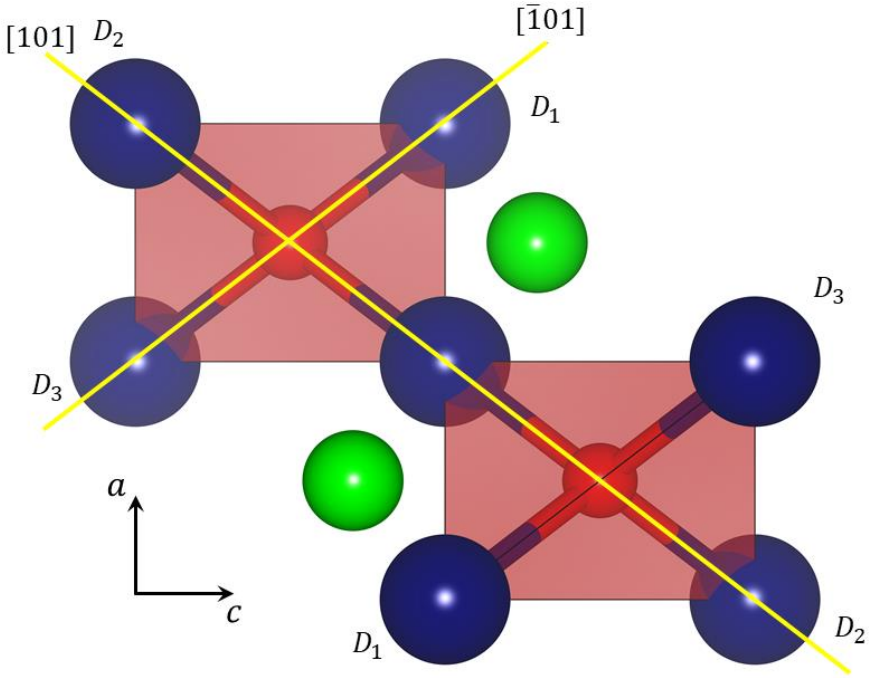

Figure 3.8. Basal view of CuO_4 tetrahedra showing the [101] and $[\bar{1}01]$ Cu chain planes and the NN and NNN Cu ions.

As mentioned before, it is important to remind that the magnetic temperature dependent profile of Cu_2OCl_2 show a broad maximum at approximately 140 K derived from the low dimensional chains of CuO_2Cl_2. In this way, the magnetization ($M_T(T)$) in such material can no longer be described exclusively as a consequence of the long range incommensurate AFM ordering, but as a combination of this long range ordering with the intra/interchain interactions, as follows:

$$M(T) = M_T(T) = (\chi_L + \chi_C) \cdot H \tag{3.3}$$

In this case, the χ_L factor represent the contribution of the long range ordered magnetic state (below T_N) and the χ_C factor is the contribution of CuO_2Cl_2 square chains to magnetic susceptibility. The $M_T(T)$ factor on the left side de of equation (3.3) represents the total magnetization, which takes in consideration both contributions obtained from magnetic measurements of Cu_2OCl_2. Once the magnetic data obtained here involves two different contributions, the equation **Erro! Fonte de referência não encontrada.** cannot be directly applied to analyze the renormalization process of phonons

observed in Cu_2OCl_2. Instead, keeping in mind the discussed models, could be more opportune to investigate the magnetization dependence of the phonon renormalization by plotting $(\Delta\omega)^{1/2}$ vs $M(T)$, where $M(T)$ is the magnetization data described by equation (3.3).

In Figure 3.9 (a-c) is shown $(\Delta\omega)^{1/2}$ as function of $M(T)$. From these analyses, it is clear the existence of a temperature range where the spin-phonon coupling renormalization scales with the magnetization, in good agreement with the model given by equation (3.5). However, it is important to note that this model is not valid in the full range where the multiferroic behavior is observed. Just below 70 K, the long range order does not seem to be the dominant contribution to the susceptibility and, although the phonon energy renormalization analysis, the proportionality between the phonon renormalization and the magnetization starts below 67 K. Another interesting feature is observed at low temperatures where a departure from the linear relationship can be noted below approximately 55 K (Figure 3.9). This effect is related to the upturn effect observed on the magnetic profile of Cu_2OCl_2 (Figure 3.3), which could be ascribed to magnetic impurities. Thus, the analysis of the spin-phonon results based on $(\Delta\omega)^{1/2}$ vs $M(T)$ plots describes the validity range of the proposed models for the phonon energy renormalization correction.

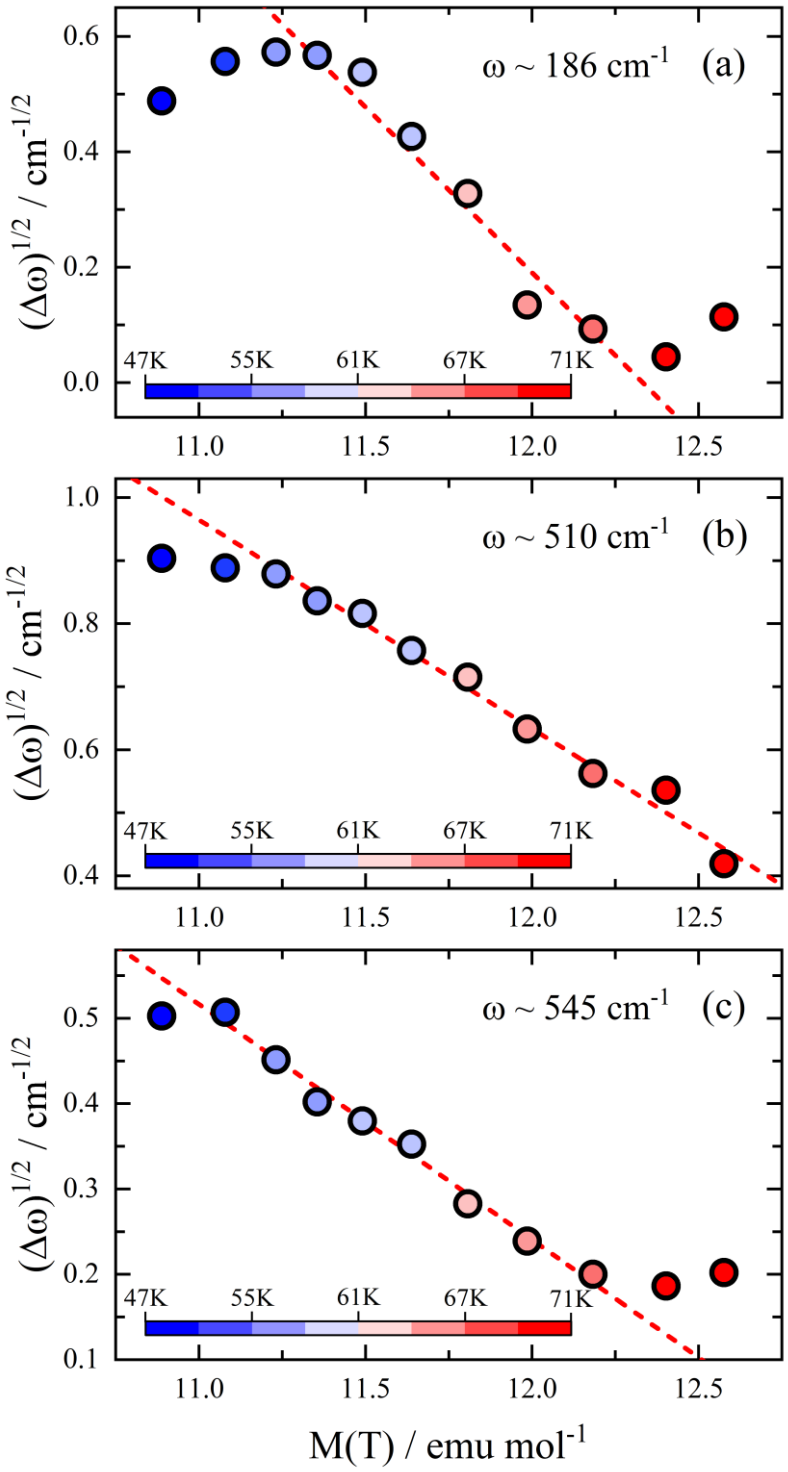

Figure 3.9. $(\Delta\omega)^{1/2}$ vs $M(T)$ plots for selected phonons of Cu_2OCl_2. The dashed lines are the linear fit of data.

3.3 *Cu_2OCl_2 Conclusions*

In this study, we synthesized the melanothallite Cu_2OCl_2 compound through the conventional solid-state reaction. Powder Diffraction and Magnetic susceptibility measurements were carried out to confirm the formation of the compound and the magnetic profile of polycrystalline Cu_2OCl_2. Once the structural and magnetic profile of synthesized samples were confirmed, Raman spectroscopy and Magnetic measurements of Cu_2OCl_2 also were analyzed to check the vibrational and magnetic profile of synthesized samples analyzing the influence of CuO impurity on Cu_2OCl_2 properties. Temperature-dependent Raman measurements were carried out to investigated the magnetoelectric coupling were a spin-phonon coupling was observed in melanothallite Cu_2OCl_2. The observed renormalization of phonons frequencies was measured being around 1 cm^{-1}. Characterized by a linear behavior between the frequencies deviations and the experimental magnetic data, the $\Delta\omega$ vs $(M(T)/M_0)^2$ revealed that the spin-phonon coupling starts at 68 K and, besides the incommensurate magnetic structure, the observed coupling behaviors are similar to those observed in stretching phonons of perovskites, whose renormalization follows the mean field behavior. The observed events also suggest that the renormalization due to the spin-phonon coupling depends only on the spin-phonon interactions and not on the phonon symmetry.

4. Temperature and pressure dependent investigations of $PbMn_7O_{12}$

Perovskites of $AA'_3B_4O_{12}$ type have been attracted attention due to their stronger charge, orbital and spins interactions of in their structures[91]. These compounds can present interesting physical and chemistry features as magnetoresistance at low fields, multiferroic properties and catalytic activities[92].

This perovskite family, usually called by quadruple perovskites, allows a big variation of chemical composition as A = Na^+, Cd^{2+}, Ca^{2+}, Sr^{2+}, Pb^{2+}, TR^{3+} (Rare Earths) or Bi^{3+}; A' = Cu^{2+}, Mn^{3+}, Co^{2+}, Pd^{2+}; B = $Mn^{3+/4+}$, Fe^{3+}, Cr^{3+}, Al^{3+}, Ti^{4+}, V^{4+}, Ge^{4+}, etc [91]. The ordering on the site A is reached in consequence of differences between the A and A' cations, where, in general, the A' is a transition metal which can adopt a square planar coordination.

In cases where A'= B = Mn, the family AMn_7O_{12} is formed containing Mn^{4+} ions and Jahn-Teller Mn^{3+} ions at different proportions depending on the cations oxidation states. The first elements of this family were discovered around 1970 by Marezio et al[93] and Bochu et al[94]. Nowadays, the AMn_7O_{12} perovskites were reported with A = Ca^{2+}, Bi^{2+}, Na^+, Ca^{2+}, Cd^{2+}, Pb^{2+}, Sr^{2+}, La^{3+} and Nd^{3+} from which only the $CaMn_7O_{12}$ [95], $BiMn_7O_{12}$ [96] and the recently discovered $PbMn_7O_{12}$ [97] present multiferroic properties.

$PbMn_7O_{12}$ (PMO) were recently synthetized by Locherer et al[98], where the authors report that this compound crystalize with $R\bar{3}$ space group at room temperature, similarly to $CdMn_7O_{12}$, $SrMn_7O_{12}$ and $CaMn_7O_{12}$. In addition, the authors report a structural transition to the $Im\bar{3}$ space group around 380 K and an antiferromagnetic ordering below 70 K. In this structure, the Pb^{2+} cation can induce polar distortions due to its lone pair electrons. In this way, the electrical and magnetic properties of PMO have been investigated intensively in the last years.

Recently, Belik et al[97] reported the structural, magnetic and electrical properties of PMO where, besides the confirmation of the structural transition associated to a charge ordering around 392 K, the authors report a second phase transition related to orbital ordering around 294 K. In the case of the magnetic properties, the authors studied the specific heat, dielectric constant and magnetic susceptibility as function of temperature. Their results revealed two magnetic transitions at 83 and 77 K, besides a third magnetic transition at lower temperatures, around 43 K. In addition, the electrical properties of PMO revealed that below 77 K the compound exhibit a spontaneous polarization of

$4\mu C/m^2$ and anomalies in dielectric constant as function of temperature and magnetic field. However, the authors did no exclude the existence of spontaneous polarizations below 83 K, explaining these effects could be too small to be detected between T_{N1} and T_{N2}. In this way, the PMO can be classified as a spin-driven multiferroic compound.

Once the coupling between the magnetic and electric orders in PMO is reported, Raman scattering spectroscopy can be used to study the temperature dependent behavior of PMO due to its sensibility to detect magnetic orderings through the coupling with the phonon lattice, mainly in perovskites compounds[99–102].

4.1 *$PbMn_7O_{12}$ synthesis procedure*

The PMO samples were synthesized through solid-state reaction under High-Pressure and High-Temperature (HPHT). This experiment was carried out in a Walker-type multianvil apparatus in the Center of Science at Extreme Conditions (CSEC) located at the School of Chemistry at The University of Edinburgh.

For this synthesis a stoichiometric amount of PbO (99.9%), MnO_2 (99.9%) and Mn_2O_3 (99.9%) were grounded until become a uniform powder and sealed into platinum capsules. The mixture was treated at different temperatures until reaching an optimized condition. In Figure 4.1 is showing the X-ray powder diffraction patterns recorded from as-synthesized $PbMn_7O_{12}$ samples of different attempts to synthesize the PMO perovskite adopting different conditions.

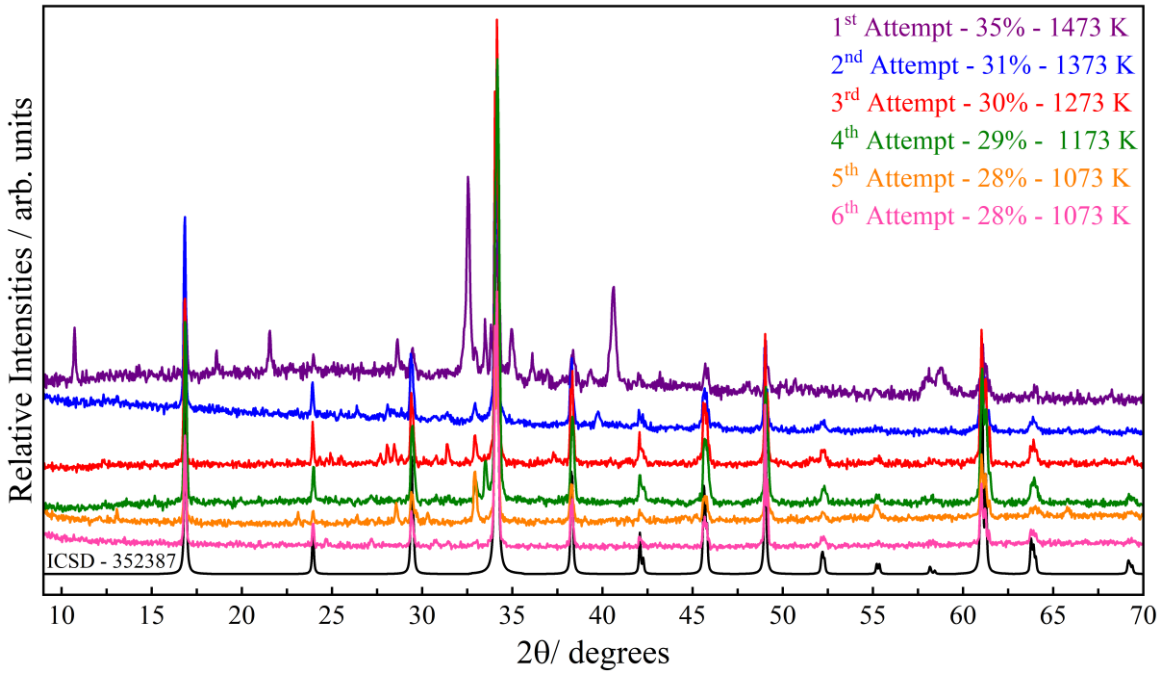

Figure 4.1. XRPD patterns of different as-synthesized $PbMn_7O_{12}$ samples with different synthesis conditions. The values on figure legend mean the potency percentage of the power unit and the equivalent temperature for each value. The black line on the bottom is the calculated XRPD pattern from the structure deposited on the ICSD database[103] with inscription number 352387.

In the first attempt, the values were chosen based on literature reports[97,103] where a stoichiometric amount of PbO (99.9%), Mn_2O_3 (99.9%) and MnO_2 (99.9%) were treated at 6 GPa and 1473 K during 60 minutes. At these conditions, the obtained samples seem to be melted, indicating that the sample reached its optimum point of reaction conditions, but expected a melting process due to the remain heating process. From this

point, the set-pointed temperature of synthesis proceedings was decreased in order to optimize the $PbMn_7O_{12}$ as the main phase of synthesized samples.

The best conditions were found on the 5th attempt, where the precursors were treated at 6 Gpa and 1073 K during 60 minutes. However, the Rietveld analyzes of as-synthesized samples revealed a considerable amount of Mn_2O_3 (9% of weight fraction) and Mn_3O_4 (6% of weight fraction) compounds as secondary phase from the synthesis procedure (evidenced by unexpected diffraction peaks between 28º and 34º in Figure 4.1). These impurities are given by the high volatility of PbO at high temperatures and a new attempt was carried out in order to decrease these amount of impurities. The presence of secondary phases was corrected by the addition of a PbO excess in proportion to the secondary phases to the precursors obtained in the as-synthesized sample.

The last attempt of $PbMn_7O_{12}$ was carried out at 6 GPa and 1073 K during 60 minutes. After treatment, the system was quenched and the pressure was slowly released until ambient pressure. The as-synthesized sample presented a reasonable proportion between the main phase and the impurities related to synthesis procedure as will be discussed later.

4.2 *Results and discussion*

The Synchrotron X-ray Powder Diffraction (XPRD) pattern of synthesized PMO samples are showed in Figure 4.2. These results are indicating that the samples presented the rhombohedral phase whose lattice parameters are $a = 10.523(5)$ Å, $b = 10.523(5)$ Å, $c = 6.411(1)$Å and $\gamma = 120°$. Those lattice parameters are very close to those reported by Belik *et al*[103] confirming the formation of the proposed sample. The PMO structure can be said as a perovskite in which the manganese ion occupy the A' and B positions in $(AA'_3)B_4O_{12}$, presenting square planar and octahedral coordination with the oxygen ions, while the Pb ions are located between these octahedra (Figure 4.3).

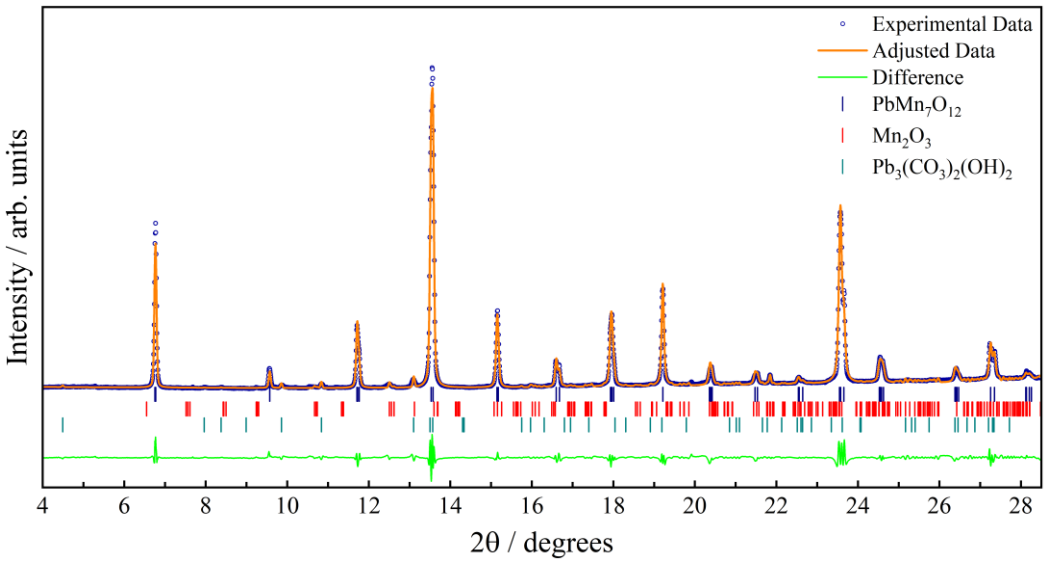

Figure 4.2. The diffraction pattern of $PbMn_7O_{12}$ (PMO) obtained through Synchrotron X-ray Powder Diffraction (SXRPD). The dark blue bars indicate the calculated diffraction peaks positions of rhombohedral phase of PMO reported by reference [103] (ICSD number 252387), the red bars are those expected for Mn2O3 and the cyan bars are expected for $Pb_3(CO_3)_2(OH)_2$

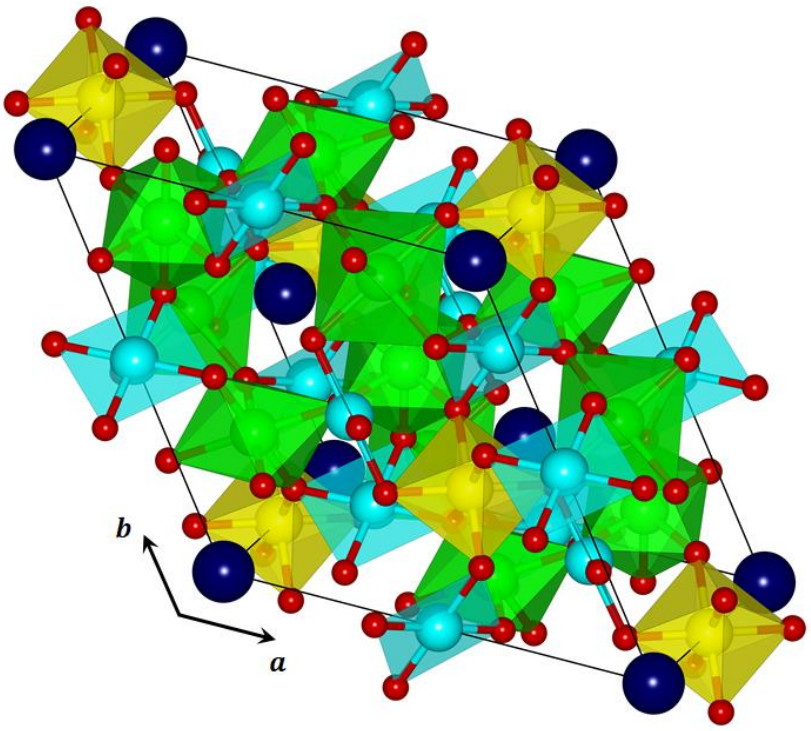

Figure 4.3. The unit cell of rhombohedral $PbMn_7O_{12}$. The dark blue spheres are the Pb ions and the red spheres are the oxygen ions. The cyan and green blue spheres are the Mn^{3+} ions with square planar and octahedral coordination, respectively, while the yellow ones are Mn^{4+} octahedrally coordinated.

Once the formation of rhombohedral PMO was confirmed, the magnetic behavior of synthesized samples was analyzed in order to verify the reported magnetic transitions

through temperature dependent magnetic susceptibility measurements and field dependent magnetization behavior. These results are shown in Figure 4.4.

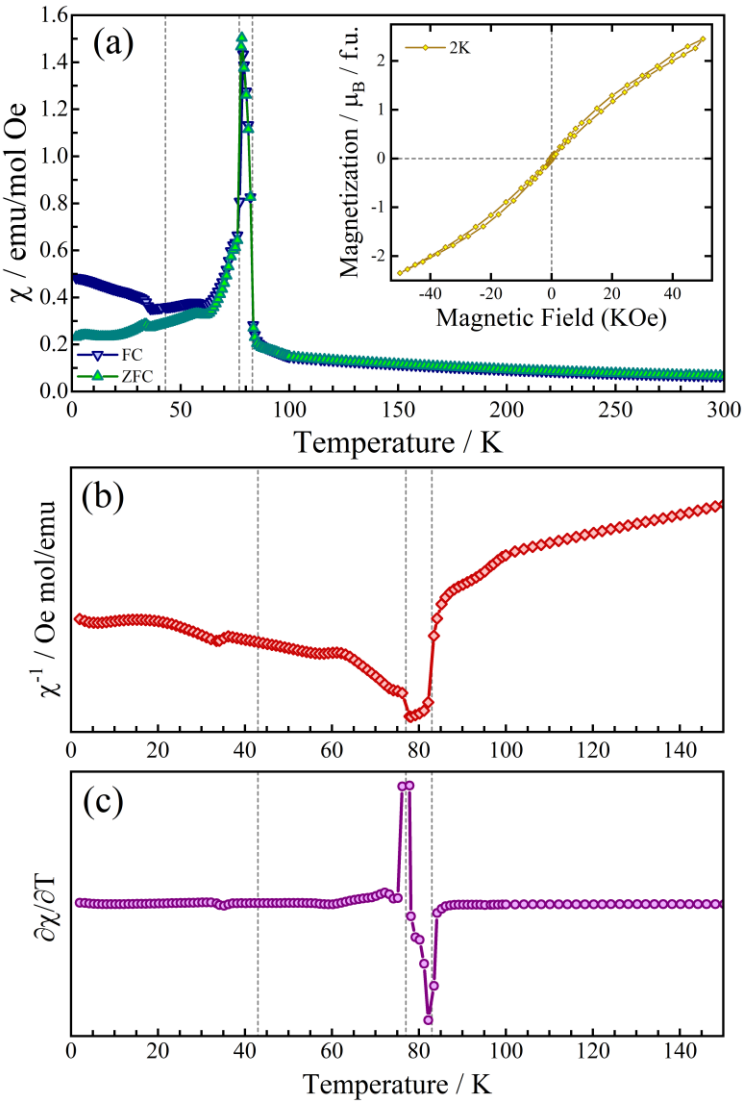

Figure 4.4. The magnetic behavior of synthesized PMO samples. (a) The ZFC and FC magnetic susceptibility as function of temperature, the inset shows the magnetic moment as function of magnetic field. (b) The inverse of magnetic susceptibility. (c) first derivate of of magnetic susceptibility as function of temperature. In all figures the gray dashed lines show the magnetic events reported in literature[97].

The temperature dependent magnetic susceptibilities (Figure 4.4(a)) present three sequential events below 90 K, they are: an abrupt increase around 83 K, followed by an abrupt decrease around 77 K and a slight magnetic event around 38 K. The first two events are clear in the inverse of magnetic susceptibility (χ^{-1}) (Figure 4.4(b)) and from its first derivate ($\partial\chi/\partial T$) (Figure 4.4(c)) and these analyzes corroborate to infer that the slight third event is started around 38 K.

From these analyzes, it is clear that the synthesized PMO samples present two magnetic transitions around 83 and 77 K, associated to T_{N1} and T_{N2} magnetic transitions of PMO, and a slight magnetic event around 38 K, associated to T_{N3}. These observations are in good agreement with the magnetic transitions reported for PMO by other authors[97]. However, the small magnetic event observed at 38 K (associated to T_{N3}) was found at temperatures slight lower than those reported in literature, where it was reported at 43 K. In addition, the field dependent magnetization analysis (inset of Figure 4.4(a)) also is in good agreement with those reported by Belik *et al*[97]. Thus, we can conclude that the synthesized sample are well ordered in agreement with those results presented in literature and the synthesized samples are well magnetically ordered.

Once the magnetic behavior of PMO was verified, Raman spectroscopy measurements were carried out in order to evaluate possible couplings between the magnetic ordering and the phonons lattice. For this study the Raman spectrum of PMO was investigated in the temperature range from 300 K until 10 K.

Based on the group theory analysis, the distribution of the C_{3i}^2 group factor at the Γ point of Brillouin zone is $6A_g \oplus 6E_g$ Raman active-modes[83] (see Table 2). Based on this analysis 18 modes of mixed symmetries are predicted in the Raman spectra of the polycrystalline PMO sample at $R\bar{3}$ space group.

Table 2. Irreducible representation of vibrational modes for $PbMn_7O_{12}$.

Ions	Site	Symmetry	Contribution
Pb	$3a$	S_6	$A_u \oplus E_u$
Mn_1	$9e$	C_i	$3A_u \oplus 3E_u$
Mn_2	$9d$	C_i	$3A_u \oplus 3E_u$
Mn_3	$3b$	S_6	$A_u \oplus E_u$
O_1	$18f$	C_1	$3A_g \oplus 3A_u \oplus 3E_g \oplus 3E_u$
O_2	$18f$	C_1	$3A_g \oplus 3A_u \oplus 3E_g \oplus 3E_u$
			$\Gamma_{TOT}: 6A_g \oplus 14A_u \oplus 6E_g \oplus 14E_u$
			$\Gamma_{AC}: A_u \oplus E_u$
			$\Gamma_{IR}: 13A_u \oplus 13E_u$
			$\Gamma_{Ram}: 6A_g \oplus 6E_g$

The Raman spectra obtained for the polycrystalline sample of PMO were weaker in comparison to those obtained for other compounds reported in this work. The best Raman spectrum obtained for PMO at 10 K Figure 4.5) allows the identification of 6

vibrational modes of mixed symmetries in the range between 100 and 750 cm^{-1}, being the most intense one located around 660 cm^{-1}.

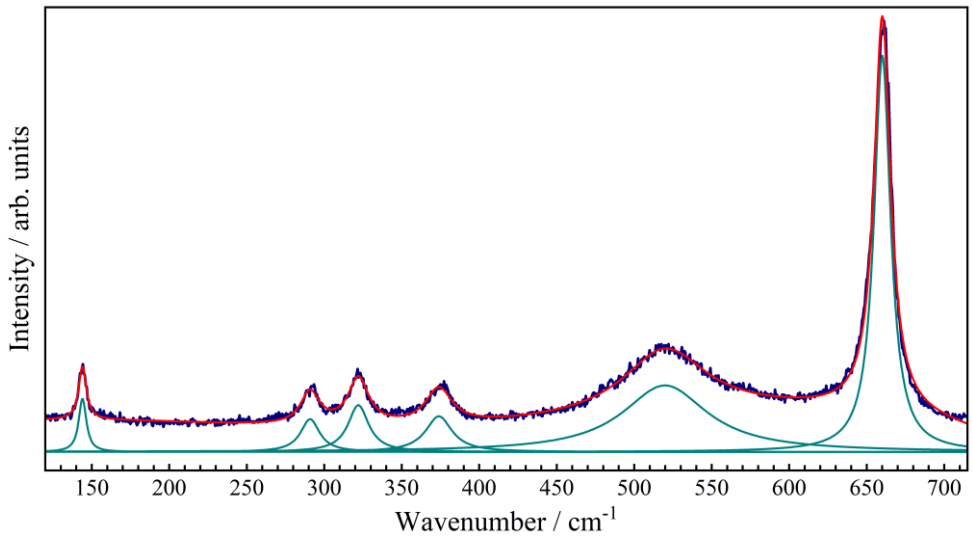

Figure 4.5. Raman spectra of $PbMn_7O_{12}$ obtained at 10 K.

The temperature-dependent Raman spectra recorded for polycrystalline sample of PMO is showed in Figure 4.6. Under cooling process, the PMO Raman spectra did not present any remarkable change in terms of additional or suppressed bands. Only the usual high-frequency shift and the sharpening of vibrational modes were detected under temperature decrease. As consequence, the overall signature of Raman spectra is maintained along the investigated temperature range, which imply that the rhombohedral PMO phase did not undergoes any phase transition in the investigated temperature range.

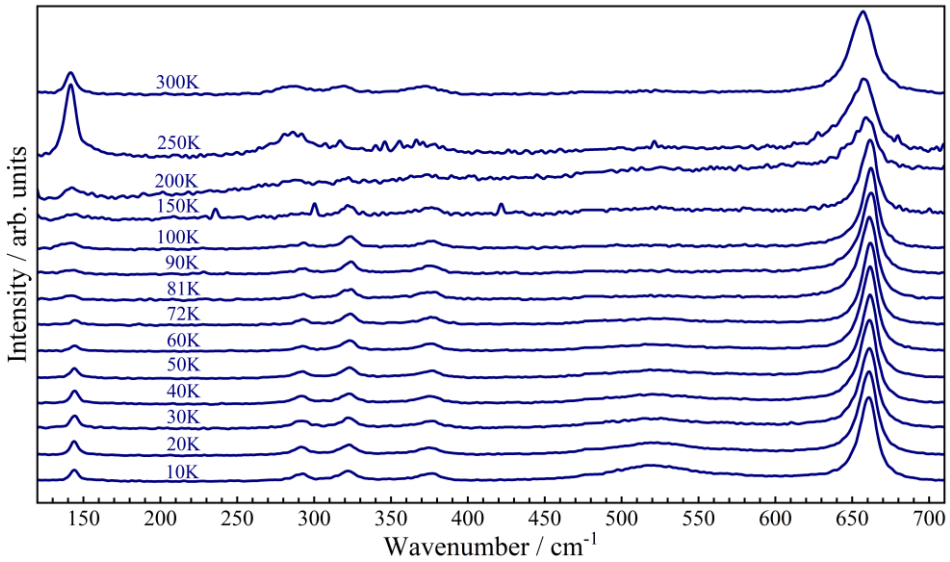

Figure 4.6. Temperature-dependent Raman spectra of pollyristaline pellet of PMO.

The temperature dependent Raman spectrum were deconvoluted into lorentizian functions in order to obtain more acurate information about the temperature dependent phonons features. The analyzes for some selected phonons frequencies are shown in Figure 4.7. From these results is notable that all selected phonon seems to expect renormalization process of their frequencies at the temperatures of the magnetic orderings, characterized by changes in the temperature-depence of the phonons positions. This behavior is more clear below 40 K, temperature at which is observed the T_{N3} of PMO, indicating a possbile existence of a coupling effect between the magnetic moments and the phonons.

However, the very weak character of PMO Raman spectrum, even at the lowest recorded temperature (Figure 4.5), had an important impact in this temperature dependent Raman study. This fact is reflectd in the deconvolution treatment, where all selected phonons modes presented a high dispersion in the frequency positions, mainly at high temperatures. These features make difficult the treatment of the anharmonicity of frequencies as proposed by Balkanski[26], hindering a more accurate analysis about possible renormalization effects.

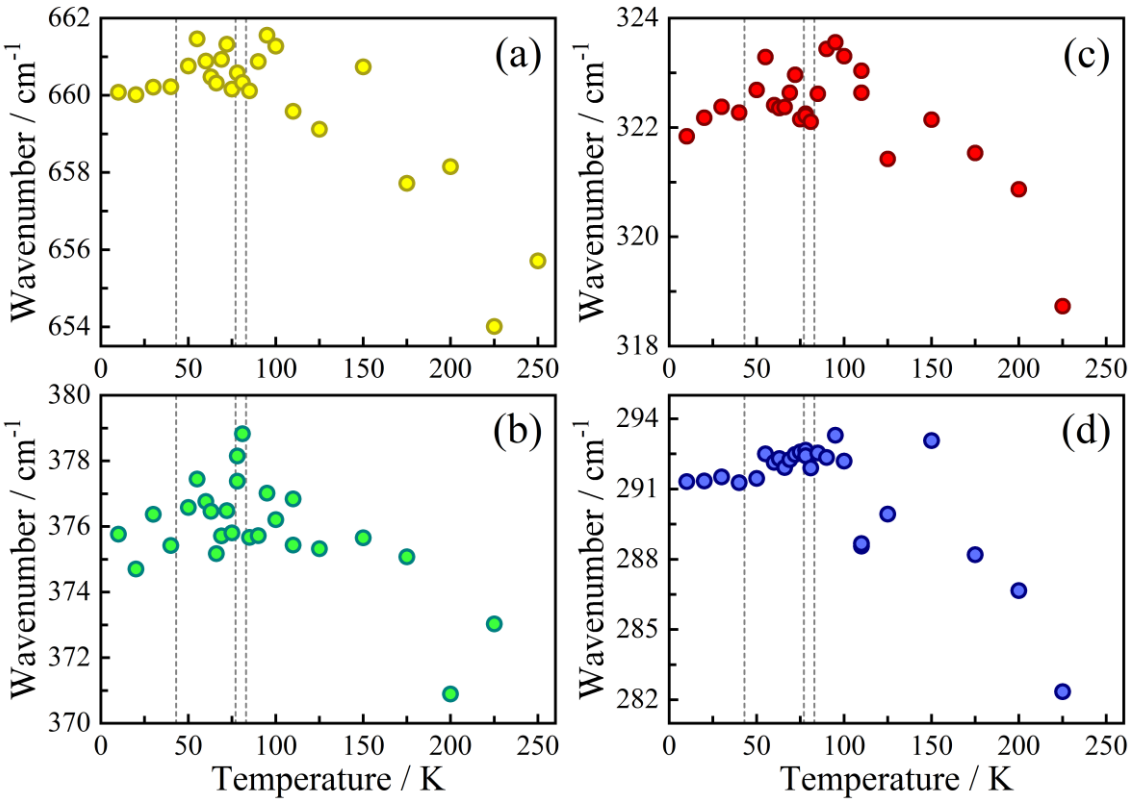

Figure 4.7. Temperature dependent frequencies of selected PMO phonons.

The PMO samples were also submitted to High-Pressure Synchrotron x-ray powder diffraction (SXRPD) analysis. In Figure 4.8 are shown the SXRPD patterns from ambient pressure until 21.90 GPa. For these analyzes the samples were grounded and sealed into a gas-membrane DAC with Argon as hydrostatic medium.

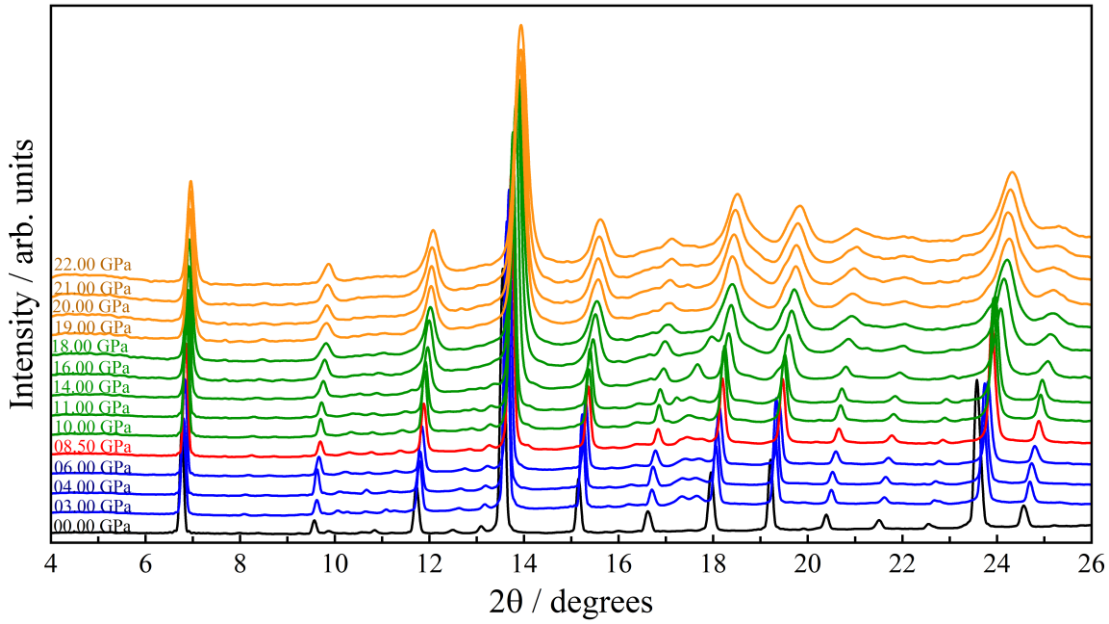

Figure 4.8. Pressure-dependent Synchrotron X-ray Powder Diffraction (SXRPD) Pattern of PMO.

As mentioned before, at ambient pressure the PMO samples adopt a rhombohedral ($R\bar{3}$) configuration and both SXRPD and XRPD analyzes revealed the presence of small amounts of Mn_2O_3 (3%) and $Pb_3(CO_3)_2(OH)_2$ (2%) as secondary phases (Figure 4.1 andFigure 4.2) and the pressure-dependent diffraction patterns (Figure 4.8) showed that these impurity signatures can be observed up to 14 GPa.

Regarding to the rhombohedral PMO diffractions peaks, the initial analysis indicates that the rhombohedral phase remains unchanged until 8.5 GPa, where very slight changes were noted. At this pressure value, the pair of diffraction peaks located at 16.7º become one and, in the following pressure point, a new diffraction peak is observed at 17º. This new peak presented a shift as pressure increases until join to the peak located at 18º around 18 GPa. These changes are shown in terms of position and intensity of the diffraction peaks in Figure 4.9 (a) and (b). In addition, the rising of small diffraction peaks also could be observed at 19º and 21º around the pressure of 14 GPa, which can also be indication of another structural change. These small changes in pressure dependent diffraction pattern could be understood as indications of changes in the crystalline structure of PMO.

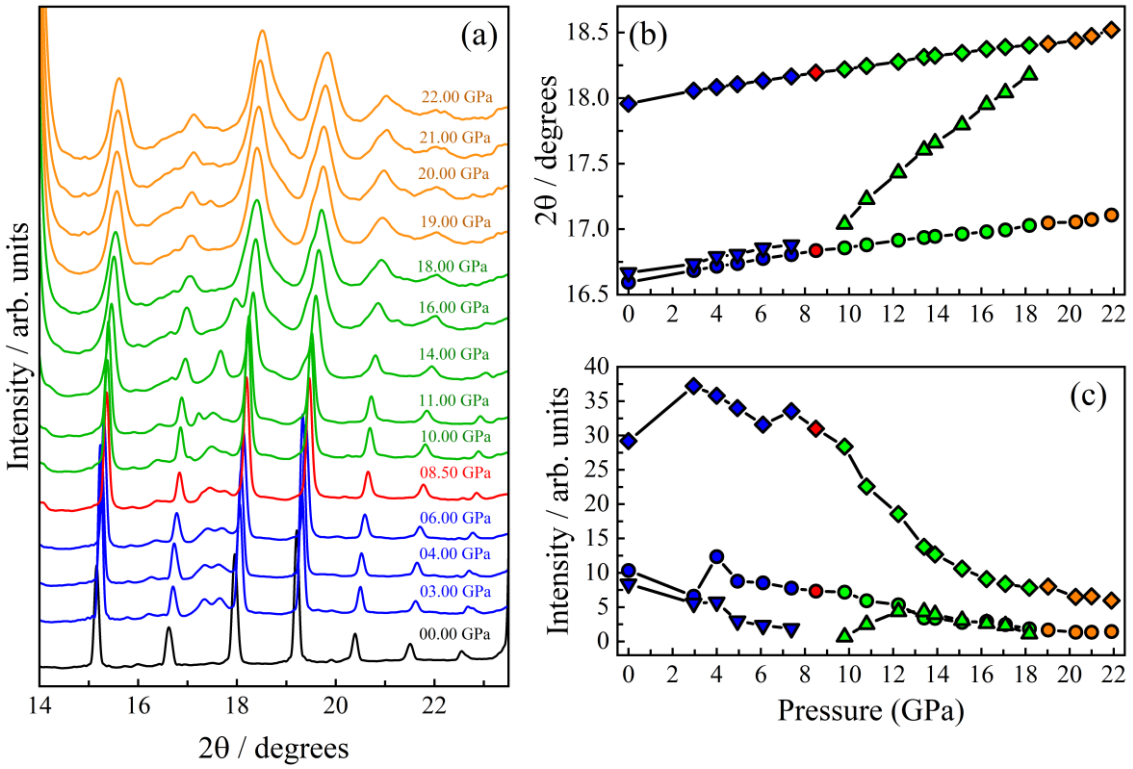

Figure 4.9. Initial analysis of slight changes observed in the pressure dependent SXRPD pattern.

4.3 *$PbMn_7O_{12}$ Conclusions*

The perovskite $PbMn7O_{12}$ (PMO) samples were synthesized although solid state reaction under HPHT conditions. XRPD and SXRPD analyses were carried out to confirm the formation of rhombohedral PMO sample and check the amount of impurities originated from the synthesis method adopted. After confirm the compound formation, the magnetic behavior of PMO sample was analyzed in order to verify its magnetic behavior. The results confirm two magnetic transitions around 83 K and 77 K, associated to T_{N1} and T_{N2} transitions of PMO, and the third magnetic transition observed around 38 K was detected slight lower than the T_{N3} transition reported at 43 K in literature.

The temperature dependent Raman measurements below room temperature were carried out in order to investigate possible coupling between the spin moments and the lattice phonons in PMO samples. From these analyses it was observed a hardening effect in some selected phonon modes below 44 K, which could be an indicative of a coupling effect. However, the low quality of Raman spectra induces a high dispersion on phonons positions, mainly at higher temperatures, making difficult to proceeds a precise study of temperature dependent phonons frequency. These features highlight the necessity to repeat these experiments in order to obtain data with better quality to perform a precise study of temperature dependent phonons features.

In addition, the pressure dependent behavior of PMO structure were investigated through SXRPD from ambient pressure up to 22 GPa. Analyses on pressure dependence of diffraction patterns indicate slight changes on diffraction peaks at 8.5, 14 and 19 GPa which could be indicatives of structural changes. However, these are initially results and deeper investigations through Le Bail or Rietveld refinements are needed to clarify the existence of such structural changes in this pressure range.

5. The Spin-phonon coupling in $TmMnO_3$

In the past years, the family of orthorhombic manganite perovskites $RMnO_3$ (o-RMO) became extensively studied because of their interesting properties as charge ordering, magnetoresistance and multiferroicity.[70,71,104–106] At ambient pressure, the $RMnO_3$ family crystallize in an orthorhombic perovskite structure for large R^{3+} ionic radius (r_R) presenting an A-type antiferromagnetic (AFM) phase[90,105]. On the other hand, for smaller r_R, the orthorhombic structure is replaced by an hexagonal phase[107–109] and its magnetic structure migrates to an incommensurate or E-type AFM structure[90,105]. The orthorhombic perovskite phase can also be stabilized in compounds with small r_R by means of High-Pressure and High-Temperature (HP/HT) treatments[110].

Belonging to the group of the smallest r_R, $TmMnO_3$ (TMO) crystallizes in a hexagonal structure presenting a $P6_3cm$ spatial group. This structure can be described as constituted by bipyramids of MnO_5 with oxygen atoms locate at the interstice of those bipyramids.[110]

Wang et al[111] studied the ferroelectric behavior of hexagonal $TmMnO_3$ (*h*-TMO) reporting a ferro-paraelectric phase transition around 621 K, while Yen et al[112] reported a magnetic transition around 84 K. Latter, Massa et al[113] confirmed the electric and magnetic transitions showing a ferroelectric-magnetic coupling in the magnetically ordered phase by means of far-infrared emissivity and reflectivity spectra analysis.

The orthorhombic phase of $TmMnO_3$ (*o*-TMO), stabilized through an HP/HT treatment, belong to the P*bnm* space group and its structure can be described as a distorted perovskite structure with corner-sharing MnO_6 octahedra distorted chain running along the *c* axis and Tm ions located at the free space between these octahedra. By means of specific heat analysis, Tachibana et al[114] reported a magnetic transition on *o*-TMO around 43 K. Later, Pomjakushin[115] classified the magnetic structure of *o*-TMO as incommensurate below 43 K and reported one more magnetic transition at 32 K, where the incommensurate structure become E-type AFM. In the same study, the authors reported dielectric susceptibilities and pyroelectric measurements where a spontaneous electric polarization appear below 32 K, which is originated by the lattice distortions due to the E-type AFM phase. These features evidence a multiferroic phase on *o*-TMO for bulk and powder samples. The ferroelectric phase below 32 K also was confirmed by

Salama et al[109] by means of Mössbauer spectroscopy, while Han et al[116] observed this phase transition in thin films. Recently, these observations also were confirmed through resonant x-ray analysis in bulk samples by Garganourakis *et al*.[117] and in thin films by Windsor *et al*.[118]

Recently, Shimamoto et al[119] reported the room temperature Raman spectra of the orthorhombic $RMnO_3$ (R = Gd - Lu) family (*o*-RMO) obtained as thin films in a $YAlO_3$ substrate. In this study, it was observed the influence of chemical pressure along *b*-axis showing that the change of the R ion induces a shift of the oxygen atoms on the *ca* plane. Furthermore, the study reports the Raman spectrum of *o*-TMO in film thin, but no information about bulk *o*-TMO was presented.

The spin-phonon coupling in *o*-RMO family was reported by Granado et al[27] and Laverdiere et al[49], where they affirm the spin-phonon coupling in compounds with small r_R and incommensurate AFM can be negligible for some compounds. In addition, the authors conclude that the spin-phonon coupling is negligible in compounds with small r_R and incommensurate AFM orderings, whereas in case of an E-type AFM ordered compounds, the authors affirm that the spin-phonon coupling should be very weak or absent. In the case of the E-type $HoMnO_3$, the authors did not observed any anomaly on temperature dependent phonon behavior indicating that its magnetic exchanges are self-excluding.[49]

In the case of TMO, the spin-phonon coupling was confirmed in *h*-TMO by far-infrared spectroscopy considering the *h*-RMO family[120]. In this study, the authors observed a phonon renormalization occurring at the magnetically ordered phase characterizing a spin-phonon coupling effect. The phonons renormalizations were estimated to be around 5 cm^{-1} for *h*-TMO.

The observed coupling between electric and magnetic ordering suggests that the magnetic ordering can also couple with the phonons in case of *o*-TMO. Thus, the Raman scattering spectroscopy is a powerful technique to confirm this coupling effect due to its sensibility to detect magnetic orderings through the coupling with the phonon lattice, mainly in perovskites compounds.[99–101] Thus, the temperature dependence of the Raman-active phonons below room temperature can help to elucidate *o*-TMO magnetic and electric behavior and their couplings.

5.1 *$TmMnO_3$ Synthesis procedure*

The o-TMO polycrystalline samples were obtained although HPHT treatment of *h*-TMO. The *h*-TMO polycrystalline samples were synthesized by solid-state reaction, where stoichiometric amounts of Tm_2O_3 (REacton, 99.99%) and Mn_2O_3 (Aldrich, 99.99%) were grounded together in an Agatha mortar. The mixture was pressurized into pellets and calcined in a conventional oven at 1200 °C during 24 hours. In sequence, the h-TMO pellets were grounded and sealed into platinum capsules in order to be treated at 1573 K under 6 GPa during 60 min in a Walker type multianvil press of Centre of Science at Extreme Conditions (CSEC), located at School of Chemistry of University of Edinburgh. After the reaction, the system was quenched to room temperature (RT) and the pressure was slowly released until atmospheric pressure. The resultant dark-green polycrystalline dense pellets were grounded until becoming powder and characterized by x-ray diffraction (XRD) on a BRUKER D8 diffractometer (Cu $K_{\alpha 1}$ radiation 1.5406 Å) in order to confirm the stabilization of the orthorhombic phase.

5.2 *Results and Discussions*

The *h*-$TmMnO_3$ samples obtained from the solid-state reaction in air presented the $P6_3cm$ space group confirmed by means of x-ray powder diffraction pattern analysis (Figure 5.2). The obtained lattice parameters $a = 6.086(0)$ Å and $c = 11.372(8)$ Å, in good accordance with those reported by Uusi-Esko *et al*.[110] In Figure 5.1 is shown the unit cell of h-TMO where the bipyramids of MnO_5 are illustrated in blue color with the red oxygen ions at the apical positions, while the interstitial Tm ions are presented in purple color (left side of Figure 5.1).

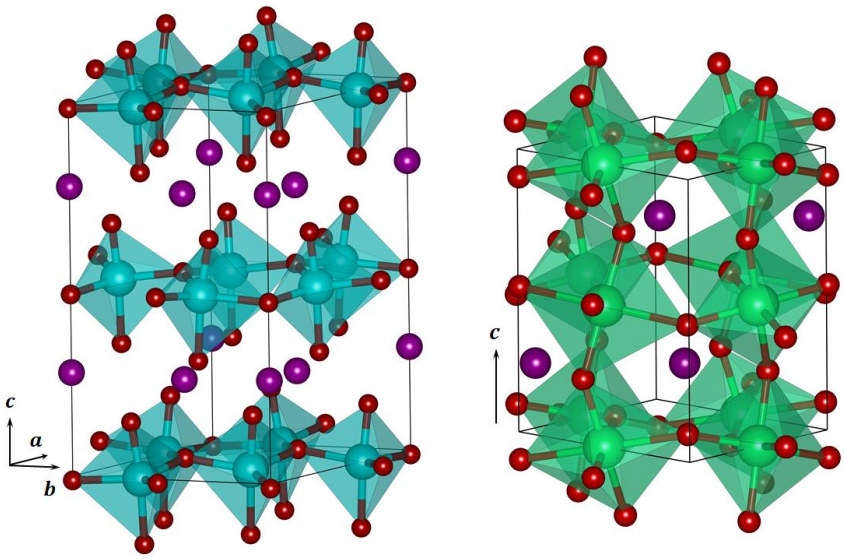

Figure 5.1. The unit cell of h-TMO (Left side) and *o*-TMO (Right side) reported by reported by Uusi Esko *et al.*[110] (ICSD number 162209 and 162209, respectively). In both structures, the dark red spheres are the O^{2-} ions and the purple are the Tm^{2+} ions, while the blue and green spheres represent the Mn^{3+} ions in the hexagonal and orthorombic structures, respectively.

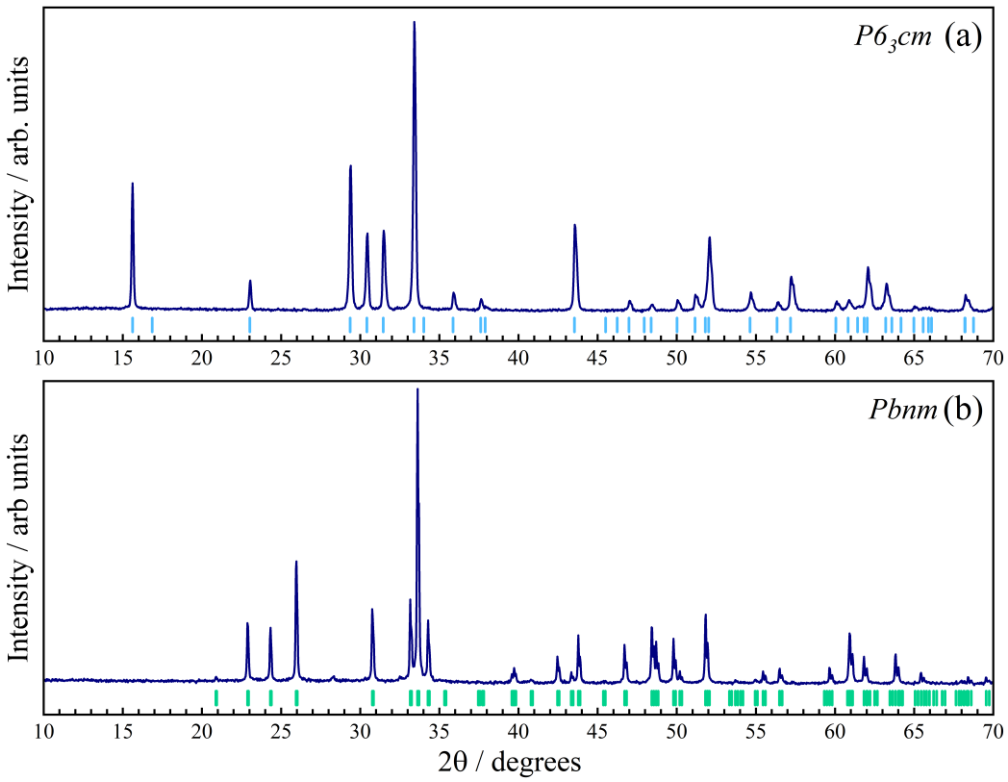

Figure 5.2. (a) Powder XRD analysis of *h*-TMO sample. The cyan bars indicate the reflection positions of h-TMO calculated based on structure reported by reference [110] (ICSD number 162202). (b) Powder XRD analysis of the *o*-TMO sample. The green bars indicate the reflection positions of *o*-TMO calculated based on structure reported by reference[110] (ICSD number 162209).

Through HPHT treatment, the crystal structure of the hexagonal phase was changed to orthorhombic structure belonging to a *Pbnm* space group which also was confirmed by means of powder x-ray analysis (Figure 5.2 (b)). The obtained lattice parameters were *a*: 5.232 Å, *b:* 5.814 Å and *c*: 7.324 Å with 4 molecules per unit cell in good agreement with other orthorhombic $TmMnO_3$ compounds reported on literature[110]. This phase is recognized as an orthorhombically distorted-perovskite structure where the Mn^{3+} ions are coordinated octahedrally with six oxygen ions forming a distorted corner-sharing MnO_6 octahedra chains, while the Tm ions are located at the free space between those octahedrons (right side of Figure 5.1 (b)).

After confirming the orthorhombic phase of $TmMnO_3$, the samples treated through HPHT were submitted to magnetic analysis. The magnetic profile of o-TMO samples was investigated in the temperature range between 300 and 2 K analyzing the magnetic susceptibility and the magnetization hysteresis was recorded at 2 K.

The temperature dependent magnetic susceptibility of o-TMO is shown in Figure 5.3 (a). The overall signature of magnetic susceptibility obtained here is in good accordance with those reported in the literature [109,110,115]. The determination of temperature magnetic ordering for this compound through the magnetic susceptibility is given by a very slight deviation of the first derivate of magnetic susceptibility behavior as function of temperature ($\partial\chi/\partial T$). Although the magnetic behavior observed here is similar to those reported in literature, the $\partial\chi/\partial T$ did not presented any considerable deviation in the temperature range where the magnetic events should be present and only a small deviation is observed around 27 K. As the magnetic events are better defined in literature by means of the lambda (λ) behavior observed in temperature dependent specific heat analysis[109] or through resonant x-ray analysis[117,118], the absence of a small event like this did not exclude the magnetic behavior of the samples synthetized here. The absence of this event is probably related to the high value of magnetic field adopted for these measurements and, once no magnetic event is reported below 30 K for the *o*-TMO compound, the small oscillation around 27 K also should be related to experimental artifacts.

The magnetization signal as function of the magnetic field measured at 2 K is shown in Figure 5.3 (b). This result is showing a hysteresis loop with two very slight saturated magnetization points and two states of spontaneous magnetization almost null (inset of Figure 5.3(b)). This result also in good accordance with those hysteresis loop reported by Yoshii *et al*[121]. As observed for the temperature dependent magnetic

susceptibility, the overall signature and the very sharp character of magnetic hysteresis loop obtained here corroborates with an antiferromagnetically ordered material. Besides the absence of remarkable changes on χ and $\partial\chi/\partial T$ that make evident a magnetic transition in o-TMO, the hysteresis loop is an indicative that the synthetized samples present an AFM ordered character, at least, at 2K.

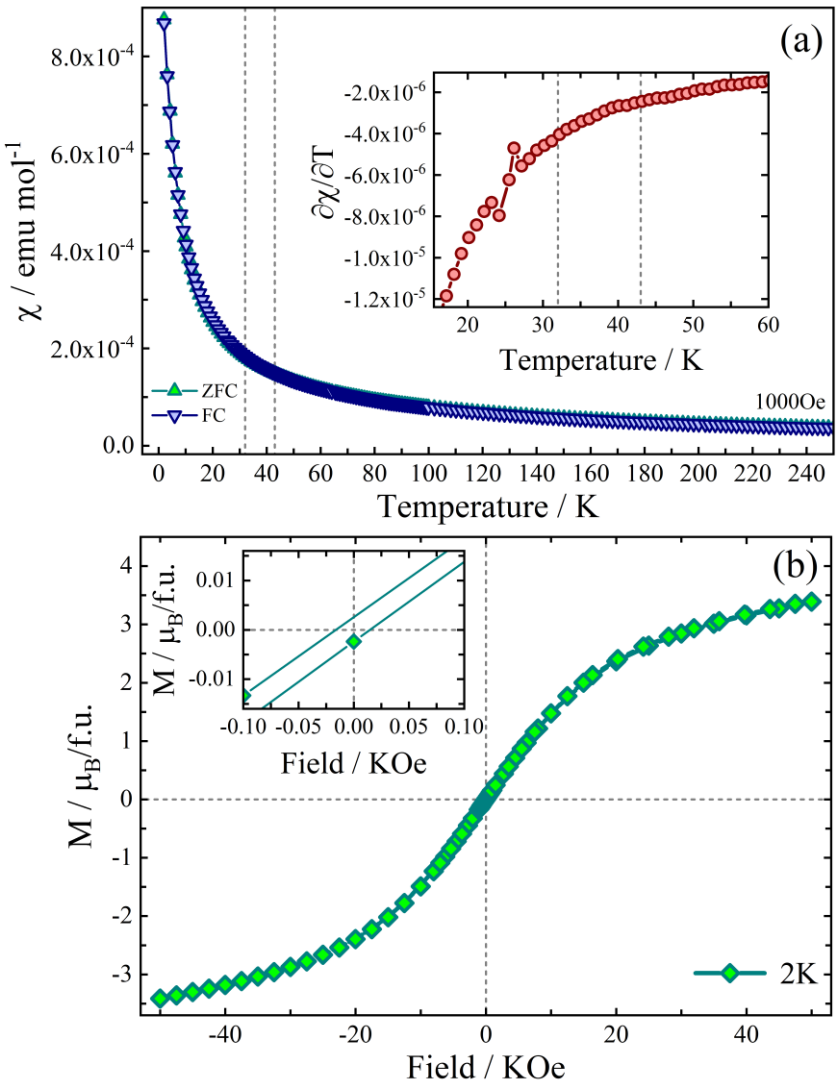

Figure 5.3. The Magnetic properties of o-TMO. (a) The Magnetic Susceptibility and the 1st derivate of magnetic susceptibility of o-TMO. (b) Magnetic Hysteresis Loop measured at 2K.

The room temperature Raman spectrum of *o*-TMO is shown in Figure 5.4. Based on the group theory analysis, the distribution of the D_{2h} group factor at the Γ point of Brillouin zone is $7A_g \oplus 5B_{1g} \oplus 7B_{2g} \oplus 5B_{3g}$ Raman active-modes[83] (see Table 3). Based on this analysis 24 modes of mixed symmetries are predicted in the Raman spectra of the orthorhombic $TmMnO_3$ polycrystalline sample at room temperature. The Raman

spectrum analysis obtained here allows the identification of 13 vibrational modes, being the most intense one located around 620 cm^{-1}.

Table 3. Irreducible representation of vibrational modes for *Pnma* $TmMnO_3$.

Ion	Site	Symmetry	Contribution
Tm	$4c$	C_S^{xz}	$2A_g \oplus A_u \oplus B_{1g} \oplus 2B_{1u} \oplus 2B_{2g} \oplus B_{2u} \oplus B_{3g} \oplus 2B_{3u}$
Mn	$4b$	C_i	$3A_u \oplus 3B_{1u} \oplus 3B_{2u} \oplus 3B_{3u}$
O	$4c$	C_S^{xz}	$2A_g \oplus A_u \oplus B_{1g} \oplus 2B_{1u} \oplus 2B_{2g} \oplus B_{2u} \oplus B_{3g} \oplus 2B_{3u}$
O	$8d$	C_1	$3A_g \oplus 3A_u \oplus 3B_{1g} \oplus 3B_{1u} \oplus 3B_{2g} \oplus 3B_{2u} \oplus 3B_{3g} \oplus 3B_{3u}$
			$\Gamma_{TOT}: 7A_g \oplus 8A_u \oplus 5B_{1g} \oplus 10B_{1u} \oplus 7B_{2g} \oplus 8B_{2u} \oplus 5B_{3g} \oplus 10B_{3u}$
			$\Gamma_{AC}: B_{1u} \oplus B_{2u} \oplus B_{3u}$
			$\Gamma_{IR}: 9B_{1u} \oplus 7B_{2u} \oplus 9B_{3u}$
			$\Gamma_{RAM}: 7A_g \oplus 5B_{1g} \oplus 7B_{2g} \oplus 5B_{3g}$
			$\Gamma_{silent}: 8A_u$

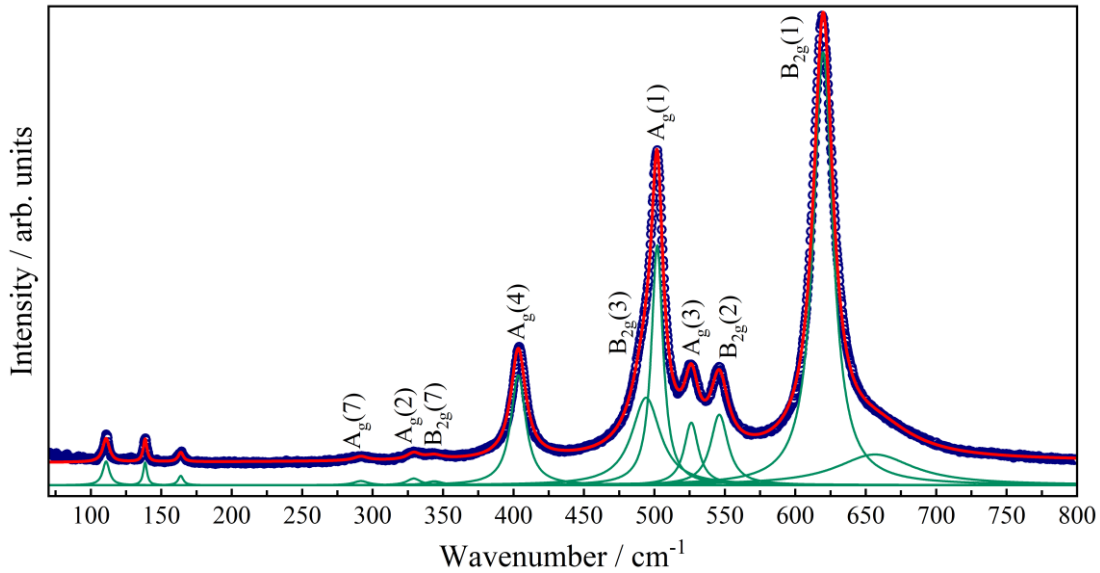

Figure 5.4. Raman spectra of the *o*-$TmMnO_3$ sample at room temperature.

The assignments of observed Raman modes on the *o*-TMO spectrum at room temperature can be made based on Raman spectra studies of *o*-RMO family[107,122–124]. In such studies, the authors show that the MnO_6 phonon positions have a R^{3+} ionic radius (r_R) dependence. Iliev *et al.*[123] reported a theoretical dynamic calculation model

for the r_R dependence of phonons positions for the most intense $A_g(3)$, $A_g(1)$ and $B_{2g}(1)$ phonons, showing that further decreases on r_R implies that the $A_g(3)$ frequency should be founded at higher than those observed for $A_g(1)$, while the $B_{2g}(1)$ mode should be the most intense of them.

In the case of *o*-TMO, we are able to infer that the external modes are located below 200 cm^{-1}, while those modes with high wavenumbers are related to MnO_6 octahedron internal modes. The three very weak modes located at 290, 329 and 343 cm^{-1} present symmetries $A_g(7)$, $A_g(2)$ and $B_{2g}(7)$, respectively. Those $A_g(7)$ and $B_{2g}(7)$ modes are related to basal octahedron oxygen motions along x and z directions, while the $A_g(2)$ mode can be related to in-phase MnO_6 rotations around the y-axis. The modes located around 404 and 493 cm^{-1} present symmetries $A_g(4)$ and $B_{2g}(3)$ assigned as out-of-phase MnO_6 rotations along x-axis and bendings, respectively. In the region of higher wavenumbers, the mode located at 502 cm^{-1} rises from the oxygen stretching having $A_g(1)$ symmetry, while the one located around 526 cm^{-1} has $A_g(3)$ symmetry being related to MnO_6 octahedra bending. Finally, the modes located at 546 and 619 cm^{-1} have B_{2g} symmetry and are assigned to in-phase O_2 "scissors-like" and stretching motions, respectively. Hence, we were able to assign 5 A_g and 4 B_{2g} modes from those 24 modes predicted on group theory analysis. A short description of the assigned Raman modes of *o*-TMO is shown in Table 4.

Table 4. Positions and assignment of the observed phonon modes in *o*-TMO Raman spectrum.

Frequence (cm^{-1})	Assignment	Motion
290	$A_g(7)$	O_1 (x)
329	$A_g(2)$	In-phase MnO_6 *y* rotations
343	$B_{2g}(7)$	O_1 (z)
404	$A_g(4)$	Out-of-phase MnO_6 *x* rotations
493	$B_{2g}(3)$	Out-of-phase MnO_6 bending
502	$A_g(1)$	O_2 antistretching
526	$A_g(3)$	MnO_6 bending
546	$B_{2g}(2)$	In-phase O_2 "scissors-like"
619	$B_{2g}(1)$	In-plane O_2 stretching

The observed Raman spectrum for *o*-TMO observed here is considerably different from the one reported for thin films by Shimamoto *et al*[119]. Nevertheless, on their thin film analysis, the authors observed a lower number of phonons in relation to those observed here. Besides that, the authors report that the phonon positions observed for thin films Raman spectra are shifted in relation to those reported for bulk samples of the majority of *o*-RMO family. This is indicative that for *o*-TMO this shift trending is not different.

The temperature-dependent Raman measurements of *o*-TMO were carried out below room temperature on the temperature range between 300 and 15 K. In reason of resolution limitations, given by loss of signal within the cryostat, we were able to follow the temperature dependent behavior of three A_g and three B_g modes with mixed symmetries (Figure 5.5), while the modes observed between 280 and 360 cm^{-1} were too weak to be monitored. Under cooling process, the Raman spectra did not present any remarkable change in terms of additional or suppressed bands. Only the usual high-frequency shift and the sharpening of vibrational modes were detected under temperature decrease, as consequence, the overall signature of Raman spectra is maintained along the investigated temperature range, which suggest that the orthorhombic phase of $TmMnO_3$ did not undergoes any structural phase transition in the investigated temperature range.

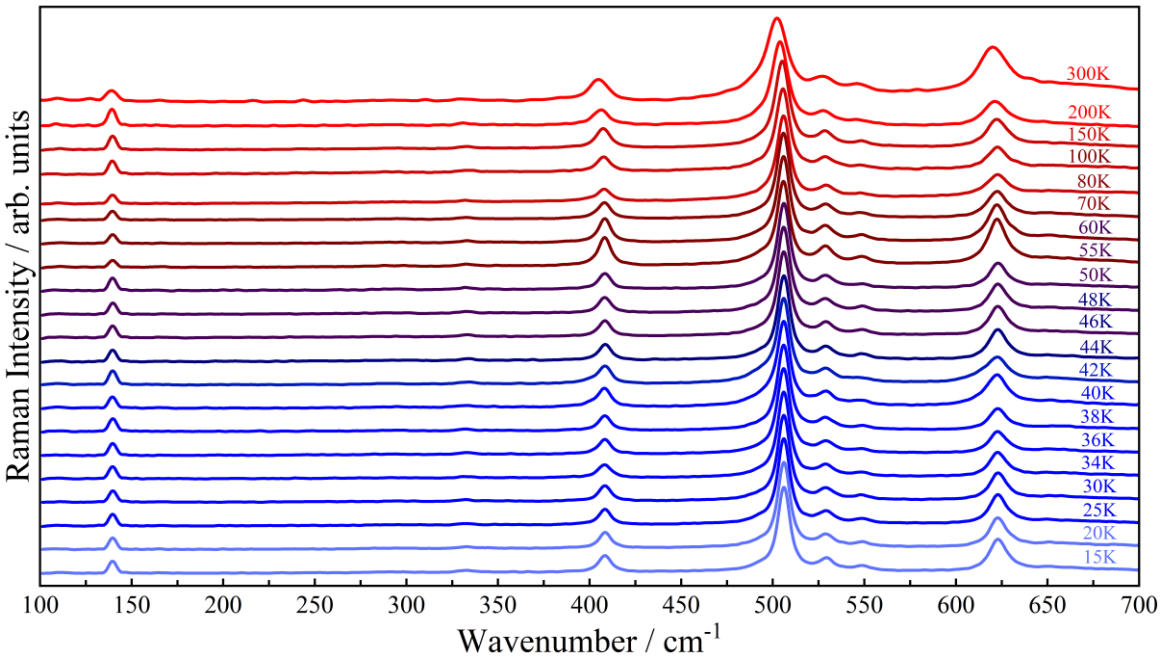

Figure 5.5. Temperature-dependent Raman spectra of *o*-TMO.

As discussed in section 1.4, In absence of significant structural changes, the temperature dependent behavior of a phonon of frequency ω and FWHM are mainly governed by the phonon anharmonicity as reported by Balkanski *et al*[26] in equations (1.5) and (1.6). In Figure 5.6 is showing the temperature dependence of selected phonon positions and its respective FWHM compared to those models.

As it can be seen, the temperature dependence of such phonon properties exhibits a renormalization in relation to the theoretical model nearby 44 K. This temperature has been reported as the magnetic transition point between the paramagnetic and the incommensurate AFM phase. Thus, the sudden hardening of frequency presented by such vibrations starting around the temperature in which the spin moments become aligned in the incommensurate ordered phase is an indication of a spin-phonon coupling between the spin moments and phonons lattice of *o*-TMO.

At this point is important to keep in mind that Pomjakushin *et al*[115] also reported a coupling between the chemical and the magnetic lattice for o-TMO below T_N, where the authors highlighted that the spin-lattice coupling in o-TMO is stronger than those observed for other compounds of o-RMO family. Based on this feature, the renormalization effects observed here on phonon frequencies also could be induced by the spin-lattice coupling instead of a spin-phonon coupling. Once FWHM is related to the phonon lifetime[89], the effects directly connected to lattice variations have no influence on this parameter, making this feature a key parameter to distinguish between phenomena generated by spin-lattice couplings and those generated by different kind of couplings as the spin-phonon coupling. Thus, the investigation of FWHM phonon become crucial to solve the ambiguity related to the origin of those frequency renormalizations. Based on this, the temperature dependent FWHM of such phonons were investigated carefully and departures from the temperature dependent anharmonic behavior of FWHM also could be noted for those selected modes. As observed in phonon frequencies, those deviations on FWHM also rises around 45 K, suggesting that the observed effects are originated by the spin-phonon coupling and not mediated by the spin-lattice coupling effects.

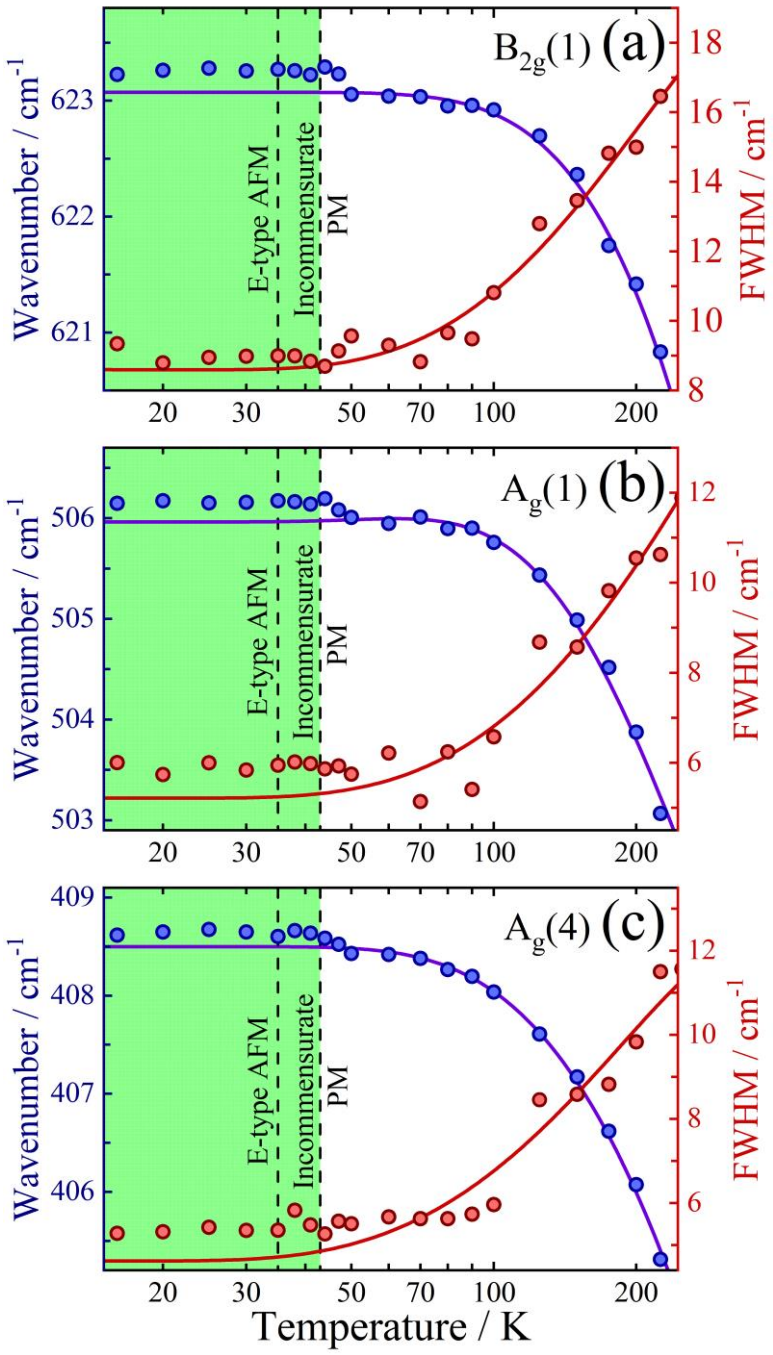

Figure 5.6. Temperature dependence of selected positions and FWHM phonons of orthorhombic $TmMnO_3$. Solid lines in purple and red indicate the fit based on Balkanski's model for phonons positions and FWHM, respectively, while the dashed lines are the magnetic transitions reported in the literature.

Similarly to *o*-TMO, the other compounds of *o*-$RMnO_3$ manganite family also showed a similar spin-phonon coupling starting at temperatures around those in which the rising of magnetic ordered phase are observed[34,49]. However, unlike other compounds of family, the o-TMO phonons presented a hardening effect on phonon positions instead a softening effect as observed by Laverdiere *et al.*[49] In addition, the

magnitude of phonons renormalization due to spin-phonon coupling observed for o-TMO are weaker in comparison to those observed for $PrMnO_3$[49] and $ErMnO_3$,[35] but are comparable to the one observed for the $A_g(1)$ phonon mode of $DyMnO_3$[49]. In the same study, the authors reported that the spin-phonon coupling are negligible in those compounds with small r_R and incommensurate AFM ordering, nevertheless, in case of *o*-TMO, the center and FWHM renormalization analysis are indicating that the spin-phonon coupling starts nearby the rising of the incommensurate AFM ordering.

It is also important to note that the renormalizations effects expected by such *o*-TMO phonons can are starting slightly above the reported T_N, indicating that the lattice phonons are sensible to magnetic moments even above the magnetic ordering temperature. In the same study mentioned on the last paragraph, Laverdière *et* a*l.*[49] highlight that the renormalizations observed for $LaMnO_3$ [125] and those reported by them for $PrMnO_3$, $NdMnO_3$, $SmMnO_3$ and $DyMnO_3$[49] also starts above or well above (around 30 K) the magnetic temperature ordering, T_N. In such cases, the authors reported that the renormalization observed above T_N could be explained by in-phase ferromagnetic interactions existing even in paramagnetic phases.[49]

As mentioned in section 1.4, the renormalization process expected by those phonon frequencies can be modeled by taking into account the static spin-spin correlation average function[28,29] and, following the approach reported by Granado *et al.*[27] showed in equation (1.15). However, in the case of incommensurate the incommensurate and the E-type magnetic orderings presented by o-TMO, we have:

$$\Delta\omega = \frac{K(T)}{m\omega}[2D_1\cos(\pi k_x) + D_2\cos(2\pi k_x) + D_3] \tag{5.1}$$

For the E-type AFM phase of o-TMO with $k_x = 0.5$, the relation (5.1) becomes:

$$\Delta\omega \propto \frac{[D_3 - D_2]}{m\omega}\left(\frac{M(T)}{M_0}\right)^2 \tag{5.2}$$

where, in this case, the NN contributions cancel themselves since each Mn^{3+} ion is surrounded by two sets of opposite spin moments ions[115]. This approach is the same as that reported by Laverdière *et al.*[49] for an E-type AFM phase.

Based on those considerations, in both magnetic phases of o-TMO, the phonon renormalization should be proportional to $(M(T)/M_0)^2$. Thus, the frequency

renormalization process ($\Delta\omega$) expected by the $A_g(4)$, $A_g(1)$ and $B_{2g}(1)$ phonons were analyzed as function of $(M(T)/M_0)^2$ data and are plotted in Figure 5.7 (panels a-c).

From the $\Delta\omega$ vs $(M(T)/M_0)^2$ analysis, it should be noted that the theoretical model for the correlation between the phonon frequency renormalization and the $(M(T)/M_0)^2$ is in accordance with the proposed models showing that the predicted model present a good fit for the o-$TmMnO_3$ spin-phonon coupling even in presence of the incommensurate and the E-type AFM phases. It is clear that there are a linear trending on $\Delta\omega$ below 44 K, however, the obtained slope of linear fit obtained for $B_{2g}(1)$, $A_g(1)$ and $A_g(4)$ phonons where -0.2074 ± 0.45308, -0.04841 ± 0.20784 and -0.15028 ± 0.34311, respectively. These very small values of linear slope shows that the $\Delta\omega$ as function of $(M(T)/M_0)^2$ is a constant (this feature also can be noted in the Figure 5.6 (a-c)) and the spin-phonon coupling have no more influence in such phonons below 35 K. This feature imply that in the E-type AFM phase, the factor $[D_3 - D_2]$ in equation (5.2) is null and D_3 and D_2 are equal and opposite each other, in good accordance with proposed by Laverdiere *et al*[49]. In contrast to the information reported about the general o-RMO family[49], the Figure 5.6 andFigure 5.7 shows that the increase of $\Delta\omega$ for *o*-TMO is observed around 47 K, close to the rising of incommensurate AFM phase and, according to the authors, in such phase the spin-phonon coupling should be negligible, suggesting that the *o*-TMO do not follows this trend.

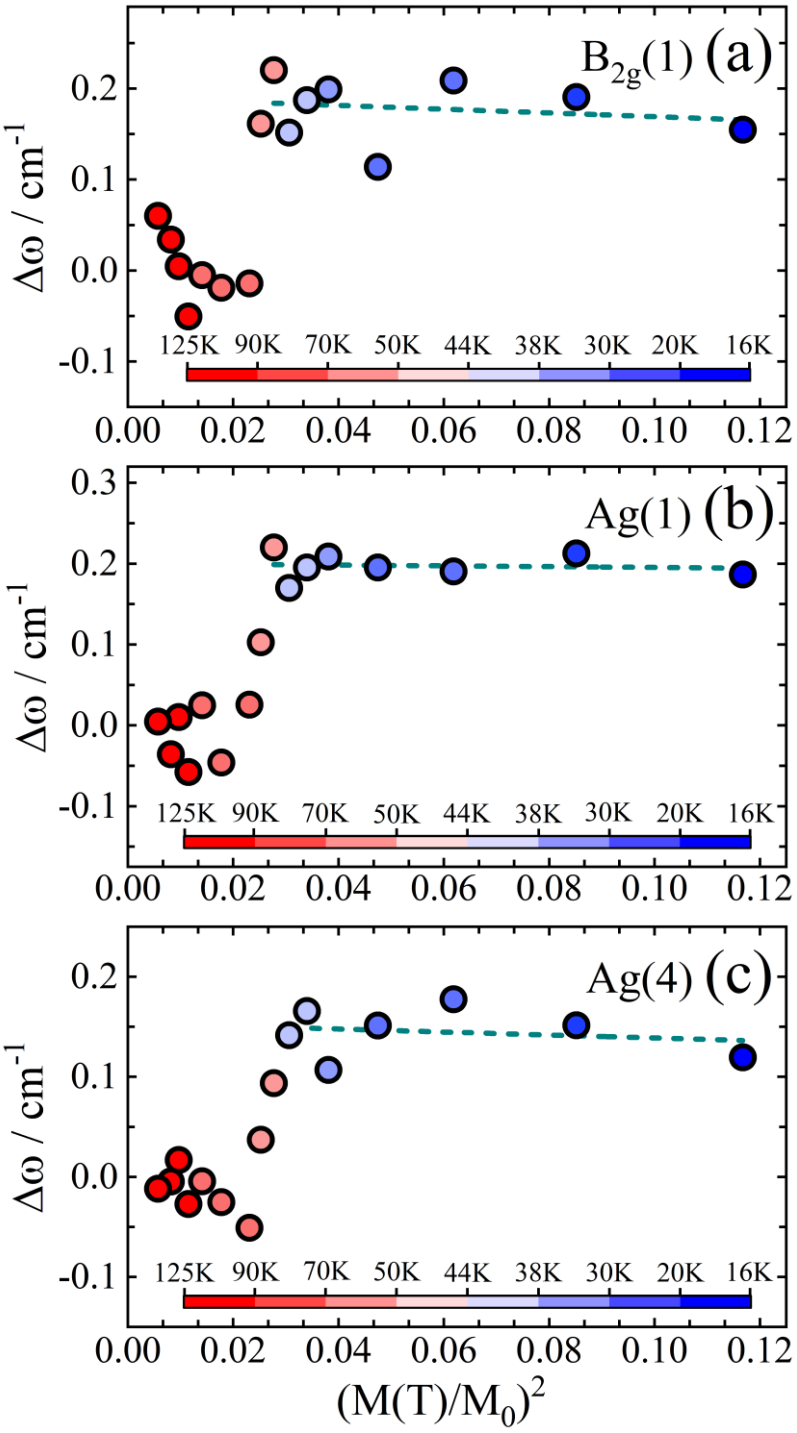

Figure 5.7. Panels a-c: Temperature dependence of the departure from anharmonic behavior of selected phonons as function of $(M(T)/M_0)^2$, the dark green dashed lines are the linear fit of data.

5.3 *$TmMnO_3$ Conclusions*

A HPHT strategy was performed to obtain *o*-TMO from *h*-TMO. The h-TMO phase was obtained by means of a conventional solid-state reaction in the air and the compound formation was confirmed through XRPD measurements. h-TMO was grounded and treated at HPHT procedure to form its orthorhombic phase. The initial characterization of o-TMO was carried by means of XRPD and magnetic susceptibility analysis in order to compare the fundamental properties of our samples with those reported in the literature.

Once the fundamental properties were checked with the literature, o-TMO was submitted to Raman spectroscopy analysis where 13 vibrational modes were observed and classified according to other compounds of the *o*-RMO family. Then, the samples were submitted to temperature variations below room temperature. The temperature dependent behavior of *o*-TMO. Our results revealed renormalizations process on the frequency and FWHM parameters for the $A_g(4)$, $A_g(3)$ and the $B_{2g}(1)$ phonons, which are related to MnO_6 vibrational motions. These features were observed below 48 K where is reported the incommensurate AFM ordered phase rises, indicating that this compound exhibit a spin-phonon-coupling even at the incommensurate magnetic ordered phase. In addition, based on the observed linear behavior of phonons deviations in function of the experimental magnetization, the $\Delta\omega$ vs $(M(T)/M_0)^2$ analysis confirmed that the spin-phonon coupling starts around 48 K in all coupled phonons and probed that this linear behavior becomes constant below 32 K, where the magnetic structure changes from incommensurate to a E-Type AFM phase. In contradiction to previously reported results, these considerations confirm that the spin-phonon coupling starts at the incommensurate ordered phase and becomes null at the E-type AFM phase.

The low magnitude of phonon frequency renormalizations indicates the spin-phonon coupling on *o*-$TmMnO_3$ is weaker than those reported for *h*-TMO phase and A-type AFM ordered *o*-RMO compounds, but still comparable with other compounds of the o-RMO family, as $DyMnO_3$.

6. The Spin-phonon coupling in $BiCrO_3$

Chromates with perovskite structure $ACrO_3$ has been investigated intensively during the last years due to their interesting properties and applications. While rare-earth-based compounds exhibit intriguing magnetic properties[126–128] and multiferroic behavior at low temperatures[129], Bi-based chromites are interesting because they are lead-free ferroelectric and multiferroic materials[130–132].

Particularly, $BiCrO_3$ (BCO) crystallizes in a monoclinic structure, which belongs to the C2/c space group. Such structure transforms into an orthorhombic Pnma structure (GdFeO3-type phase) around 420 K[101]. However, it was observed that the Pnma structure is still present at low temperatures in the BCO compound. In fact, it is assumed that a C2/c - Pnma phase coexistence is a stable state[133,134]. This feature directly drives the BCO magnetic properties since the long-range G-type antiferromagnetic (AFM) ordering around T_N = 110 K is associated to the C2/c phase, while two anomalies at 40 K and 165 K are associated to the Pnma one[134]. In addition, a magnetic anomaly around 75 K was also reported being characterized by a large increase on magnetization curve in the interval between 80 K and 60 K. This event is due to the magnetic moments alignment, where the spin moments form a 50º angle with the monoclinic b direction[135], preserving the well-ordered G-type antiferromagnetic structure[134]. Two interesting features in the BCO magnetic behavior are the frequency-dependent magnetic properties below 40 K, which still need further explanations, and the AFM transition at 110 K, being, in fact, a two-step transition, at 109 K and 111 K[134,135].

Concerning BCO electric properties there are still many open questions. Dielectric properties of bulk BCO were investigated at high temperatures by Niitaka *et al* [101], where they observed an anomaly in the dielectric constant around 420 K. However, the peak observed in the dielectric constant at different frequencies were very broad and showed strong frequency dependence indicating a possible extrinsic origin, probably due to conductivity. However, based on first-principle density functional calculations, an antiferroelectric behavior attached to the structural distortions at high temperatures was predicted in BCO by Hill *et al*[136]. In thin films, the contradictions remain. For example, Murakami et al[130] reported the growing of ferroelectric BCO at room temperature by pulsed laser deposition (PLD) in $LaAlO_3$(001), $SrTiO_3$ (001) and $NdGaO_3$ (110) substrates. Meanwhile, Kin *et al*[137] observed that BCO thin films growth by PLD on $SrTiO_3$ (001) with $SrRuO_3$ bottom electrode exhibit antiferroelectricity with an electric

field induced ferroelectric phase, as confirmed by double hysteretic behaviors in the electric field dependence of dielectric constant and polarization. They also observed that the dielectric constant exhibits a maximum at 140 K, which was ascribed to T_N. In thin films, such discrepancy can be induced by different deposition conditions, which imply different stress and structures. Although both scientific teams reported thick thin films (50 nm and 200 nm), in which strain should not be strong.

The Raman spectrum of polycrystalline bulk and thin films of BCO were firstly reported by Himcinschi *et al*[138]. In this study, the authors confirmed the monoclinic to orthorhombic phase transition at 400 K described by Niitaka *et al*[101], by analyzing the temperature dependent Raman spectrum on the temperature range between 500 and 87 K. However, the authors did not report any spectral anomaly on the interval between 120 and 87 K, which could be related to the reported magnetic events.

Despite the contradictions on the dielectric property, the possible observed coupling between electric and magnetic ordering suggests that the magnetic ordering can also couple with the lattice. In this way, the Raman scattering spectroscopy is a powerful technique due to its sensibility to detect magnetic orderings through the coupling with the phonon lattice, which was verified mainly in perovskites compounds[99–101]. Thus, the temperature dependence of the Raman-active phonons below room temperature can help to elucidate BCO magnetic and electric behavior and their coupling.

6.1 *$BiCrO_3$ Synthesis Procedure*

Polycrystalline samples of BCO were synthesized through solid state reaction under high pressure and high temperature (HPHT). Stoichiometric amounts of Bi_2O_3 (99.9%) and Cr_2O_3 (99.9%) were ground in an agate mortar, sealed into platinum capsules and treated by means of HPHT solid-state reaction in a Walker type multianvil press in hand of Centre of Science at Extreme Conditions (CSEC), located at School of Chemistry of University of Edinburgh. To synthesize the BCO samples obtained here, two attempts were performed and checked by means of XRPD until reaches the optimized conditions to favor the formation of the monoclinic phase of BCO (the X-ray powder pattern of two attempts are shown in Figure 6.1). In the first attempt, the reaction chamber was firstly pressurized until the system reached 6 GPa when it was heated from room temperature up to 1650 K. At this point, the system was kept in these conditions for 60 min. In sequence, it was quenched to room temperature (RT) and the pressure was slowly released. In this case, the sample seems to have undergone a fusion process and the XRPD pattern shows the existence of different phases from the one intended.

As a second attempt, the reaction chamber was pressurized until the system reached 6 GPa again, but in this case, the system was heated at 1273 K. In sequence, the system was maintained under 6 GPa and 1273 K during 60 min and then, it was quenched to room temperature and the pressure was slowly released. The resultant polycrystalline samples of this attempt were dark-green dense pellet and the XRPD pattern confirmed the formation of the desired compound.

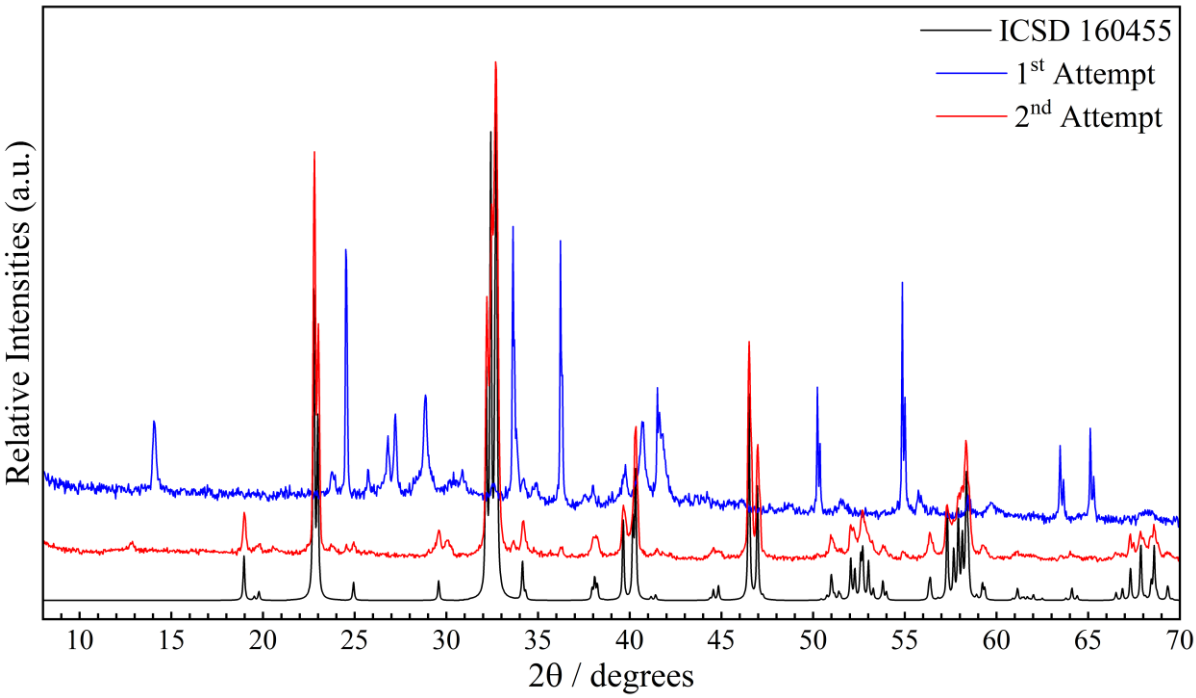

Figure 6.1. XRPD diffraction patterns of the two attempts to obtain the monoclinic phase of BCO. The black XRPD pattern is the one calculated from the reported monoclinic structure of BCO[139] and deposited on the ICSD database.

6.2 *Results and Discussions*

After reach the optimized synthesis conditions, the dark green polycrystalline pellets of $BiCrO_3$ were submitted to X-ray diffraction measurements whose results are shown in Figure 6.2. The obtained samples were analyzed by the Rietveld method presenting a monoclinic perovskite-type structure belonging to *C2/c* space group, whose lattice parameters are *a*: 9.472Å, *b*: 5.481Å, *c*: 9.580Å and *β*: 108.574º with eight formula units per unit cell, in good agreement with those reported by other authors.[101,139,140] Small amounts of $Bi_2O_2CO_3$ and the *Pnma* phase were detected as secondary phases with fraction weight of 2% and 8%, respectively, as usual in such BCO synthesis procedure[135,141].

As a standard perovskite, BCO crystalline structure exhibits a corner-shared CrO_6 octahedra lattice, while the Bi ions are located in the free space between such octahedra (Figure 6.3). In this configuration, the octahedra are tilted according to Glazer tilting system $a^-b^-b^-$ in relation to the ideal cubic perovskite[142].

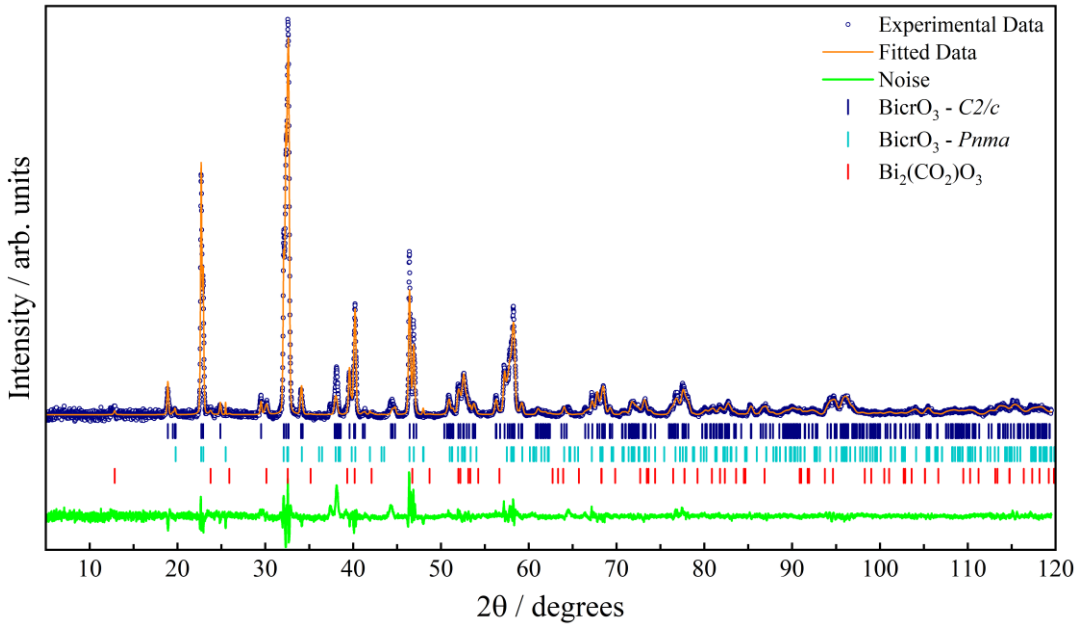

Figure 6.2. XRPD pattern obtained from as-synthesized BCO samples. The dark blue line is the BCO data as-synthesized, the darkblue bars indicate the peaks of standard monoclinic *C2/c* sample[139] (ICSD number 160455), the red bars indicate the *Pnma* phase of BCO phase[139] (ICSD number 160454) and the red bars indicate the BiO_2CO_3 (ICSD number 36245).

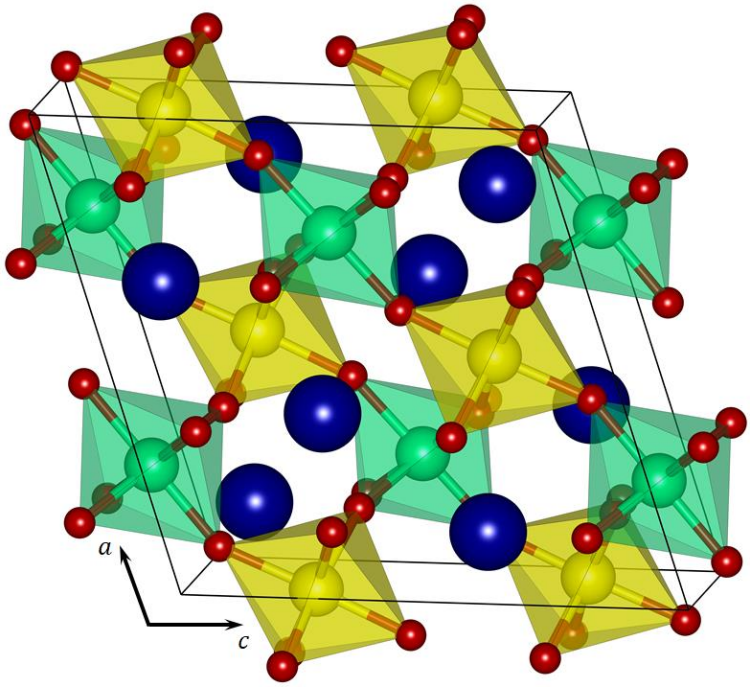

Figure 6.3. The crystalline structure of monoclinic BCO. In this figure, the red spheres are the O^{2-} ions, the blue spheres are the Bi^{3+} ions and the yellow and green spheres are the Mn^{3+} ions. The different colors of highlighting the G-type antiferromagnetic ordering through different colors of CrO_6 octahedra.

The Figure 6.4 (a) shown the zero field cooled (ZFC) and field cooled (FC) magnetic susceptibilities of BCO between 3 and 300 K and the Figure 6.4 (b) is showing the magnetization of BCO as function of magnetic field (magnetic hysteresis loop) measured at 2K. This magnetic profile of BCO samples is in agreement with the magnetic behavior reported in previous works[135,139,140]. The ZFC and FC curves are showing the appearance of magnetic contributions around 110K attributed to the rising of a G-Type antiferromagnetic structure. At this temperature also can be noted a sudden rise on susceptibility, in literature this event has been associated with a weak ferromagnetic ordering[101,134,135,140]. In sequence, the curves show a large increase on the magnetic susceptibility intensity around 80K, which is associated with a spin reorientation event[135]. In the inverse of magnetic susceptibility (presented in the inset of Figure 6.4(a)) also become clear the magnetic events at 110 and 80 K.

The first derivate of magnetic susceptibility ($\partial\chi/\partial T$) (Figure 6.4 (b)) also highlight the magnetic events around 110 and 80 K and present a very slight anomaly around 40 K. Based on published works[143], two additional anomalies on magnetic susceptibility were expected around 165 and 40 K, indicating that the slight anomaly around 40 K in $\partial\chi/\partial T$ analysis should be one of those reported events.

Thus, from the magnetic profile of the samples synthesized in this study, it is clear that the BCO samples did not exhibit another magnetic phenomenon besides those related to antiferromagnetic G-type ordering at 110 K and the spin alignment around 80 K. These characteristics are indicative of a well-ordered sample, confirming that the small amount of impurities has no influence on magnetic behavior of samples studied here.

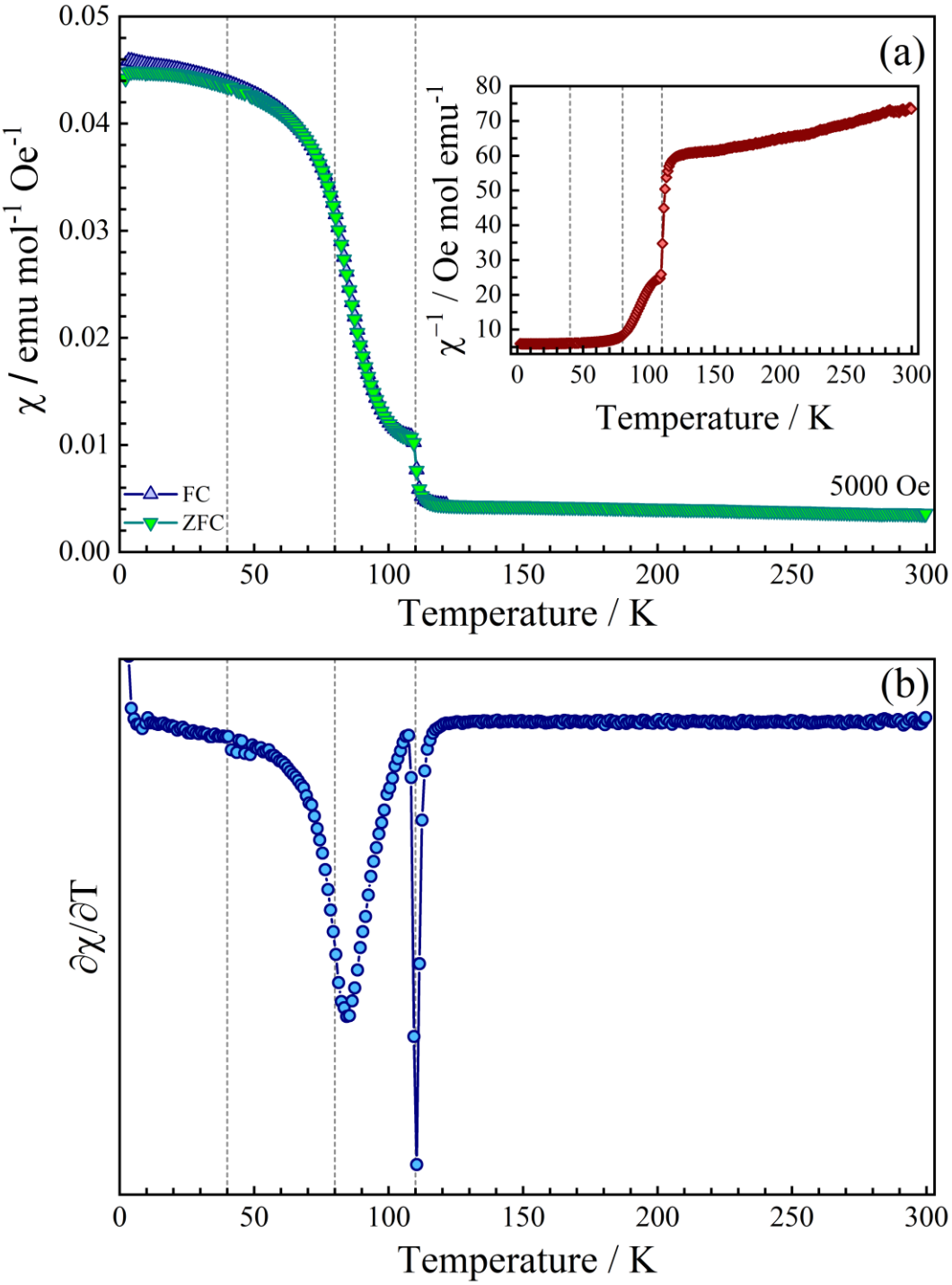

Figure 6.4. Magnetic properties of BCO. (a) Magnetic susceptibility curves obtained from BCO samples. The blue triangles are shown the zero field cooling and the green triangles show the field cooling results. The inset panel is showing the inverse of magnetic susceptibility. (b) the first derivate of temperature-dependent magnetic susceptibility ($\partial\chi/\partial T$).

In an earlier work, Andersson [144] suggested that not only the nearest neighbor (NN) interactions, but also the next nearest neighbor (NNN) interactions have an important role to understand complex magnetic orderings in antiferromagnetic materials, especially when they present a high θ_{CW}/T_N ratio. In the case of BCO, each Cr ion is surrounded by one set of two Cr ions which can be classified as NN, whose distances are 3.87 and 3.94 Å, and one set of two Cr ions associated to NNN, whose distances are 5.47 and 5.57 Å. The fitted effective magnetic moments (μ_{eff}) of Cr^{3+} ions in the BCO structure was reported of order to $4\mu_B$ and the Weiss constant (θ_{CW}) around $-360\ K$[145], giving an approximate $|\theta_{CW}/\ T_N|$ ratio of 3.27. This value highlight the complex character of BCO antiferromagnetic structure specially when compared to a ratio of 3.09 reported for $YCrO_3$[33], which also present a weak ferromagnetic phase in a complex competition with the main antiferromagnetic phase. Other indicatives of strong NN and NNN interactions are the estimated values of its respective exchange constants J_1 and J_2 (Figure 6.5). Considering the molecular field theory, these interaction constants can be related to the Currie-Weiss constant (θ_{CW}) and the Néel Temperature (T_N) following the approach reported by Tsushima et al[146] where:

$$J_1 = \frac{K_B}{8s(s+1)} \cdot (\theta_{CW} - T_N) \tag{6.1}$$

$$J_2 = \frac{1}{2} \cdot \frac{K_B}{8s(s+1)} \cdot (\theta_{CW} + T_N) \tag{6.2}$$

The exchange constants where estimated by using the experimental values of θ_{CW} and T_N, giving $J_1 = -10.89$ and $J_2 = -2.90$ cm^{-1}. The values associated to BCO were lower than those reported for $SmCrO_3$ ($J_1 = -13.54\ cm^{-1}$ and $J_2 = -4.64\ cm^{-1}$)[147], but they are still comparable with those of $YCrO_3$ ($J_1 = -13.48$ and $J_2 = -3.45\ cm^{-1}$), indicating that the J_2, related to the NNN interactions, is not negligible when compared with the one related to the interactions between NN ions (J_1), highlighting the complex character of the magnetic interactions in this system.

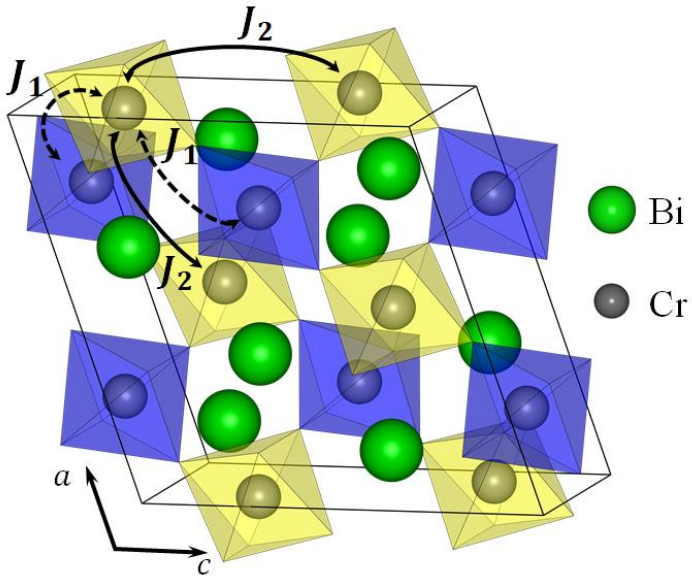

Figure 6.5. Schematic representation of exchange paths on unit cell of BCO (the oxygen atoms were omitted).

Once the formation of BCO was confirmed by PDXR and the magnetic behavior is in good accordance with the one reported in the literature, the BCO samples were submitted to Raman spectroscopy analysis. The BCO Raman spectrum measured at room temperature is shown in Figure 6.6. According to the group theory analysis based on the site occupation of the $C2/c$ monoclinic structure, 27 Raman-active modes are predicted at room temperature (Table 5). The Raman-active vibrational modes at the Γ point of the Brillouin zone[83] can be decomposed in terms of the irreducible representations of the C_{2h} point group as $13A_g \oplus 14B_g$. In Figure 6.6, 13 of the 27 predicted Raman-active modes are observed, which is in good agreement with the results previously reported by Himcinschi *et al*[138].

Table 5. Irreducible representation of the vibrational modes of monoclinic BCO.

Ion	Site	Symmetry	Contribution
Bi	$8f$	C_1	$3A_g \oplus 3A_u \oplus 3B_g \oplus 3B_u$
Cr_1	$4e$	C_2	$A_g \oplus A_u \oplus 2B_g \oplus 2B_u$
Cr_2	$4d$	C_i	$3A_u \oplus 3B_u$
O_1	$8f$	C_1	$3A_g \oplus 3A_u \oplus 3B_g \oplus 3B_u$
O_2	$8f$	C_1	$3A_g \oplus 3A_u \oplus 3B_g \oplus 3B_u$
O_3	$8f$	C_1	$3A_g \oplus 3A_u \oplus 3B_g \oplus 3B_u$
		$\Gamma_{TOT} = 13A_g \oplus 16A_u \oplus 14B_g \oplus 17B_u$	
		$\Gamma_{Ac} = A_u \oplus 2B_u$	
		$\Gamma_{IR} = 15A_u \oplus 15B_u$	
		$\Gamma_{Raman} = 13A_g \oplus 14B_g$	

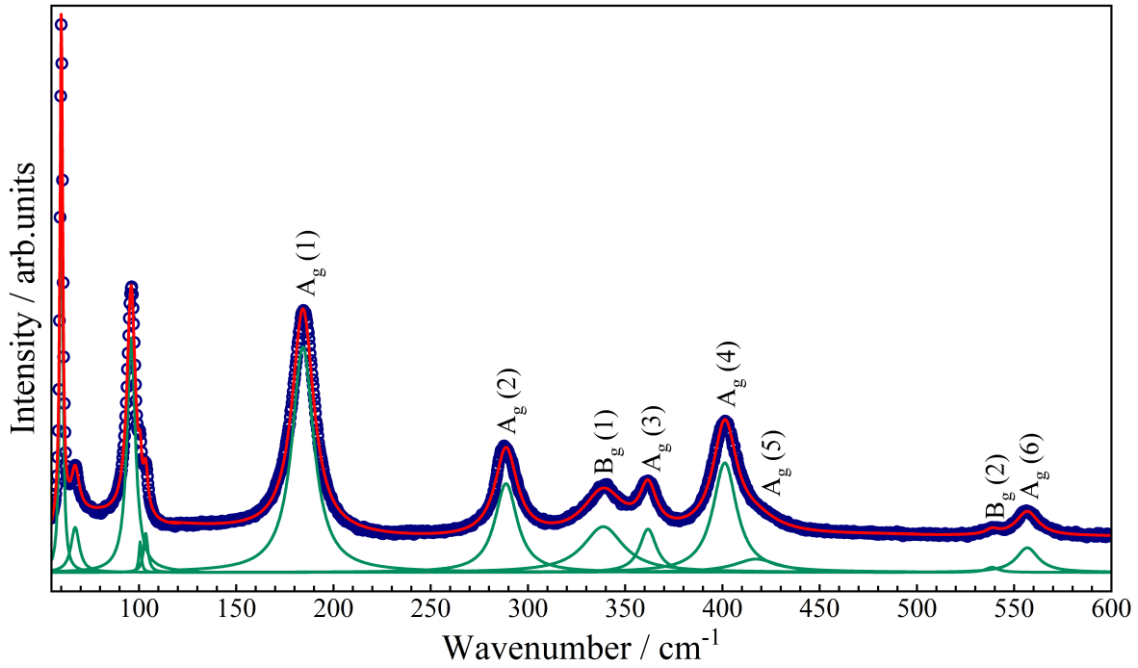

Figure 6.6. Room Temperature Spectrum of BCO. Open blues circles show the experimental data fitted with individual Lorentzian. The red solid line indicates the best fit for the experimental data.

The assignment of the observed Raman modes based on those reported for the ABO_3 perovskite family[148–151] is shown in Table 6. In the BCO Raman spectra, the external modes are located below 180 cm^{-1}, while those modes with higher wavenumbers are due to the CrO_6 octahedron internal modes. The modes located around 184 and 362 cm^{-1} have A_g symmetry and are related to in-phase y rotations and out-of-phase x rotations, respectively. The modes observed at 289 and 340 cm^{-1} have A_g and B_g symmetries, respectively, being related to the basal octahedra oxygen motion along x and $-z$ axis. The octahedra bending and out-of-phase bending have A_g symmetry and are observed at 402 and 417 cm^{-1}, respectively. Finally, the mode located at 538 cm^{-1} has B_g symmetry and it is due to the anti-stretching octahedra vibrations. It is notable that on this study the A_g modes are more intense that B_g ones, this finding is in agreement with the results reported for the monoclinic phase of $BiMnO_3$[152] and the polarized measurements performed by Talkenberger et al.[153] and Himcinschi et al.[138] for the monoclinic BCO phase.

BCO samples were also submitted to Raman temperature dependent analysis. In this experiment, it was possible to monitor the temperature dependent behavior of six A_g and two B_g internal modes with mixed symmetries under cooling from 300K to 10K. Figure 6.7 exhibits the temperature-dependent Raman spectra obtained for BCO. Since

this compound does not exhibit structural phase transitions in the investigated temperature range, it is not possible to note any remarkable change or anomaly in terms of additional or suppressed bands in the Raman spectra. Only the usual high-frequency shift and modes sharpening were observed, which are understood by considering the lattice contraction and reduction of thermal vibrations. In this way, the overall signature of Raman spectra is maintained along all the investigated temperature range.

Table 6. Positions and assignments of the observed Raman modes in BCO Raman spectrum.

Wavenumber (cm^{-1})	Symmetry	Main atomic motions
185	$A_g(1)$	BO_6 in-phase y rotations
289	$A_g(2)$	O_1(x), A(-x)
340	$B_g(1)$	O_1(-z), A(z)
362	$A_g(3)$	BO_6 out-of-phase x rotations
402	$A_g(4)$	BO_6 bending
417	$A_g(5)$	BO_6 out-of-phase bending
538	$B_g(2)$	O_2, O_1 anti-stretching
555	$A_g(6)$	---

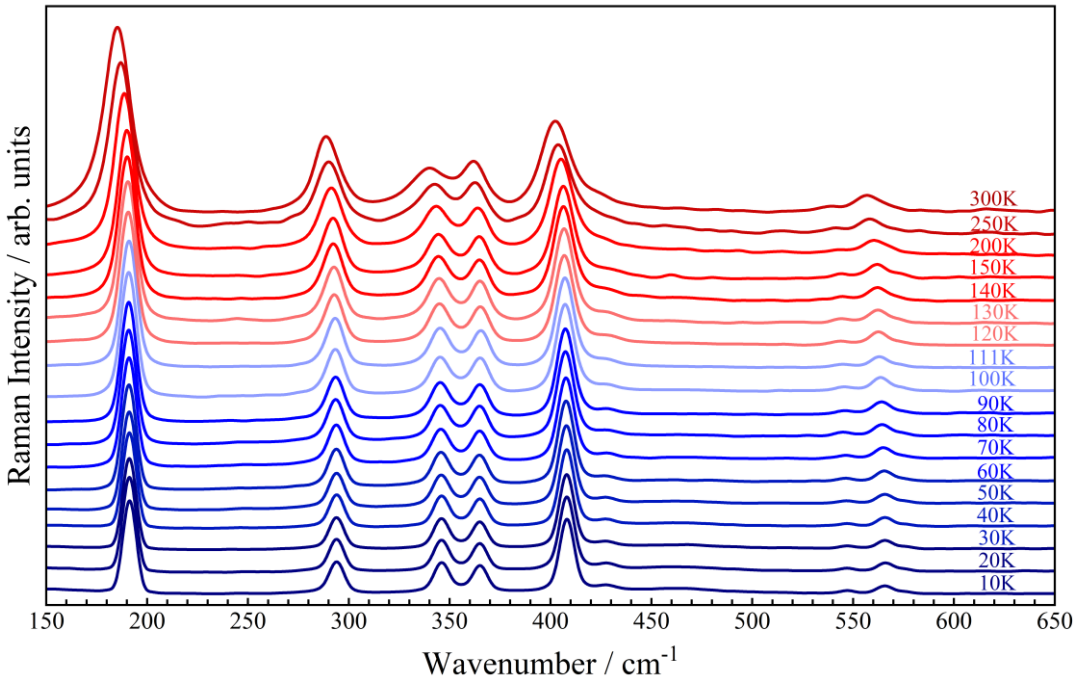

Figure 6.7. Temperature-dependent Raman spectra of BCO.

As mentioned in the previous chapters, in absence of structural changes, the temperature-dependent behavior of a phonon mode of frequency ω is mainly governed

by the phonon anharmonicity hardening, in which, according to Balkanski's model[26], the temperature-dependence of the FWHM and phonon frequency are given by the equations (1.5) and (1.6), respectively. In Figure 6.8, it is shown the temperature dependent behavior of selected phonon positions and their FWHM compared with the Balkanski's model.

The temperature dependence of such phonons exhibits a renormalization from the theoretical model at 110K for the $A_g(1)$, $A_g(3)$, $B_g(2)$ and $A_g(6)$ modes (Figure 6.8 a, b, c and f), while the $B_g(1)$ and $A_g(4)$ showed this effect only below 80 K (Figure 6.8 (d) and (e)). The stronger deviations are observed in $B_g(2)$ and $A_g(6)$ modes, reaching values around 3-4 cm^{-1}. At this point, should be noted that T_N = 110 K is the temperature at which the AFM ordering is observed in BCO, while 80K is the temperature where the spin moments realign around b axis in the monoclinic structure[135].

Such changes on the phonon positions suggest a spin-phonon coupling in BCO at these temperatures. As mentioned before, the FWHM is related to the phonon lifetime[89], as a consequence this parameter becomes not sensitive to thermal lattice variations. Thus, the FWHM analysis is an important tool to distinguish between events related to subtle volume changes due to exchange-striction[40] or magnetostriction effects and phenomena related to coupling effects[154]. In this way, the FWHM of all selected modes presented subtle deviations from the expected behavior at 110 and 80 K indicating the presence of a spin-phonon coupling at these temperatures. The poor FWHM fitting of $B_g(2)$ mode above 110K is due to the very low intensity of this mode in comparison with the remaining ones.

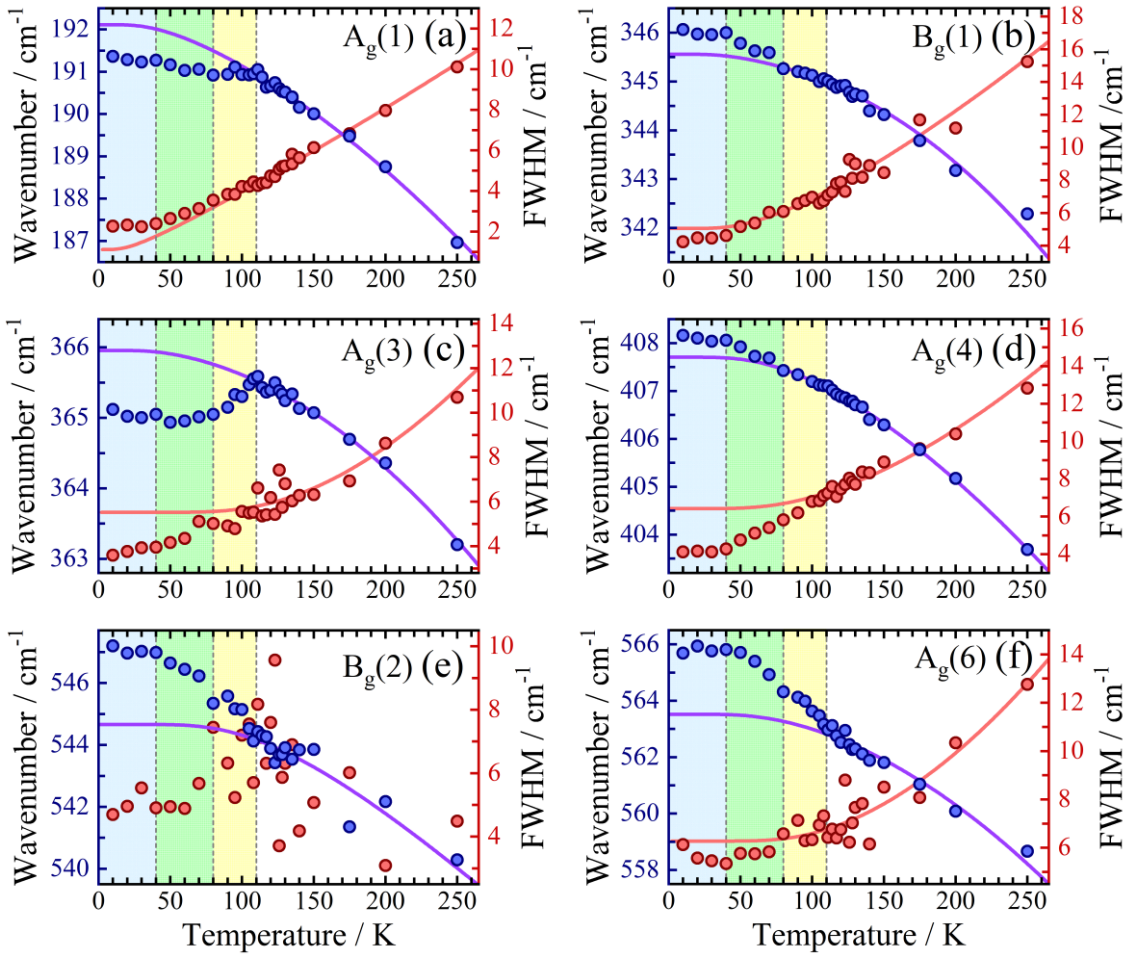

Figure 6.8. Panels a-f: Temperature dependence of the phonon energy and full width at half maximum (FWHM) of selected Raman-active modes of BCO. Solid lines are the fit of position and FWHM phonons based on the Balkanski's model[26] and the dashed lines are the magnetic events reported in the literature.

The variation of the frequency and linewidth presented by the phonons around the temperature of the BCO magnetic events suggest that magnetic ordering on BCO induces a spin-phonon coupling at these temperatures. The temperature dependent behavior of the Raman spectra of the $RCrO_3$ family was reported by Bahdram et al[155]. In this study, the authors observed similar spin-phonon couplings confirmed through FHWM analysis in samples where the R^{3+} site is occupied by a magnetic ion. In addition, Mahana et al[40] recently reported the spin-phonon coupling of $GdCrO_3$ in which the phonon frequencies also presented a mix of hardening and softening effects below T_N, as observed in our BCO study. In both cases, the reported renormalizations were in order of 1 - 3 cm^{-1} in good accordance with the magnitude of the renormalizations observed here.

Besides the events at 110 and 80 K, the Raman results also revealed very subtle changes on the phonon behavior below 40 K, temperature at which the phonon positions become almost constant. This feature is very weak in comparison with those observed

for the magnetic events at higher temperatures, but still is an indicative that the Raman modes in BCO are also sensitive to the magnetic event at 40 K reported by Belik et al[145]. However, further observations are necessary to confirm this assumption.

As mentioned before, the phonon frequency departure from the expected anharmonic behavior of a given vibrational mode as a function of the temperature due to a spin ordered phase can be described taking into account the spin-spin correlation function[28,29]:

$$\Delta\omega \equiv \omega - \omega_0 = \lambda\langle\vec{S}_i \cdot \vec{S}_j\rangle \tag{6.3}$$

At this point is important to remind that the λ factor is a coupling constant and $\langle\vec{S}_i \cdot \vec{S}_j\rangle$ denotes a statistical-mechanical average for adjacent spins on opposite sublattices.

In the case of BCO, the hardening effect observed on $B_g(1)$, $A_g(4)$, $B_g(2)$ and $A_g(6)$ are in agreement with the general trending of AFM materials, while the $A_g(3)$ and $B_g(2)$ modes do not follow this tendency, indicating that each phonon mode has a particular and independent λ factor.

As mentioned before, a similar mix between hardening and softening frequencies behavior has been reported for $GdCrO_3$ [40], $YCrO_3$ [33] and $BiMnO_3$ [156] samples. In the last two cases, the authors attribute this mixed behavior to a competition between a weak ferromagnetic and the antiferromagnetic phases presented by these materials. For such cases, Wakamura et al[157] proposed a theoretical model in which the phonon renormalization (Δω) can be interpreted by:

$$\Delta\omega \propto -k_1\langle S_a \cdot S_b\rangle + k_2\langle S_c \cdot S_d\rangle \tag{6.4}$$

where k_1 and k_2 are spin dependent force constants deduced from the derivatives of the exchange integrals with respect to the phonon displacements. In this way, k_1 is associated with ferromagnetic NN, while k_2 is related to the antiferromagnetic NNN exchange[158]. In this model, the spin correlation function of the nearest and the next nearest neighbors have the same temperature dependence[158] inducing the same correlation function for $\langle S_a \cdot S_b\rangle$ and $\langle S_c \cdot S_d\rangle$. In this way, the equation (5.3) reduces to equation (6.4) where the complex λ factor arise from the difference $k_2 - k_1$, assuming different values for each phonon mode.

For BCO, a weak ferromagnetic order[101,134,135,140] evidenced by a sudden increase on magnetic susceptibility (Figure 6.4 (a)) is reported in coexistence with the G-type antiferromagnetic phase. Thus, this approach could explain the observed phonons behavior, in which a softening effect is presented by the $A_g(1)$ and $A_g(3)$, while other modes presented a hardening tendency.

The spin-phonon coupling mechanism proposed by Granado et al[27] describing the phonon renormalization induced by the spin-phonon coupling for perovskite structures can be described as:

$$\Delta\omega(T) = \omega_{anh}(T) - \omega(T) \propto \frac{M^2(T)}{M_0} \tag{6.5}$$

where $M(T)$ is the average magnetization per magnetic ion at the temperature T and M_0 is the saturated magnetization. As mentioned before, this model works well for different perovskites even for those presenting antisymmetric phonon renormalizations[31,40,44], which is the case of BCO. In this way, based on the equation, the Figure 6.9 shows $\Delta\omega$ as function of $(M(T)/M_0)^2$ for the investigated phonons. As observed in other perovskite compounds[36,39,42,43,46,89,159], these results confirm the existence of a linear correlation between the renormalization of the phonon energies and $(M(T)/M_0)^2$, in accordance with the proposed model.

The correlation between the magnetization and the renormalized phonon positions for the $B_g(1)$ and $A_g(4)$ modes (Figure 6.9 (d) and (e), respectively) exhibits, as expected, a clear linear correlation just below 80 K. These results agree with the existence of a weak spin-phonon coupling which, for these vibrational modes, appear only below the temperature at which the magnetic moments undergo a slight reorientation process.

In the case of $A_g(1)$ and $A_g(3)$ phonons (Figure 6.9 (a) and (b), respectively), it can be noted that the linear behavior appears around 110 K where the $\Delta\omega$ increases linearly with the square of the magnetization. However, below 80 K there is a slight change in the linear behavior of both phonons. These findings indicate that although the spin-phonon coupling starts at 110 K, these phonons also are also sensitive to the spin reorientation below 80 K.

The same two steps spin-phonon coupling effect is observed for the $B_g(2)$ and $A_g(6)$ phonons (Figure 6.9(c) and (f), respectively). In both cases, there is a linear

correlation between $\Delta\omega$ and $(M(T)/M_0)^2$ below 110 K, but at 80 K, there is a clear slope change associated with the spin reorientation phenomenon.

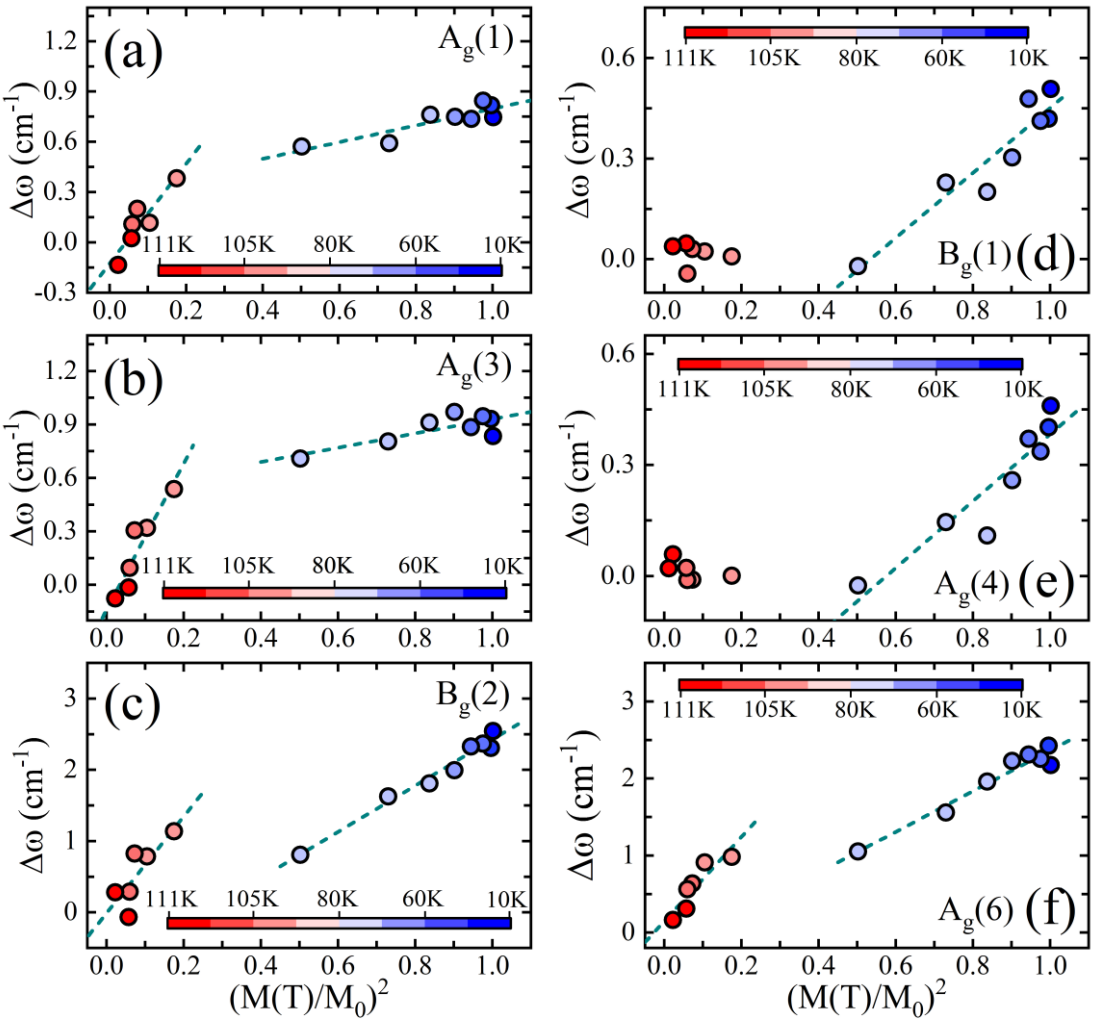

Figure 6.9. panels a-f: Temperature dependence of the departure from the anharmonic frequency behavior of selected phonons as function of $(M(T)/M_0)^2$, the dark green dashed lines are guides for eyes to show the linear behavior of data.

The hydrostatic pressure dependence behavior of the $BiMO_3$ family presenting monoclinic $C2/c$ structure was investigated by Belik *et al*[160] through SXRPD. In this study, the authors reported a $C2/c$ to $P2_1/c$ phase transition for $BiMnO_3$ followed by another phase transition to a $Pnma$ structure. This sequence of transitions presents interesting magnetic effects as changes in the magnetic ordering, Jahn-Teller distortions and orbital ordering, classifying it as a peculiar high pressure behavior. For the BCO sample, the authors did not observed the presence of a second monoclinic phase, reporting that the BCO system changes from $C2/c$ to $Pnma$ structure which may induces changes on magnetic properties as observed for $BiMnO_3$. Based on these results, the BCO samples were also submitted to SXRPD analysis in order to investigate the structural stabilization of this compound under pressure variation. Figure 6.10 shows the pressure-dependent SXRPD patterns from ambient pressure up to 11.00 GPa. For these analyzes the samples were sealed into a gas-membrane DAC and the oil mineral (nujol) was used as hydrostatic medium.

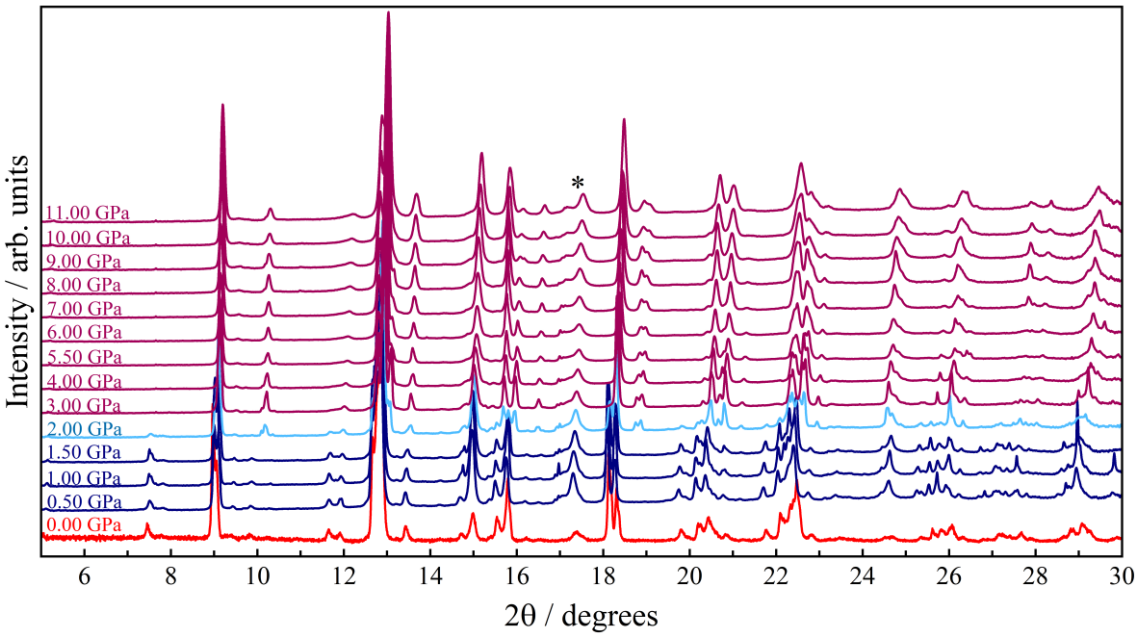

Figure 6.10. Pressure-dependent SXRPD pattern of BCO samples. The asterisk is marking the position of the gasket diffraction peak.

The initial diffraction pattern confirms the monoclinic C2/c phase with the presence of $Bi(CO_3)O_2$ and the $Pnma$ orthorhombic BCO secondary phases, as already presented by the XRPD results cited previously in this chapter. Above ambient pressure it can be seen that the monoclinic phase remains as the main phase until 2.00 GPa where new diffraction peaks are noted together those related to the $C2/c$ phase, characterizing a phase coexistence region. In addition, at 3.00 GPa the system already completed this

phase transition, but the observed value of the phase transition is quite different from the one reported for Belik *et al*[160].

In order to obtain more information about the diffraction pattern at 3.00 GPa, the Le Bail method was employed to investigate the new high-pressure phase. The Le Bail analysis suggested a better solution with a P2/c monoclinic phase with addition of the orthorhombic BCO and $Bi(CO_3)O_2$ as secondary phases, in contrast to those results reported previously for the BCO high-pressure phase.

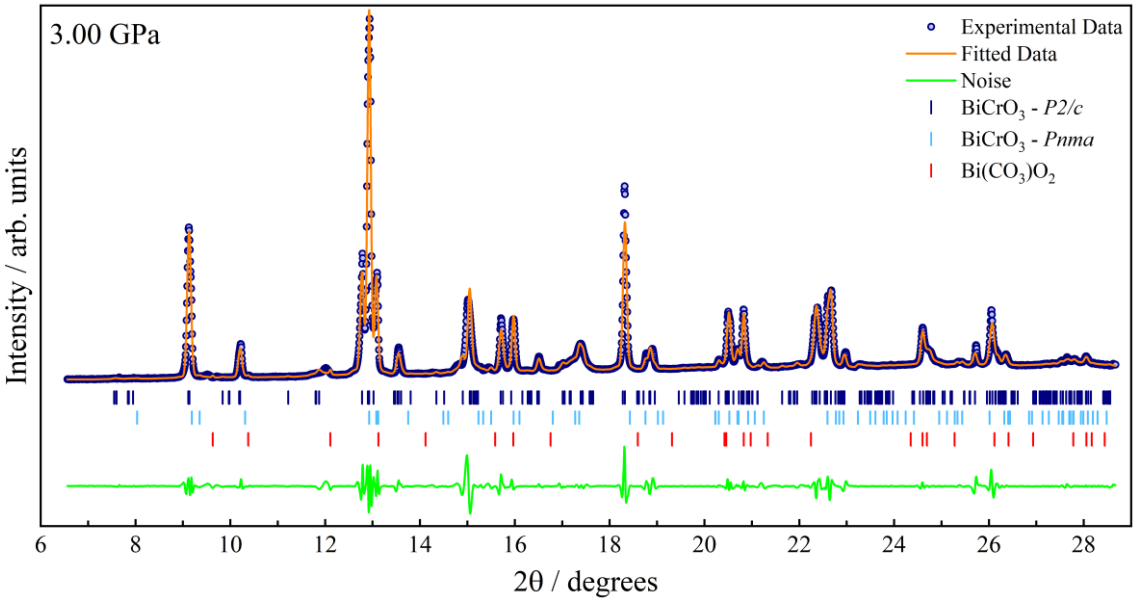

Figure 6.11. Lebail analysis of the SXRPD pattern of BCO at 3.00 GPa.

6.3 *$BiCrO_3$ Conclusions*

The perovskite $BiCrO_3$ was synthesized through a solid state reaction under HPHT conditions. XRPD analyses confirm the formation of BCO monoclinic with a minor amount of impurities originated from the adopted synthesis method. After the confirmation of the compound formation, the magnetic properties of BCO samples were investigated to confirm the magnetic transitions reported in the literature. From these analyses, we clear observed two magnetic transitions at 110 K and 80 K, related to rising of G-type AFM ordering and the spin reorientation, respectively and the first derivate of magnetic susceptibility revealed the existence of a slight magnetic event around 40 K.

The temperature dependent Raman measurements below room temperature revealed renormalizations effects in the energy of BCO phonons. The anomalies observed in frequencies and FWHM of $A_g(1)$, $A_g(3)$, $B_g(2)$ and $A_g(6)$ phonons start at 110 K, coinciding with the emergence of a G-type antiferromagnetic ordered structure and indicating that the observed effects are given by a spin-phonon coupling. On the other hand, the $B_g(1)$ and $A_g(4)$ phonons presented similar effects just below 80 K. These features suggest that some phonons are sensitive to the coupling between the magnetic and lattice phonons at the beginning of magnetically ordered phases, whereas others only expect this coupling only after the spin reorientation. The $\Delta\omega$ vs $(M(T)/M_0)^2$ plots confirmed the linearity between these magnitudes below 110 K or 80 K, depending on the observed phonon. In addition, these analyzes revealed that all spin-coupled phonons are sensitive to the spin reorientation reported around 80 K, which is also evidenced by changes in the slope of this linear behavior in the modes in which the coupling start at 110K.

No anomaly was observed at 165 K, which should be related with the magnetic ordering of the orthorhombic BCO impurity, suggesting that there is not coupling with the phonon lattice, or this effect is very weak. Conversely, a quite subtle change in the phonon frequency below 40 K suggests their dependence with the low temperature magnetic phenomenon of the orthorhombic phase.

The pressure dependent structural behavior of BCO presented slight changes in the diffraction patterns between 2.00 and 3.00 GPa, where initial analysis revealed a possible transition from the monoclinic *C2/c* to a monoclinic *P2/c* space group.

7. CONCLUSIONS

The solid state-reaction under High-Pressure and High-Temperature synthesis technique proved to be a powerful tool to produce compounds presenting interesting features, which could not be reached through conventional methods. The different synthesis conditions, based on the slight variations in pressure and temperature parameters adopted by different synthesis routes, revealed the crucial role of these thermodynamic parameters in the process to obtain good samples. The samples synthesized in this study presented interesting multiferroic properties, reflected in distinctive coupling effects between the magnetic ordering and lattice.

In the case of the melanothallite Cu_2OCl_2, we were able to report a spin-phonon coupling characterized by the renormalization of the phonon frequency and FWHM in three vibrational modes located at 186, 510 and 545 cm^{-1}. These effects start below 68 K, that corresponds to the temperature at which the magnetic ordering rising. The phonons harden below the magnetic transition due to spin-phonon coupling are in accordance with the empiric observations for antiferromagnetically ordered compounds. Despite the incommensurate spiral magnetic structure, the observed coupling behavior is similar to those observed in the stretching phonons of perovskites. The $\Delta\omega$ vs $(M(T)/M_0)^2$ plots showed that the renormalization of phonon frequencies follows the mean field approach, initially proposed for perovskite compounds. These findings suggest that the renormalizations due to the spin-phonon coupling depends only on the spin-phonon interactions and not on the phonon symmetry.

The $PbMn_7O_{12}$ Raman spectrum was investigated below room temperature and revealed renormalization effects of phonons frequencies below 80 K. These renormalizations are probably due to coupling between the spin moments and the lattice phonons. However, the temperature dependent phonons positions still presented high dispersion mainly at higher temperatures making difficult a precise analysis of these effects. This experiment will be repeated. The pressure-dependent behavior of $PbMn_7O_{12}$ structure also was investigated through Synchrotron X-ray diffraction measurements where initial Lebail analysis revealed possible structural phase transitions around 8.5, 14 and 19 GPa. However, deeper investigations through Rietveld Refinement are needed to confirm these transitions.

For the orthorhombic $TmMnO_3$ compound, we were able to report the room temperature Raman spectrum, where 13 vibrational modes were observed and assigned based on other o-RMO family compounds. The temperature dependence of Raman spectra of *o*-TMO below room temperature revealed renormalization effects on the frequency and FWHM parameters of $A_g(4)$, $A_g(3)$ and the $B_{2g}(1)$ phonons, which are related to MnO_6 vibrational motions. These effects were observed below 48 K where the incommensurate AFM ordered phase rises. However, the $\Delta\omega$ vs $(M(T)/M_0)^2$ analysis showed that in the G-type ordered phase (below 32 K) the renormalization effects become null indicating that there is no coupling at this magnetic ordered phase. These features indicate that this compound exhibit a spin-phonon coupling at the incommensurate magnetic ordered in contradiction to previous reports, which assumed that no coupling should be observed in the incommensurate phase of this family of compound. The low magnitude of the phonon frequency renormalization indicates the spin-phonon coupling in *o*-$TmMnO_3$ is weaker when compared to the values reported for its hexagonal phase and other *o*-RMO compounds with an A-type AFM phase, but still comparable with another compounds of o-RMO family, as $DyMnO_3$.

The monoclinic $BiCrO_3$ Raman spectrum was monitored below room temperature revealing hardening and softening effects on frequencies of the $A_g(1)$, $A_g(3)$, $B_g(2)$ and $A_g(6)$ phonons starting at 110 K. This temperature coincides with the emergence of a G-type antiferromagnetic ordered structure indicating that a spin-phonon coupling induces the observed phonon renormalizations. On the other hand, the $B_g(1)$ and $A_g(4)$ phonons also presented renormalization effects, but only below 80 K, indicating that these phonons expect the coupling just in the spin realigned phase under 80 K. The coupling behavior observed in all modes is similar to those reported in the stretching phonons in other perovskites, whose phonon renormalization follows a mean field behavior. Moreover, the $\Delta\omega$ vs $(M(T)/M_0)^2$ analysis showed that the $A_g(1)$, $A_g(3)$, $B_g(2)$ and $A_g(6)$ phonons also are sensitive to the spin realignment at 80 K, indicating that all spin-coupled phonons are influenced by the magnetic event at 80 K. No anomaly was observed at 165 K, which reveals that, if there is a magnetic ordering due to orthorhombic sublattice at this temperature, it does not couple with the phonon lattice. Finally, subtle changes in the phonon frequency below 40 K suggests a low temperature magnetic phenomenon. The pressure-dependent behavior of $BiCrO_3$ structure was also investigated through synchrotron X-ray diffraction measurements, where initial Lebail analysis revealed a

possible structural transition from C2/c to a P*2/c* space group occurring between 2.00 and 3.00 GPa. However, deeper investigations through Lebail or Rietveld Refinement are needed to confirm this conclusion.

Based multiferroic properties presented by the proposed materials, all synthesized samples presented coupling effects between the spins moments and the lattice phonons, recognized by renormalization of such phonon frequencies. These observations showed that each magnetic effect has a particular influence on spin-phonon coupling observed for each analyzed sample, which is reflected in the temperature dependent behavior of the lattice phonons, revealing interesting features about the multiferroic behavior of studied samples as the origin of magnetic orderings and changes in their magnetic structures. In this way, the spin-phonon coupling analysis through Raman spectroscopy can be seen as a fast and particle technique to improve the understanding of magnetoelectric multiferroic behavior and their coupling effect as well as to determine possible magnetic transitions through additional changes in this coupling behavior.

8. REFERENCES

[1] M. Mostovoy, Multiferroics: A whirlwind of opportunities, **Nature Materials**. 9 (**2010**) 188–190.

[2] K. Dörr, A. Herklotz, Materials science: Two steps for a magnetoelectric switch, **Nature**. 516 (**2014**) 337–338.

[3] J.F. Scott, Searching for new ferroelectrics and multiferroics: A user's point of view, **Npj Computational Materials**. 1 (**2015**) 15006.

[4] M.M. Vopson, Fundamentals of Multiferroic Materials and Their Possible Applications, **Critical Reviews in Solid State and Materials Sciences**. 40 (**2015**) 223–250.

[5] S. Dong, J.-M. Liu, S.-W. Cheong, Z. Ren, Multiferroic materials and magnetoelectric physics: symmetry, entanglement, excitation, and topology, **Advances in Physics**. 64 (**2015**) 519–626.

[6] N. Spaldin, Magnetic Materials: fundamentals and applications, Cambridge University Press, **2010**.

[7] P. Curie, Sur la symétrie dans les phénomènes physiques, symétrie d'un champ électrique et d'un champ magnétique, **Journal de Physique Théorique et Appliquée**. 3 (**1894**) 393–415.

[8] W.C. Röntgen, Über die durch Bewegung eines im homogenen elektrischen Felde befindlichen Dielectrikums hervorgerufene elektrodynamische Kraft, **Annalen Der Physik**. 271 (**1888**) 264–270.

[9] P. Debye, Remark on some new experiments on a magneto-electric straightening effect, **Journal of Physics**. 36 (**1926**) 300–301.

[10] H. Schmid, Multi-ferroic magnetoelectrics, **Ferroelectrics**. 162 (**1994**) 317–338.

[11] L.W. Martin, S.P. Crane, Y.H. Chu, M.B. Holcomb, M. Gajek, M. Huijben, C.H. Yang, N. Balke, R. Ramesh, Multiferroics and magnetoelectrics: Thin films and nanostructures, **Journal of Physics Condensed Matter**. 20 (**2008**).

[12] W. Eerenstein, N.D. Mathur, J.F. Scott, J. F, Scott: Multiferroic and magnetoelectric materials, **Nature**. 442759 (**2006**) 759–765.

[13] J.M.D. Coey, Magnetism and Magnetic Materials, Cambridge University Press, Cambridge, **2010**.

[14] B.D. Cullity, C.D. Graham, Introduction to Magnetic Materials, 2nd ed., Wiley, New Jersey, **2008**.

[15] A.N.L. de A. Silva, Síntese e caracterização de perovskitas quádruplas multiferróicas, Universidade Federal do Maranhão, **2015**.

[16] M. Fiebig, T. Lottermoser, D. Meier, M. Trassin, The evolution of multiferroics, **Nature Reviews Materials**. 1 (**2016**) 16046.

[17] D. Khomskii, Classifying multiferroics: Mechanisms and effects, **Physics**. 2 (**2009**) 20.

[18] B.B. Van Aken, T.T.M. Palstra, A. Filippetti, N.A. Spaldin, The origin of ferroelectricity in magnetoelectric $YMnO_3$, **Nature Materials**. 3 (**2004**) 164–170.

[19] M. Fiebig, Revival of the magnetoelectric effect, **Journal of Physics D: Applied Physics**. 38 (**2005**) R123–R152.

[20] R. Ramesh, N. a Spaldin, Multiferroics: progress and prospects in thin films, **Nature Materials**. 6 (**2007**) 21–29.

[21] M.M. Vopson, Fundamentals of Multiferroic Materials and Their Possible Applications, **Critical Reviews in Solid State and Materials Sciences**. 40 (**2015**) 223–250.

[22] R. Ramesh, N.A. Spaldin, Multiferroics: progress and prospects in thin films, **Nature Materials**. 6 (**2007**) 21–29.

[23] P. Gupta, P. Poddar, Using Raman and dielectric spectroscopy to elucidate the spin phonon and magnetoelectric coupling in $DyCrO_3$ nanoplatelets, **RSC Advances**. 5 (**2015**) 10094–10101.

[24] R.X. da Silva, Síntese e Caracterização de Perovskitas Complexas Multiferróicas com estrutura dupla ordenada, Universidade Federal do Maranhão, **2015**.

[25] T.R. Hart, R.L. Aggarwal, B. Lax, Temperature Dependence of Raman Scattering in Silicon, **Physical Review B**. 1 (**1970**) 638–642.

[26] M. Balkanski, R.F. Wallis, E. Haro, Anharmonic effects in light scattering due to optical phonons in silicon, **Physical Review B**. 28 (**1983**) 1928–1934.

[27] E. Granado, A. García, J.A. Sanjurjo, C. Rettori, I. Torriani, F. Prado, R.D. Sánchez, A. Caneiro, S.B. Oseroff, Magnetic ordering effects in the Raman spectra of $La_{1-x}Mn_{1-x}O_3$, **Physical Review B**. 60 (**1999**) 11879–11882.

[28] W. Baltensperger, J.S. Helman, Influence of magnetic order in insulators on the optical phonon frequency, **Helvetica Physica Acta**. 41 (**1968**) 668–673.

[29] D.J. Lockwood, M.G. Cottam, The spin - phonon interaction in FeF_2 and MnF_2 studied by Raman spectroscopy, **J. Appl. Phys.** 64 (**1988**) 5876.

[30] W.S. Ferreira, J. Agostinho Moreira, A. Almeida, M.R. Chaves, J.P. Araújo, J.B.

Oliveira, J.M. MacHado Da Silva, M.A. Sá, T.M. Mendonça, P. Simeão Carvalho, J. Kreisel, J.L. Ribeiro, L.G. Vieira, P.B. Tavares, S. Mendonça, Spin-phonon coupling and magnetoelectric properties: EuMnO3 versus GdMnO3, **Physical Review B - Condensed Matter and Materials Physics**. 79 (**2009**) 1–10.

[31] M.A. Prosnikov, A.N. Smirnov, V.Y. Davydov, R. V. Pisarev, N.A. Lyubochko, S.N. Barilo, Magnetic dynamics and spin-phonon coupling in the antiferromagnet Ni_2NbBO_6, **Physical Review B**. 98 (**2018**) 104404.

[32] M.N. Iliev, M. V. Abrashev, J. Laverdière, S. Jandl, M.M. Gospodinov, Y.-Q. Wang, Y.-Y. Sun, Distortion-dependent Raman spectra and mode mixing in $RMnO_3$ perovskites (R=La, Pr, Nd, Sm, Eu, Gd, Tb, Dy, Ho, Y), **Physical Review B**. 73 (**2006**) 064302.

[33] Y. Sharma, S. Sahoo, W. Perez, S. Mukherjee, R. Gupta, A. Garg, R. Chatterjee, R.S. Katiyar, Phonons and magnetic excitation correlations in weak ferromagnetic $YCrO_3$, **Journal of Applied Physics**. 115 (**2014**) 0–9.

[34] S. Mansouri, S. Jandl, A. Mukhin, V.Y. Ivanov, A. Balbashov, A comparative Raman study between $PrMnO_3$, $NdMnO_3$, $TbMnO_3$ and $DyMnO_3$, **Scientific Reports**. 7 (**2017**) 13796.

[35] J. Vermette, S. Jandl, M.M. Gospodinov, Raman study of spin–phonon coupling in $ErMnO_3$, **Journal of Physics: Condensed Matter**. 20 (**2008**) 425219.

[36] M.N. Iliev, M. V. Abrashev, A.P. Litvinchuk, V.G. Hadjiev, H. Guo, A. Gupta, Raman spectroscopy of ordered double perovskite La_2CoMnO_6, **Physical Review B**. 75 (**2007**) 104118.

[37] M.N. Iliev, V.G. Hadjiev, A.P. Litvinchuk, F. Yen, Y.Q. Wang, Y.Y. Sun, S. Jandl, J. Laverdière, V.N. Popov, M.M. Gospodinov, Multiple-order Raman scattering from rare-earth manganites: Oxygen isotope and rare-earth substitution effects, **Physical Review B - Condensed Matter and Materials Physics**. 75 (**2007**) 4–8.

[38] R.B. Macedo Filho, A. Pedro Ayala, C. William de Araujo Paschoal, Spin-phonon coupling in Y_2NiMnO_6 double perovskite probed by Raman spectroscopy, **Applied Physics Letters**. 102 (**2013**) 192902.

[39] R.X. Silva, H. Reichlova, X. Marti, D.A.B. Barbosa, M.W. Lufaso, B.S. Araujo, A.P. Ayala, C.W.A. Paschoal, Spin-phonon coupling in $Gd(Co_{1/2}Mn_{1/2})O_3$ perovskite, **Journal of Applied Physics**. 114 (**2013**) 194102.

[40] S. Mahana, B. Rakshit, R. Basu, S. Dhara, B. Joseph, U. Manju, S.D. Mahanti, D. Topwal, Local inversion symmetry breaking and spin-phonon coupling in the

perovskite $GdCrO_3$, **Physical Review B**. 96 (**2017**) 1–9.

[41] M. El Amrani, M. Zaghrioui, V. Ta Phuoc, F. Gervais, N.E. Massa, Local symmetry breaking and spin-phonon coupling in $SmCrO_3$ orthochromite, **Journal of Magnetism and Magnetic Materials**. 361 (**2014**) 1–6.

[42] R.B. Macedo Filho, A. Pedro Ayala, C. William de Araujo Paschoal, Spin-phonon coupling in Y_2NiMnO_6 double perovskite probed by Raman spectroscopy, **Applied Physics Letters**. 102 (**2013**) 192902.

[43] M.N. Iliev, H. Guo, A. Gupta, Raman spectroscopy evidence of strong spin-phonon coupling in epitaxial thin films of the double perovskite La_2NiMnO_6, **Applied Physics Letters**. 90 (**2007**) 151914.

[44] P. Toulemonde, P. Bordet, P. Bouvier, J. Kreisel, Single-crystalline $BiMnO_3$ studied by temperature-dependent x-ray diffraction and Raman spectroscopy, **Physical Review B**. 89 (**2014**) 224107.

[45] E. Aytan, B. Debnath, F. Kargar, Y. Barlas, M.M. Lacerda, J.X. Li, R.K. Lake, J. Shi, A.A. Balandin, Spin-phonon coupling in antiferromagnetic nickel oxide, **Applied Physics Letters**. 111 (**2017**) 252402.

[46] R.B. Macedo Filho, D.A.B. Barbosa, H. Reichlova, X. Marti, A.S. De Menezes, A.P. Ayala, C.W.A. Paschoal, Role of rare-earth ionic radii on the spin-phonon coupling in multiferroic ordered double perovskites, **Materials Research Express**. 2 (**2015**) 75201.

[47] R.X. Silva, M.C. Castro Júnior, S. Yáñez-Vilar, M.S. Andújar, J. Mira, M.A. Señarís-Rodríguez, C.W.A. Paschoal, Spin-phonon coupling in multiferroic Y_2CoMnO_6, **Journal of Alloys and Compounds**. 690 (**2017**) 909–915.

[48] A.B. Sushkov, O. Tchernyshyov, W.R. II, S.W. Cheong, H.D. Drew, Probing Spin Correlations with Phonons in the Strongly Frustrated Magnet $ZnCr_2O_4$, **Physical Review Letters**. 94 (**2005**) 137202.

[49] J. Laverdière, S. Jandl, A.A. Mukhin, V.Y. Ivanov, V.G. Ivanov, M.N. Iliev, Spin-phonon coupling in orthorhombic $RMnO_3$ (R= Pr, Nd, Sm, Eu, Gd, Td, Dy Ho, Y): A Raman study, **Physical Review B**. 73 (**2006**) 214301.

[50] B.H. Toby, EXPGUI , a graphical user interface for GSAS, **Journal of Applied Crystallography**. 34 (**2001**) 210–213.

[51] A.C. Larson, R.B. Von Dreele, GSAS - General Structure Analysis System, (**2004**) 86–784.

[52] A.P. Hammersley, S.O. Svensson, M. Hanfland, A.N. Fitch, D. Hausermann, Two-

dimensional detector software: From real detector to idealised image or two-theta scan, **High Pressure Research**. 14 (**1996**) 235–248.

[53] C. Prescher, V.B. Prakapenka, DIOPTAS : a program for reduction of two-dimensional X-ray diffraction data and data exploration, **High Pressure Research**. 35 (**2015**) 223–230.

[54] A. Le Bail, H. Duroy, J.L. Fourquet, Ab-initio structure determination of LiSbWO6 by X-ray powder diffraction, **Materials Research Bulletin**. 23 (**1988**) 447–452.

[55] J. Rodríguez-Carvajal, Recent advances in magnetic structure determination by neutron powder diffraction, **Physica B: Condensed Matter**. 192 (**1993**) 55–69.

[56] M. Wojdyr, Fityk : a general-purpose peak fitting program, **Journal of Applied Crystallography**. 43 (**2010**) 1126–1128.

[57] R.C. Liebermann, Multi-anvil, high pressure apparatus: a half-century of development and progress, **High Pressure Research**. 31 (**2011**) 493–532.

[58] P.C. Burnley, The Multi-Anvil Apparatus, **Teaching Mineralogy: Topical Resources**. (**2016**).

[59] A. Jayaraman, Diamond anvil cell and high-pressure physical investigations, **Reviews of Modern Physics**. 55 (**1983**) 65–108.

[60] J.C. Chervin, B. Canny, J.M. Besson, P. Pruzan, A diamond anvil cell for IR microspectroscopy, **Review of Scientific Instruments**. 66 (**1995**) 2595–2598.

[61] T. Kato, E. Ohtani, H. Morishima, D. Yamazaki, A. Suzuki, M. Suto, T. Kikegawa, O. Shimomura, In situ x ray observation of high-pressure phase transitions of $MgSiO_3$, **Journal of Geophysical Research B: Solid Earth**. 100 (**1995**) 20,475-20,481.

[62] N. Kawai, S. Endo, The generation of ultrahigh hydrostatic pressures by a split sphere apparatus, **Review of Scientific Instruments**. 41 (**1970**) 1178–1181.

[63] D. Delmonte, Combined magnetic, electric, ferroelectric and magnetoeletric characterization of novel multiferroic perovskites obtanined by high pressure/temperature synthesis, Università degli studi di Parma, **2015**.

[64] J. Ma, J. Hu, Z. Li, C.W. Nan, Recent progress in multiferroic magnetoelectric composites: From bulk to thin films, **Advanced Materials**. 23 (**2011**) 1062–1087.

[65] F. Matsukura, Y. Tokura, H. Ohno, Control of magnetism by electric fields, **Nature Nanotechnology**. 10 (**2015**) 209–220.

[66] W. Eerenstein, N.D. Mathur, J.F. Scott, Multiferroic and magnetoelectric

materials, **Nature**. 442 (**2006**) 759–765.

[67] J.F. Scott, Data storage: Multiferroic memories, **Nature Materials**. 6 (**2007**) 256–257.

[68] I. Žutić, J. Fabian, S. Das Sarma, Spintronics: Fundamentals and applications, **Reviews of Modern Physics**. 76 (**2004**) 323–410.

[69] M. Sánchez-Andújar, S. Yáñez-Vilar, N. Biskup, S. Castro-García, J. Mira, J. Rivas, M.A. Señarís-Rodríguez, Magnetoelectric behavior in the complex CaMn7O12 perovskite, **Journal of Magnetism and Magnetic Materials**. 321 (**2009**) 1739–1742.

[70] T. Kimura, T. Goto, H. Shintani, K. Ishizaka, T. Arima, Y. Tokura, Magnetic control of ferroelectric polarization, **Nature**. 426 (**2003**) 55–58.

[71] M. Kenzelmann, A.B. Harris, S. Jonas, C. Broholm, J. Schefer, S.B. Kim, C.L. Zhang, S.-W. Cheong, O.P. Vajk, J.W. Lynn, Magnetic Inversion Symmetry Breaking and Ferroelectricity in $TbMnO_3$, **Physical Review Letters**. 95 (**2005**) 087206.

[72] N. Hur, S. Park, P.A. Sharma, J.S. Ahn, S. Guha, S.-W. Cheong, Electric polarization reversal and memory in a multiferroic material induced by magnetic fields, **Nature**. 429 (**2004**) 392–395.

[73] L. Zhao, M.T. Fernandez-Diaz, L.H. Tjeng, A.C. Komarek, Oxyhalides: A new class of high-TC multiferroic materials, **Science Advances**. 2 (**2016**) e1600353–e1600353.

[74] S. V. Krivovichev, S.K. Filatov, P.C. Burns, THE CUPRITE-LIKE FRAMEWORK OF OCu4 TETRAHEDRA IN THE CRYSTAL STRUCTURE OF SYNTHETIC MELANOTHALLITE, Cu_2OCl_2, AND ITS NEGATIVE THERMAL EXPANSION, **The Canadian Mineralogist**. 40 (**2002**) 1185–1190.

[75] H. Okabe, K. Suzuki, K. Kawashima, T. Muranaka, J. Akimitsu, New Pyrochlore-like Compound Cu_2OCl_2 with S=1/2, **Journal of the Physical Society of Japan**. 75 (**2006**) 123705.

[76] A. Junod, D. Eckert, G. Triscone, J. M ller, W. Reichardt, A study of the magnetic transitions in CuO: specific heat (1-330 K), magnetic susceptibility and phonon density of states, **Journal of Physics: Condensed Matter**. 1 (**1989**) 8021–8034.

[77] P.J. Brown, T. Chattopadhyay, J.B. Forsyth, V. Nunez, Antiferromagnetism in CuO studied by neutron polarimetry, **Journal of Physics: Condensed Matter**. 3 (**1991**) 4281–4287.

[78] T. Kimura, Y. Sekio, H. Nakamura, T. Siegrist, a P. Ramirez, Cupric oxide as an induced-multiferroic with high-TC, **Nature Materials**. 7 (**2008**) 291–294.

[79] M. Hase, I. Terasaki, K. Uchinokura, Observation of the spin-Peierls transition in linear Cu^{2+} (spin-1/2) chains in an inorganic compound, **Physical Review Letters**. 70 (**1993**) 3651–3654.

[80] A. Seidel, C.A. Marianetti, F.C. Chou, G. Ceder, P.A. Lee, S=1/2 chains and spin-Peierls transition in TiOCl, **Physical Review B**. 67 (**2003**) 020405.

[81] J.N. McElearney, S. Merchant, R.L. Carlin, Isotropic magnetic exchange in magnesium dichloride dihydrate, $MnCl_2.2H_2O$, a chemical linear chain, **Inorganic Chemistry**. 12 (**1973**) 906–908.

[82] W.E. Hatfield, New magnetic and structural results for uniformly spaced, alternatingly spaced, and ladder-like copper (II) linear chain compounds (invited), **Journal of Applied Physics**. 52 (**1981**) 1985–1990.

[83] D.L. Rousseau, R.P. Bauman, S.P.S. Porto, Normal mode determination in crystals, **Journal of Raman Spectroscopy**. 10 (**1981**) 253–290.

[84] H. Hagemann, H. Bill, W. Sadowski, E. Walker, M. François, Raman spectra of single crystal CuO, **Solid State Communications**. 73 (**1990**) 447–451.

[85] J.F. Xu, W. Ji, Z.X. Shen, S.H. Tang, X.R. Ye, D.Z. Jia, X.Q. Xin, Preparation and Characterization of CuO Nanocrystals, **Journal of Solid State Chemistry**. 147 (**1999**) 516–519.

[86] J.F. Xu, W. Ji, Z.X. Shen, W.S. Li, S.H. Tang, X.R. Ye, D.Z. Jia, X.Q. Xin, Raman spectra of CuO nanocrystals, **Journal of Raman Spectroscopy**. 30 (**1999**) 413–415.

[87] K. Reimann, K. Syassen, Pressure dependence of Raman modes in CuO, **Solid State Communications**. 76 (**1990**) 137–140.

[88] X.K. Chen, J.C. Irwin, J.P. Franck, Evidence for a strong spin-phonon interaction in cupric oxide, **Physical Review B**. 52 (**1995**) R13130–R13133.

[89] H.-M. Eiter, P. Jaschke, R. Hackl, A. Bauer, M. Gangl, C. Pfleiderer, Raman study of the temperature and magnetic-field dependence of the electronic and lattice properties of MnSi, **Physical Review B**. 90 (**2014**) 024411.

[90] T. Kimura, S. Ishihara, H. Shintani, T. Arima, K.T. Takahashi, K. Ishizaka, Y. Tokura, Distorted perovskite with e_g^1 configuration as a frustrated spin system, **Physical Review B**. 68 (**2003**) 060403.

[91] A.N. Vasil'ev, O.S. Volkova, New functional materials $AC_3B_4O_{12}$ (Review), **Low**

Temperature Physics. 33 (**2007**) 895–914.

[92] S. Yagi, I. Yamada, H. Tsukasaki, A. Seno, M. Murakami, H. Fujii, H. Chen, N. Umezawa, H. Abe, N. Nishiyama, S. Mori, Covalency-reinforced oxygen evolution reaction catalyst, **Nature Communications**. 6 (**2015**) 8249.

[93] M. Marezio, P.D. Dernier, J. Chenavas, J.C. Joubert, High pressure synthesis and crystal structure of $NaMn_7O_{12}$, **Journal of Solid State Chemistry**. 6 (**1973**) 16–20.

[94] B. Bochu, J. Chenavas, J. Joubert, M. Marezio, High pressure synthesis and crystal structure of a new series of perovskite-like compounds CMn_7O_{12}(C= Na, Ca, Cd, Sr, La, Nd), **Journal of Solid State Chemistry**. 11 (**1974**) 88–93.

[95] R.D. Johnson, L.C. Chapon, D.D. Khalyavin, P. Manuel, P.G. Radaelli, C. Martin, Giant improper ferroelectricity in the ferroaxial magnet $CaMn_7O_{12}$, **Physical Review Letters**. 108 (**2012**) 2–5.

[96] F. Mezzadri, G. Calestani, M. Calicchio, E. Gilioli, F. Bolzoni, R. Cabassi, M. Marezio, A. Migliori, Synthesis and characterization of multiferroic $BiMn_7O_{12}$, **Physical Review B**. 79 (**2009**).

[97] A.A. Belik, Y.S. Glazkova, N. Terada, Y. Matsushita, A. V. Sobolev, I.A. Presniakov, N. Tsujii, S. Nimori, K. Takehana, Y. Imanaka, Spin-Driven Multiferroic Properties of $PbMn_7O_{12}$ Perovskite, **Inorganic Chemistry**. 55 (**2016**) 6169–6177.

[98] T. Locherer, R. Dinnebier, R.K. Kremer, M. Greenblatt, M. Jansen, Synthesis and properties of a new quadruple perovskite: A-site ordered $PbMn_3Mn_4O_{12}$, **Journal of Solid State Chemistry**. 190 (**2012**) 277–284.

[99] F. Sugawara, S. Iida, Y. Syono, S. Akimoto, New Magnetic Perovskites $BiMnO_3$ and $BiCrO_3$, **Journal of the Physical Society of Japan**. 20 (**1965**) 1529–1529.

[100] F. Sugawara, S. Iiida, Y. Syono, S. Akimoto, Magnetic Properties and Crystal Distortions of $BiMnO_3$ and $BiCrO_3$, **Journal of the Physical Society of Japan**. 25 (**1968**) 1553–1558.

[101] S. Niitaka, M. Azuma, M. Takano, E. Nishibori, M. Takata, M. Sakata, Crystal structure and dielectric and magnetic properties of $BiCrO_3$ as a ferroelectromagnet, **Solid State Ionics**. 172 (**2004**) 557–559.

[102] A. Nonato, B.S. Araujo, A.P. Ayala, A.P. Maciel, S. Yanez-Vilar, M. Sanchez-Andujar, M.A. Senaris-Rodriguez, C.W.A. Paschoal, Spin-phonon and magnetostriction phenomena in $CaMn_7O_{12}$ helimagnet probed by Raman

spectroscopy, **Applied Physics Letters**. 105 (**2014**) 1–5.

[103] A.A. Belik, Y.S. Glazkova, Y. Katsuya, M. Tanaka, A. V. Sobolev, I.A. Presniakov, Low-Temperature Structural Modulations in $CdMn_7O_{12}$, $CaMn_7O_{12}$, $SrMn_7O_{12}$, and $PbMn_7O_{12}$ Perovskites Studied by Synchrotron X-ray Powder Diffraction and Mös, **The Journal of Physical Chemistry C**. 120 (**2016**) 8278–8288.

[104] H.Y. Hwang, S.-W. Cheong, P.G. Radaelli, M. Marezio, B. Batlogg, Lattice Effects on the Magnetoresistance in Doped $LaMnO_3$, **Physical Review Letters**. 75 (**1995**) 914–917.

[105] T. Goto, T. Kimura, G. Lawes, A.P. Ramirez, Y. Tokura, Ferroelectricity and Giant Magnetocapacitance in Perovskite Rare-Earth Manganites, **Physical Review Letters**. 92 (**2004**) 257201.

[106] E. Baldini, T. Kubacka, B.P.P. Mallett, C. Ma, S.M. Koohpayeh, Y. Zhu, C. Bernhard, S.L. Johnson, F. Carbone, Lattice-mediated magnetic order melting in TbMnO3, **Physical Review B**. 97 (**2018**) 125149.

[107] L. Martín-Carrón, A. De Andrés, M.J. Martínez-Lope, M.T. Casais, J.A. Alonso, Raman phonons and light scattering in $RMnO_3$ (R=La, Pr, Nd, Ho, Er Tb and Y) orthorhombic and hexagonal manganites, **Journal of Alloys and Compounds**. 323–324 (**2001**) 494–497.

[108] J.-S. Zhou, J.B. Goodenough, J.M. Gallardo-Amores, E. Morán, M.A. Alario-Franco, R. Caudillo, Hexagonal versus perovskite phase of manganite (R=Y, Ho, Er, Tm, Yb, Lu), **Physical Review B**. 74 (**2006**) 014422.

[109] H.A. Salama, G.A. Stewart, W.D. Hutchison, K. Nishimura, D.R. Scott, H.S.C. O'Neill, A 169Tm-Mössbauer spectroscopy investigation of orthorhombic phase o - $TmMnO_3$, **Solid State Communications**. 150 (**2010**) 289–291.

[110] K. Uusi-Esko, J. Malm, N. Imamura, H. Yamauchi, M. Karppinen, Characterization of $RMnO_3$ (R = Sc, Y, Dy-Lu): High-pressure synthesized metastable perovskites and their hexagonal precursor phases, **Materials Chemistry and Physics**. 112 (**2008**) 1029–1034.

[111] L.J. Wang, S.M. Feng, J.L. Zhu, R.C. Yu, C.Q. Jin, W. Yu, X.H. Wang, L.T. Li, Ferroelectricity of multiferroic hexagonal $TmMnO_3$ ceramics synthesized under high pressure, **Applied Physics Letters**. 91 (**2007**) 172502.

[112] F. Yen, C. dela Cruz, B. Lorenz, E. Galstyan, Y.Y. Sun, M. Gospodinov, C.W. Chu, Magnetic phase diagrams of multiferroic hexagonal $RMnO_3$ (R = Er, Yb,

Tm, and Ho), **Journal of Materials Research**. 22 (**2007**) 2163–2173.

[113] N.E. Massa, L. Del Campo, D.D.S. Meneses, P. Echegut, M.J. Martínez-Lope, J.A. Alonso, Phonons and hybrid modes in the high and low temperature far infrared dynamics of hexagonal $TmMnO_3$., **Journal of Physics. Condensed Matter : An Institute of Physics Journal**. 26 (**2014**) 275901.

[114] M. Tachibana, T. Shimoyama, H. Kawaji, T. Atake, E. Takayama-Muromachi, Jahn-Teller distortion and magnetic transitions in perovskite $RMnO_3$ (R=Ho, Er, Tm, Yb, and Lu), **Physical Review B - Condensed Matter and Materials Physics**. 75 (**2007**) 2–6.

[115] V.Y. Pomjakushin, M. Kenzelmann, A. Dönni, A.B. Harris, T. Nakajima, S. Mitsuda, M. Tachibana, L. Keller, J. Mesot, H. Kitazawa, E. Takayama-Muromachi, Evidence for large electric polarization from collinear magnetism in $TmMnO_3$, **New Journal of Physics**. 11 (**2009**).

[116] T.C. Han, H.H. Chao, Observation of large electric polarization in orthorhombic $TmMnO_3$ thin films, **Applied Physics Letters**. 97 (**2010**).

[117] M. Garganourakis, Y. Bodenthin, R.A. De Souza, V. Scagnoli, A. Dönni, M. Tachibana, H. Kitazawa, E. Takayama-Muromachi, U. Staub, Magnetic and electronic orderings in orthorhombic $RMnO_3$ (R=Tm, Lu) studied by resonant soft x-ray powder diffraction, **Physical Review B - Condensed Matter and Materials Physics**. 86 (**2012**) 1–5.

[118] Y.W. Windsor, M. Ramakrishnan, L. Rettig, A. Alberca, E.M. Bothschafter, U. Staub, K. Shimamoto, Y. Hu, T. Lippert, C.W. Schneider, Interplay between magnetic order at Mn and Tm sites alongside the structural distortion in multiferroic films of o−$TmMnO_3$, **Physical Review B**. 91 (**2015**) 235144.

[119] K. Shimamoto, S. Mukherjee, N.S. Bingham, A.K. Suszka, T. Lippert, C. Niedermayer, C.W. Schneider, Single-axis-dependent structural and multiferroic properties of orthorhombic $RMnO_3$ (R=Gd-Lu), **Physical Review B**. 95 (**2017**) 1–9.

[120] R. Basistyy, T.N. Stanislavchuk, A.A. Sirenko, A.P. Litvinchuk, M. Kotelyanskii, G.L. Carr, N. Lee, X. Wang, S.W. Cheong, Infrared-active optical phonons and magnetic excitations in the hexagonal manganites $RMnO_3$ (R=Ho, Er, Tm, Yb, and Lu), **Physical Review B - Condensed Matter and Materials Physics**. 90 (**2014**) 1–12.

[121] K. Yoshii, H. Abe, Magnetic Properties of $LnMnO_3$ (Ln=Ho, Er, Tm, Yb, and Lu),

Journal of Solid State Chemistry. 165 (**2002**) 131–135.

[122] A. De Andrés, J.L. Martínez, J.M. Alonso, E. Herrero, C. Prieto, J.A. Alonso, F. Agulló, M. García-Hernández, Raman phonons in orthorhombic manganites, **Journal of Magnetism and Magnetic Materials**. 196 (**1999**) 453–454.

[123] M.N. Iliev, M. V. Abrashev, J. Laverdière, S. Jandl, M.M. Gospodinov, Y.-Q. Wang, Y.-Y. Sun, Distortion-dependent Raman spectra and mode mixing in $RMnO_3$ perovskites (R=La, Pr, **Physical Review B**. 73 (**2006**) 064302.

[124] L. Martín-Carrón, A. De Andrés, M.J. Martínez-Lope, M.T. Casais, J.A. Alonso, Raman phonons as a probe of disorder, fluctuations, and local structure in doped and undoped orthorhombic and rhombohedral manganites, **Physical Review B - Condensed Matter and Materials Physics**. 66 (**2002**) 1–8.

[125] E. Granado, A. Garcia, J. Sanjurjo, C. Rettori, I. Torriani, E. Prado, R. Sanchez, A. Canerio, S. Oseroff, Magnetic ordering effects in the Raman spectra of $La_{1-x}Mn_{1-x}O_3$, **Phys. Rev. B**. 60 (**1999**) 11879.

[126] B. Rajeswaran, D.I. Khomskii, A.K. Zvezdin, C.N.R. Rao, A. Sundaresan, Field-induced polar order at the Néel temperature of chromium in rare-earth orthochromites: Interplay of rare-earth and Cr magnetism, **Physical Review B**. 86 (**2012**) 214409.

[127] H.J. Zhao, J. Íñiguez, X.M. Chen, L. Bellaiche, Origin of the magnetization and compensation temperature in rare-earth orthoferrites and orthochromates, **Physical Review B**. 93 (**2016**) 014417.

[128] H.J. Zhao, L. Bellaiche, X.M. Chen, J. Íñiguez, Improper electric polarization in simple perovskite oxides with two magnetic sublattices, **Nature Communications**. 8 (**2017**) 14025.

[129] J.R. Sahu, C.R. Serrao, N. Ray, U. V. Waghmare, C.N.R. Rao, Rare earth chromites: a new family of multiferroics, **J. Mater. Chem.** 17 (**2007**) 42–44.

[130] M. Murakami, S. Fujino, S.-H. Lim, C.J. Long, L.G. Salamanca-Riba, M. Wuttig, I. Takeuchi, V. Nagarajan, A. Varatharajan, Fabrication of multiferroic epitaxial $BiCrO_3$ thin films, **Applied Physics Letters**. 88 (**2006**) 152902.

[131] R. V. William, A. Marikani, D. Madhavan, Effect of annealing process on dielectric and multiferroic properties of Sol-Gel derived bismuth chromate thin films, **Ferroelectrics Letters Section**. 44 (**2017**) 18–28.

[132] J. Ding, X.-B. Kang, L.-W. Wen, H.-D. Li, J.-M. Zhang, Magnetic and Ferroelectric Properties of $BiCrO_3$ from First-Principles Calculations, **Chinese**

Physics Letters. 31 (**2014**) 107501.

[133] A. a Belik, E. Takayama-Muromachi, On magnetic properties of $BiCrO_3$ and $BiMnO_3$, **Journal of Physics: Conference Series**. 165 (**2009**) 012035.

[134] A.A. Belik, Polar and nonpolar phases of BiMO3: A review, **Journal of Solid State Chemistry**. 195 (**2012**) 32–40.

[135] C. Darie, C. Goujon, M. Bacia, H. Klein, P. Toulemonde, P. Bordet, E. Suard, Magnetic and crystal structures of $BiCrO_3$, **Solid State Sciences**. 12 (**2010**) 660–664.

[136] N.A. Hill, P. Bättig, C. Daul, First principles search for multiferroism in $BiCrO_3$, **Journal of Physical Chemistry B**. 106 (**2002**) 3383–3388.

[137] D.H. Kim, H.N. Lee, M. Varela, H.M. Christen, Antiferroelectricity in multiferroic BiCrO3 epitaxial films, **Applied Physics Letters**. 89 (**2006**) 162904.

[138] C. Himcinschi, I. Vrejoiu, T. Weißbach, K. Vijayanandhini, A. Talkenberger, C. Röder, S. Bahmann, D.R.T. Zahn, A.A. Belik, D. Rafaja, J. Kortus, Raman spectra and dielectric function of BiCrO3: Experimental and first-principles studies, **Journal of Applied Physics**. 110 (**2011**).

[139] A.A. Belik, S. Iikubo, K. Kodama, N. Igawa, S. Shamoto, E. Takayama-Muromachi, Neutron Powder Diffraction Study on the Crystal and Magnetic Structures of BiCrO 3, **Chemistry of Materials**. 20 (**2008**) 3765–3769.

[140] A.A. Belik, N. Tsujii, H. Suzuki, E. Takayama-muromachi, Q.B. Center, Magnetic Properties of Bulk $BiCrO_3$ Studied with dc and ac Magnetization and Specific Heat, **Inorganic Chemistry**. 46 (**2007**) 8746–8751.

[141] C. Goujon, C. Darie, M. Bacia, H. Klein, L. Ortega, P. Bordet, High pressure synthesis of $BiCrO_3$, a candidate for multiferroism, **Journal of Physics: Conference Series**. 121 (**2008**) 022009.

[142] A.M. Glazer, The classification of tilted octahedra in perovskites, **Acta Crystallographica Section B Structural Crystallography and Crystal Chemistry**. 28 (**1972**) 3384–3392.

[143] A.A. Belik, E. Takayama-Muromachi, On magnetic properties of $BiCrO_3$ and $BiMnO_3$, **Journal of Physics: Conference Series**. 165 (**2009**) 012035.

[144] P.W. Anderson, Generalizations of the Weiss Molecular Field Theory of Antiferromagnetism, **Physical Review**. 79 (**1950**) 705–710.

[145] A.A. Belik, N. Tsujii, H. Suzuki, E. Takayama-muromachi, Q.B. Center, Magnetic Properties of Bulk $BiCrO_3$ Studied with dc and ac Magnetization and Specific

Heat, **Inorganic Chemistry**. 46 (**2007**) 8746–8751.

[146] K. Tsushima, K. Aoyagi, S. Sugano, Magnetic and Magneto-Optical Properties of Some Rare-Earth and Yttrium Orthochromites, **Journal of Applied Physics**. 41 (**1970**) 1238–1240.

[147] M. Tripathi, R.J. Choudhary, D.M. Phase, T. Chatterji, H.E. Fischer, Evolution of magnetic phases in $SmCrO_3$: A neutron diffraction and magnetometric study, **Phys. Rev. B**. 96 (**2017**) 174421.

[148] M.C. Weber, J. Kreisel, P.A. Thomas, M. Newton, K. Sardar, R.I. Walton, Phonon Raman scattering of $RCrO_3$ perovskites (R=Y, La, Pr, Sm, Gd, Dy, Ho, Yb, Lu), **Physical Review B - Condensed Matter and Materials Physics**. 85 (**2012**) 1–9.

[149] M.N. Iliev, A.P. Litvinchuk, V.G. Hadjiev, Y.-Q. Wang, J. Cmaidalka, R.-L. Meng, Y.-Y. Sun, N. Kolev, M. V. Abrashev, Raman spectroscopy of low-temperature (Pnma) and high-temperature (R-3c) phases of $LaCrO_3$, **Physical Review B**. 74 (**2006**) 214301.

[150] M.N. Iliev, M. V. Abrashev, J. Laverdière, S. Jandl, M.M. Gospodinov, Y.-Q. Wang, Y.-Y. Sun, Distortion-dependent Raman spectra and mode mixing in $RMnO_3$ perovskites (R=La, P), **Physical Review B**. 73 (**2006**) 064302.

[151] N.D. Todorov, M. V. Abrashev, V.G. Ivanov, G.G. Tsutsumanova, V. Marinova, Y.-Q. Wang, M.N. Iliev, Comparative Raman study of isostructural $YCrO_3$ and $YMnO_3$: Effect, **Physical Review B**. 83 (**2011**) 224303.

[152] D.P. Kozlenko, N.T. Dang, S.H. Jabarov, A.A. Belik, S.E. Kichanov, E. V. Lukin, C. Lathe, L.S. Dubrovinsky, V.Y. Kazimirov, M.B. Smirnov, B.N. Savenko, A.I. Mammadov, E. Takayama-Muromachi, L.H. Khiem, Structural polymorphism in multiferroic $BiMnO_3$ at high pressures and temperatures, **Journal of Alloys and Compounds**. 585 (**2014**) 741–747.

[153] A. Talkenberger, C. Himcinschi, T. Weißbach, K. Vijayanandhini, I. Vrejoiu, C. Röder, D. Rafaja, J. Kortus, Raman spectroscopic and X-ray diffraction investigations of epitaxial $BiCrO_3$ thin films, **Thin Solid Films**. 520 (**2012**) 4590–4594.

[154] A. Nonato, B.S. Araujo, A.P. Ayala, A.P. Maciel, S. Yanez-Vilar, M. Sanchez-Andujar, M.A. Senaris-Rodriguez, C.W.A. Paschoal, Spin-phonon and magnetostriction phenomena in $CaMn_7O_{12}$ helimagnet probed by Raman spectroscopy, **Applied Physics Letters**. 105 (**2014**) 222902.

[155] V. Srinu Bhadram, B. Rajeswaran, A. Sundaresan, C. Narayana, Spin-phonon

coupling in multiferroic $RCrO_3$ (R-Y, Lu, Gd, Eu, Sm): A Raman study, **EPL (Europhysics Letters)**. 101 (**2013**) 17008.

[156] P. Toulemonde, P. Bordet, P. Bouvier, J. Kreisel, Single-crystalline $BiMnO_3$ studied by temperature-dependent x-ray diffraction and Raman spectroscopy, **Physical Review B**. 89 (**2014**) 224107.

[157] K. Wakamura, T. Arai, Effect of magnetic ordering on phonon parameters for infrared active modes in ferromagnetic spinel $CdCr_2S_4$, **Journal of Applied Physics**. 63 (**1988**) 5824–5829.

[158] J.A. Moreira, A. Almeida, W.S. Ferreira, J.E. Araújo, A.M. Pereira, M.R. Chaves, J. Kreisel, S.M.F. Vilela, P.B. Tavares, Coupling between phonons and magnetic excitations in orthorhombic $Eu_{1-x}Y_xMnO_3$, **Physical Review B**. 81 (**2010**) 054447.

[159] R.X. Silva, M.C. Castro Júnior, S. Yáñez-Vilar, M.S. Andújar, J. Mira, M.A. Señarís-Rodríguez, C.W.A. Paschoal, Spin-phonon coupling in multiferroic Y_2CoMnO_6, **Journal of Alloys and Compounds**. 690 (**2017**) 909–915.

[160] A.A. Belik, H. Yusa, N. Hirao, Y. Ohishi, E. Takayama-Muromachi, Peculiar High-Pressure Behavior of $BiMnO_3$, **Inorganic Chemistry**. 48 (**2009**) 1000–1004.

[161] J.J. Sakurai, J. Napolitano, Modern Quantum Mechanics, Second Edi, Cambridge University Press, Cambridge, **2017**.

[162] Y. Tokura, S. Seki, N. Nagaosa, Multiferroics of spin origin, **Reports on Progress in Physics**. 77 (**2014**) 076501.

9. APPENDIX

9.1 *Published works related to this thesis*

B. S. Araújo, A. M. Arévalo-López, J. P. Attfield, C. W. A. Paschoal, and A. P. Ayala, "Spin-phonon coupling in melanothallite Cu_2OCl_2," *Appl. Phys. Lett.*, vol. 113, no. 22, p. 222901, Nov. 2018.

9.2 *Works in submission state*

The Spin-phonon Coupling Effect on $BiCrO_3$, B. S. Araújo, A. M. Arévalo-López, C. C. Santos, J. P. Attfield, C. W. A. Paschoal, and A. P. Ayala. Submitted to Physical Review Materials

9.3 *Works in preparation state*

The Spin-phonon Coupling Effect on orthorhombic $TmMnO_3$, B. S. Araújo, A. M. Arévalo-López, C. C. Santos, J. P. Attfield, C. W. A. Paschoal, and A. P. Ayala.

The pressure dependent behavior of $BiCrO_3$ investigated through Synchrotron Radiation and Raman spectroscopy, B. S. Araújo, A. M. Arévalo-López, J. P. Attfield, C. W. A. Paschoal, and A. P. Ayala.

The pressure dependent behavior of $PbMn_7O_{12}$ through Synchrotron Radiation, B. S. Araújo, A. M. Arévalo-López, J. P. Attfield, C. W. A. Paschoal, and A. P. Ayala.

9.4 *Other published works during the Ph.D. period*

F. E. O. Medeiros, B. S. Araújo, and A. P. Ayala, "Raman spectroscopy investigation of the thermal stability of the multiferroic CuCl2 and its hydrated form," *Vib. Spectrosc.*, vol. 99, no. July, pp. 1–6, 2018.

A. Bongioanni, B. S. Araújo, Y. S. de Oliveira, M. R. Longhi, A. Ayala, and C. Garnero, "Improving Properties of Albendazole Desmotropes by Supramolecular Systems with Maltodextrin and Glutamic Acid," *AAPS PharmSciTech*, vol. 19, no. 3, pp. 1468–1476, 2018.

F. A. A. Aguiar *et al.*, “Effect of V_2O_5 Addition on the Phase Composition of $Bi_5FeTi_3O_{15}$ Ceramic and RF/Microwave Dielectric Properties,” *J. Electron. Mater.*, vol. 46, no. 4, pp. 2467–2475, 2017.

B. P. Bezerra *et al.*, “Phase transitions in secnidazole: Thermal stability and polymorphism studied by X-ray powder diffraction, thermal analysis and vibrational spectroscopy,” *Vib. Spectrosc.*, vol. 86, pp. 90–96, 2016.